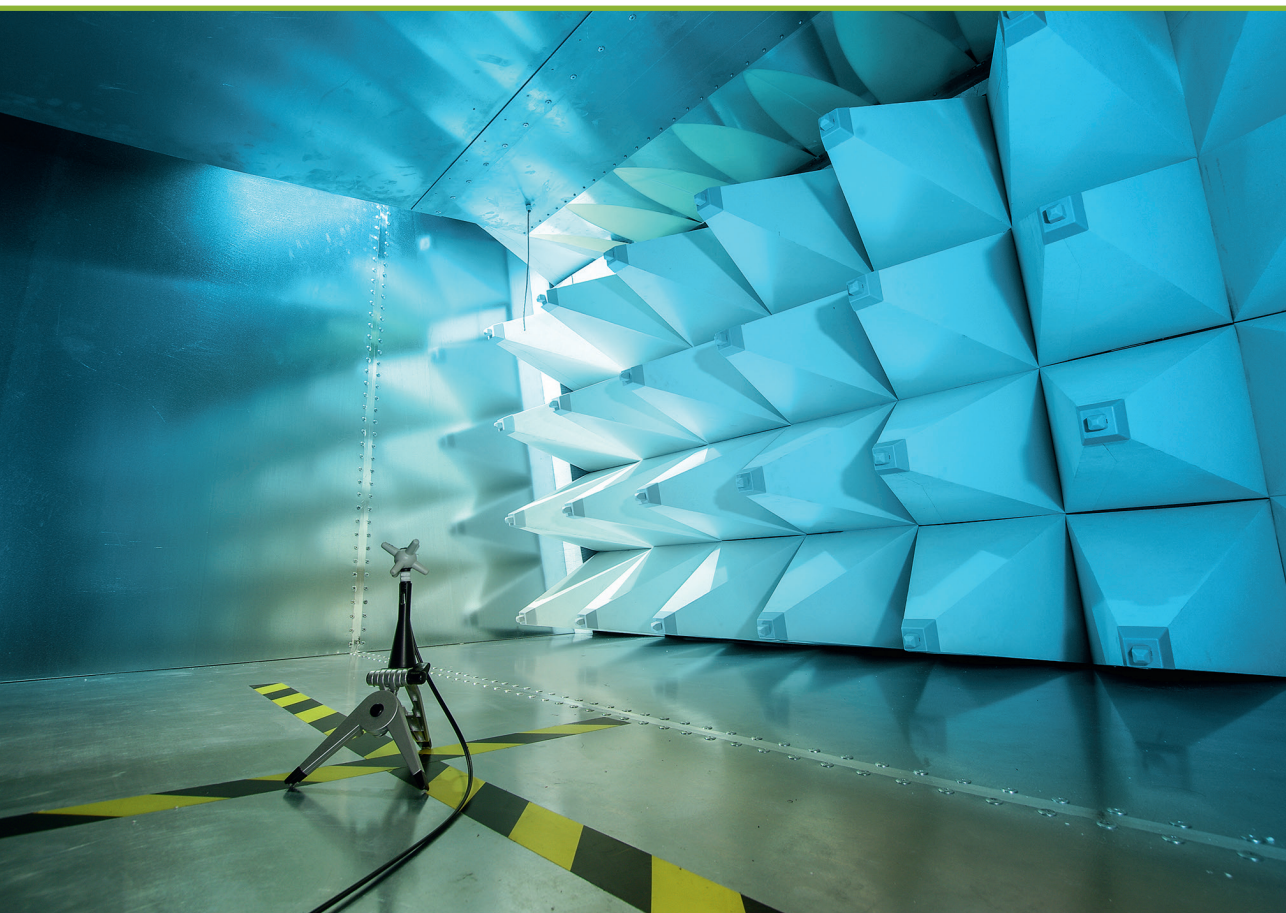


Romāns Kušņins

**MODEL SENSITIVITY EVALUATION AND
DIELECTRIC CONSTANT MEASUREMENT
UNCERTAINTY REDUCTION**

Doctoral Thesis



RIGA TECHNICAL UNIVERSITY

Faculty of Electronics and Telecommunications

Institute of Radioelectronics

Romāns Kušņins

Student of the doctoral study program "Electronics"

**MODEL SENSITIVITY EVALUATION AND
DIELECTRIC CONSTANT
MEASUREMENT UNCERTAINTY
REDUCTION**

Doctoral Thesis

Scientific supervisor:
Assistant Professor *Dr. sc. ing.*
JĀNIS SEMEŅAKO

RTU Press
Riga 2023

Kušņins, R. Model sensitivity evaluation and dielectric constant measurement uncertainty reduction. Summary of the Doctoral Thesis. Riga: RTU Press, 2023. 128 p.

Published in accordance with the decision of the Promotion Council “RTU P-08” of 26 January 2023, Minutes No. 18.



This work has been supported by the European Social Fund within the Project No 8.2.2.0/20/I/008 «Strengthening of PhD students and academic personnel of Riga Technical University and BA School of Business and Finance in the strategic fields of specialization» of the Specific Objective 8.2.2 «To Strengthen Academic Staff of Higher Education Institutions in Strategic Specialization Areas» of the Operational Programme «Growth and Employment»

**DOCTORAL THESIS PROPOSED TO RIGA TECHNICAL
UNIVERSITY FOR THE PROMOTION TO THE SCIENTIFIC
DEGREE OF DOCTOR OF SCIENCE**

To be granted the scientific degree of Doctor of Science (Ph. D.), the present Doctoral Thesis has been submitted for the defence at the open meeting of RTU Promotion Council on 31 March 2023 11.00 at the Faculty of Electronics and Telecommunications of Riga Technical University, Azenes 12, Room 201.

OFFICIAL REVIEWERS

Professor Dr. sc. ing. Dmitrijs Pikuļins
Riga Technical University

Professor Dr.-Ing. Ingo Gaspard
Hochschule Darmstadt, University of Applied Sciences, Germany

Associate professor Dr. Darius Plonis
Vilnius Gediminas Technical University, Lithuania

DECLARATION OF ACADEMIC INTEGRITY

I hereby declare that the Doctoral Thesis submitted for the review to Riga Technical University for the promotion to the scientific degree of Doctor of Science (Ph. D.) is my own. I confirm that this Doctoral Thesis had not been submitted to any other university for the promotion to a scientific degree.

Romāns Kušņins

Date:

The Doctoral Thesis has been written in English. It consists of an Introduction; 6 Chapters; Conclusion; 54 figures; 13 tables; the total number of pages is 128. The Bibliography contains 138 titles.

ANOTĀCIJA

Darbs ir veltīts augstfrekvences dielektriķu ar maziem zudumiem dielektriskās caurlaidības mērījumu modeļu izvērtēšanai un tādu mērījumu modeļu izveidošanai, kuru pielietošana samazina mērījumu nenoteiktību, ja tradicionālās metodes to nenodrošina.

Augstfrekvences dielektriķu pielietošana mūsdienu mikroviļņu iekārtās ir tik plaša, ka šajā jomā ilgus gadus veic pētījumus ne tikai universitātes un pētījumu centri, bet arī firmas, kuras ražo mēraparāturu un sertificētas testa laboratorijas. Lai gan ir sen nosecināts, ka universālu metožu un modeļu nav, tomēr bieži vien netiek piegriezta pietiekama vērība mērījumu modeļa piemērotības izvērtēšanai, it sevišķi gadījumos, kad ir jālieto nesagraujoša metode pie fiksēta parametru (parauga sagaidāmā dielektriskā caurlaidība, izmēri un ģeometriskā forma, frekvence, izvēlēta mērījumu metode u.c.) kopuma. Nepareiza modeļa izvēle un tā neizvērtēšana ne reti var dot tik lielu dielektriskās caurlaidības mērījumu nenoteiktību, ka mērījumu rezultāti nav praksē lietojami. Arī citi modeļi var nedot rezultātus, ja paraugu nesagrauj.

Šajā darbā tiek parādīta nepieciešamība vispirms analizēt vai izvēlētais mērījumu modelis dod iespējas pietiekami precīzi noteikt dielektrisko caurlaidību pie noteiktā parametru kopuma un šim mērķim tiek piedāvāta vienkārša un efektīva izvērtēšanas metode – modeļa jutības analīzes metode.

Darbā tiek parādīts un ar aprēķiniem pamatots, ka gadījumos, kad tiek noteikts, ka mērījumi ir jāveic pie nemainīga uzdotā parametru kopuma, bet tiek izsecināts, ka modelis nav piemērots, jo mērījumu nenoteiktība iznāk nepieņemami liela, ir iespējams veidot citu nesagraujošu mērījumu modeli, kura lietošana būtiski samazina mērījumu nenoteiktību un ka šādu modeli var izveidot, ja parauga tuvumā (vai tieši tam blakus) izvieto vienu vai divus modeļa papildus elementus. Var lietot arī citu pieeju, kad tiek mainīti parauga ģeometriskie izmēri, bet tas nozīmē, ka jāsagrauj paraugs, kas ne vienmēr ir pieļaujams un iespējams. Tā arī parasti dara, ja lieto rezonanses metodes.

Darbā konkrēti tiek pētīti modeļi, kuri lieto atstarošanās metodi, ja ar to mēra dielektrisko caurlaidību un lieto modeļus, kuros tiek mērīti plakani dielektriski paraugi taisnstūra viļņvadā un brīvā telpā un cilindriski dielektriski paraugi taisnstūra viļņvadā.

Mērījumu nenoteiktības izvērtēšanai tiek lietotas starptautiskajos standartos noteiktās metodes - Kļūdu izplatīšanās metode un Montekarlo metode, kas dod ticamu izvērtējamu arī nelineāriem modeļiem, bet šī metode prasa ļoti apjomīgu skaitļošanu. Šajā darbā tiek lietota autora izstrādāta efektīva skaitļošanas metode, kura modeļiem ar dielektriskiem cilindriem viļņvadā dod augstas precizitātes skaitlisku risinājumu daudzātrāk, kā līdz šim lietotās pieejas, kas deva iespēju pielietot Montekarlo metodi mērījumu modeļiem ar cilindru (un ar cilindriem) viļņvadā, kas bija praktiski neiespējams ar iepriekš lietotajām pieejām.

Darbā ir 128 lappuses, 54 attēli, 13 tabulas, 138 izmantotie literatūras avoti.

ANNOTATION

The thesis is devoted to evaluating dielectric constant measurement models for high-frequency low-loss dielectric materials and to constructing measurement models whose application reduces measurement uncertainty when conventional measurement methods cannot accomplish it.

The application of high-frequency dielectrics in modern microwave equipment is so extensive that not only universities and research centers but also companies that manufacture measuring equipment and certified test laboratories have been conducting research in this field for many years. Although universal methods and models are available, little attention has been paid to the evaluation of the suitability of the measurement model, particularly in cases where a non-destructive method is used and the model parameters must be fixed (expected value of sample dielectric constant, dimensions, shape, frequency, etc.). The use of an inappropriate model without an a priori evaluation of its suitability may lead to such a high uncertainty that the measurement results would not be usable in practice. Some models may also fail to give meaningful results for samples that, for various reasons, may not be altered.

In the thesis, it is demonstrated and justified through calculations that in the case when the measurements are performed using a model with a fixed set of parameters, and the model evaluation shows that it is not suitable, it is possible to reduce the measurement uncertainty via extending this model by adding to it one or more additional dielectric objects. Another approach is based on altering the dimensions of the sample, leading to its destruction, which is not always acceptable and possible. The thesis shows the importance of ascertaining if a selected measurement model is capable of providing sufficiently high dielectric constant accuracy for a given set of model parameters. To that end, a simple and effective measurement model evaluation method is proposed - the model sensitivity analysis method.

The measurement models investigated in the present thesis employ the reflection method to retrieve the dielectric constant and involve flat dielectric samples fitting tightly in the cross-section of a rectangular waveguide, flat dielectric samples located in free-space, and cylindrical dielectric full-height H-plane samples in a rectangular waveguide.

The measurement uncertainty is estimated using two international standard recommended methods, namely, the Error Propagation Method and Monte Carlo Method. The latter is highly computationally demanding while providing reliable uncertainty estimation of nonlinear models. In the thesis, an efficient computational method developed by the author is used, which for models involving dielectric cylindrical rods in a waveguide, ensures highly accurate results while being considerably faster than the existing general-purpose methods, thereby allowing one to perform the Monte Carlo-based measurement uncertainty estimation for the rod-based measurement models in a reasonable time-frame, which would be impossible if general-purpose methods were employed due to prohibitively large computational burden.

The thesis contains 128 pages, 54 figures, 13 tables, and 138 citations.

CONTENTS

LIST OF FIGURES	8
LIST OF TABLES AND ABBREVIATIONS.....	10
NOMENCLATURE.....	11
INTRODUCTION	13
Aim of the Thesis and Defended Theses.....	14
Main Tasks	15
Research Methods	16
Scientific Novelty.....	16
Main Results of the Thesis.....	17
Structure of the Thesis.....	17
Publications and Approbation of the Thesis	18
1 MODEL EVALUATION AND UNCERTAINTY ESTIMATION.....	21
1.1 Model Evaluation and Uncertainty Estimation.....	21
1.2 EMCP Extraction Methods	26
2 CONVENTIONAL MEASUREMENT MODELS	29
2.1 Single Slab Models	29
2.1.1 Single Slab Waveguide Measurement Model.....	29
2.1.2 Single Slab Free Space Measurement Model.....	36
2.2 Single Rod Waveguide Measurement Model.....	39
2.2.1 Overview of Single Rod Models.....	39
2.2.2 Uncertainty Analysis of Single Rod Model.....	41
2.3 Summary	44
3 MULTI-SLAB WAVEGUIDE MEASUREMENT MODEL.....	45
3.1 Overview of Extended and Optimized Measurement Models	45
3.2 Two-Slab Waveguide Measurement Model	45
3.2.1 Extended Model.....	45
3.2.2 Uncertainty Reduction.....	46
3.2.3 Extended Model Analysis.....	48
3.2.4 Solution of the Forward Problem	49
3.2.5 Numerical Study of The Two-Slab Waveguide Model.....	51
3.3 Three-Slab Waveguide Measurement Model.....	54
3.3.1 Shortcomings of Two-slab Measurement Model.....	54
3.3.2 Uncertainty Analysis of the Three Slab Model	55
3.4 Sensitivity Analysis for Two-Slab Waveguide Model	57
3.5 Summary	61
4 MULTI-SLAB FREE-SPACE MEASUREMENT MODEL.....	62
4.1 Two-slab Free Space Measurement Model.....	62
4.1.1 Overview of Free Space Measurement Model	62

4.1.2	Solution of the Forward Problem	62
4.1.3	Uncertainty Analysis of Free Space Models	67
4.2	Three Slab Free Space Measurement Model.....	69
4.3	Sensitivity Analysis of Two-Slab Free Space Model.....	72
4.4	Summary	75
5	TWO-ROD MEASUREMENT MODEL.....	77
5.1	Two-Rod Model	77
5.1.1	Overview of Two-Rod model.....	77
5.1.2	Uncertainty Analysis for Two-rod model.....	77
5.2	Summary	80
6	FAST INTEGRAL EQUATION METHOD.....	81
6.1	Multiple Dielectric Rod Structures	81
6.1.1	Overview of General Purpose Numerical Methods.....	81
6.1.2	Semi-Analytic Methods for Handling Cylindrical Obstacles.....	82
6.1.3	Discretization of Boundary Integral Equation.....	86
6.1.4	Evaluation of the Spectral Series Terms.....	92
6.1.5	Evaluation of the Spatial Series Terms.....	95
6.1.6	Evaluation of Excitation Vector Entries	99
6.1.7	Numerical Validation.....	100
6.1.8	Extended Boundary Integral Equation Method.....	103
6.1.9	Formulation	104
6.1.10	Numerical Verification	110
6.2	Summary	113
	CONCLUSIONS	114
	BIBLIOGRAPHY	116

LIST OF FIGURES

- 2.1 The conventional single slab waveguide measurement model.
- 2.2 $|S_{11}|$ as a function of $\varepsilon'_{r,\text{mut}}$ for the single slab waveguide model and the confidence intervals for $\varepsilon'_{r,\text{mut}} = 10.2$ and $\varepsilon'_{r,\text{mut}} = 4.3$.
- 2.3 $|S_{11}|$ as a function of $\varepsilon'_{r,\text{mut}}$ for two different values of $d_{r,\text{mut}}$ and the corresponding confidence intervals.
- 2.4 The conventional free space technique measurement model.
- 2.5 $|S_{11}|$ as a function of $\varepsilon'_{r,\text{mut}}$ and the confidence intervals for samples with two different $\varepsilon'_{r,\text{mut}}$.
- 2.6 $|S_{11}|$ as a function of $\varepsilon'_{r,\text{mut}}$ and the confidence intervals for two different $d_{r,\text{mut}}$.
- 2.7 The geometry of the conventional single rod measurement model.
- 2.8 $|S_{11}|$ as a function of $\varepsilon'_{r,\text{mut}}$, and confidence intervals for a model with a cylindrical sample in a waveguide calculated at two different values of $\varepsilon'_{r,\text{mut}}$.
- 2.9 $|S_{11}|$ as a function of $\varepsilon'_{r,\text{mut}}$ for different values of $r_{r,\text{mut}}$.
- 3.1 Geometry of the two-slab waveguide measurement model.
- 3.2 $u_{|S_{11}|}$ as a function of $|S_{11}|$ for vector network analyzer Keysight P5024B.
- 3.3 $|S_{11}|$ as a function of $\varepsilon'_{r,\text{mut}}$, and widths of confidence intervals for the conventional (CSWM) and the extended (ETSWM) models.
- 3.4 The standard uncertainty as a function of $\varepsilon'_{r,\text{mut}}$ for the conventional (CSWM) and the extended (ETSWM) models.
- 3.5 Three-slab waveguide measurement model geometry.
- 3.6 $|S_{11}|$ as a function of $\varepsilon'_{r,\text{mut}}$, and widths of the confidence intervals for the conventional (CSWM) and the extended (CTrSWM) models.
- 3.7 The standard uncertainty as a function of $\varepsilon'_{r,\text{mut}}$ for the conventional (CSWM) and the extended (CTrSWM) models.
- 3.8 The best estimate (mean value) of $\varepsilon'_{r,\text{mut}}$ as a function of d_{int} .
- 3.9 $u(\varepsilon'_{r,\text{mut}})$ as a function of d_{int} .
- 3.10 $u_{|S_{11}|}(\varepsilon'_{r,\text{mut}})$ as a function of d_{int} .
- 3.11 $u_{d_{\text{aux}}}(\varepsilon'_{r,\text{mut}})$ as a function of d_{int} .
- 3.12 $u_{d_{\text{mut}}}(\varepsilon'_{r,\text{mut}})$ as a function of d_{int} .
- 3.13 $u_{\varepsilon'_{\text{aux}}}(\varepsilon'_{r,\text{mut}})$ as a function of d_{int} .
- 3.14 $u_{\tan \delta_{\text{aux}}}(\varepsilon'_{r,\text{mut}})$ as a function of d_{int} .
- 4.1 Two-slab free space measurement model geometry.
- 4.2 $|S_{11}|$ as a function of $\varepsilon'_{r,\text{mut}}$, and confidence interval widths for the conventional (CSFSM) and the extended (ETSFSM) models.

- 4.3 The standard uncertainty as a function of the interslab distance for the conventional (CSFSM) and the extended (ETSFMS) models.
- 4.4 Three-slab free space measurement model geometry.
- 4.5 $|S_{11}|$ as a function of $\varepsilon'_{r,\text{mut}}$, and the confidence interval widths for the conventional (CSFSM) and the extended (ETrSFSM) models.
- 4.6 The standard uncertainty as a function of the interslab distance for the conventional (CSFSM) and the extended (ETrSFSM) models.
- 4.7 The best estimate of $\varepsilon'_{r,\text{mut}}$ as a function of d_{int} .
- 4.8 $u(\varepsilon'_{r,\text{mut}})$ as a function of d_{int} .
- 4.9 $u_{|S_{11}|}(\varepsilon'_{r,\text{mut}})$ as a function of d_{int} .
- 4.10 $u_{d_{\text{mut}}}(\varepsilon'_{r,\text{mut}})$ as a function of d_{int} .
- 4.11 $u_{d_{\text{aux}}}(\varepsilon'_{r,\text{mut}})$ as a function of d_{int} .
- 4.12 $u_{\varepsilon'_{\text{aux}}}(\varepsilon'_{r,\text{mut}})$ as a function of d_{int} .
- 4.13 $u_{\tan \delta_{\text{aux}}}(\varepsilon'_{r,\text{mut}})$ as a function of d_{int} .
- 5.1 Extended two-rod measurement model geometry.
- 5.2 $|S_{11}|$ as a function of $\varepsilon'_{r,\text{mut}}$ and confidence interval widths for the conventional (CSRWM) and the extended (ETRWM) models.
- 5.3 The standard uncertainty as a function of $\varepsilon'_{r,\text{mut}}$ for the conventional (CSRWM) and the extended (ETRWM) models.
- 6.1 The geometry of a multi-rod structure.
- 6.2 $|S_{11}|$ and $|S_{21}|$ as a function of ε_{r11} . Two solid dielectric rods.
- 6.3 $|S_{11}|$ and $|S_{21}|$ against ε_{r12} . Two two-layered dielectric rods.
- 6.4 $|S_{11}|$ and $|S_{21}|$ as a function of a/λ . Two solid dielectric rods.
- 6.5 $|S_{11}|$ and $|S_{21}|$ as a function of a/λ . Two two-layered dielectric rods.
- 6.6 Two dielectric rods in a rectangular waveguide.
- 6.7 $|S_{11}|$ as a function of $\varepsilon'_{r,\text{mut}}$, calculated using the IBIM and the HFSS.
- 6.8 The geometry of the problem.
- 6.9 Local coordinate systems of rods and their inclusions.
- 6.10 Single dielectric rod with two identical holes (HFSS model).
- 6.11 Two dielectric rods with two identical holes (HFSS model).
- 6.12 $|S_{11}|$ calculated for the single rod model as a function of a/λ_0 .
- 6.13 $|S_{11}|$ calculated for the double rod model as a function of a/λ_0 .
- 6.14 $|S_{21}|$ calculated for the double rod model as a function of a/λ_0 .
- 6.15 The phase of S_{21} calculated for the double rod model as a function of a/λ_0 .

LIST OF TABLES

Table 2.1	Single slab waveguide model parameters
Table 2.2	Model parameters for two single slab models
Table 2.3	Two single rod waveguide model parameters
Table 2.4	Single slab free-space model parameters
Table 2.5	Two single rod waveguide model parameters
Table 2.6	Single rod waveguide model parameters
Table 3.1	Two-slab waveguide model parameters
Table 3.2	Three-slab waveguide model parameters
Table 4.1	Two-slab free-space model parameters
Table 4.2	Three-slab free-space model parameters
Table 5.1	Two-rod waveguide model parameters
Table 6.1	Two-rod waveguide model parameters
Table 6.2	Comparison of calculation times

ABBREVIATIONS

EPM	Error Propagation Method
GUM	Guide to the Expression of Uncertainty in Measurement
EMCP	Electromagnetic Constitutive Parameters
ANN	Artificial Neural Networks
NRW	Nicolson-Ross-Weir Method
FEM	Finite Element Method
MCM	Monte Carlo Method
MoM	Method of Moments
MUT	Material Under Test (in text)
mut	Material Under Test (in formulas)
NRM	Newton-Raphson Root-finding Method
VNA	Vector Network Analyzer
T/R	Transmission/Reflection Method

NOMENCLATURE

γ_m	transverse wavenumber for the TE_{m0} mode
ε_0	permittivity of vacuum
$\varepsilon'_{r,\text{aux}}$	dielectric constant of the auxiliary slab (rod) material
$\varepsilon'_{r,\text{int}}$	dielectric constant of the middle slab material
$\varepsilon'_{r,\text{mut}}$	MUT dielectric constant
$\varepsilon_{r,\text{aux}}$	complex dielectric constant of the auxiliary slab (rod) material
$\varepsilon_{r,\text{int}}$	complex dielectric constant of the middle slab material
$\varepsilon_{r,\text{mut}}$	MUT complex dielectric constant
λ_0	free space wavelength
μ_0	permeability of vacuum
ω	angular frequency
a	width of the broader wall of a rectangular waveguide
$A_{n,\{j,i\}}$	n -th unknown electric field expansion coefficient for i -th layer of j -th rod
$B_{n,\{j,i\}}$	n -th unknown magnetic field expansion coefficient for i -th layer of j -th rod
c	speed of light
C_n^m	binomial coefficient
c_{cl}	conventional model sensitivity coefficient
c_{ex}	extended model sensitivity coefficient
d_{mut}	MUT slab thickness
d_{aux}	auxiliary slab thickness
d_{int}	interslab (interrod) distance or middle slab thickness
$\text{erf}(x)$	error function
$\text{Ei}(x)$	exponential integral
$E_y(\mathbf{r})$	tangential components of the total electric fields
$E_y^i(\mathbf{r})$	y component of the incident electric field
f	frequency
$G(\mathbf{r}_o, \mathbf{r}_s)$	waveguide Green's function
$H_\varphi(\mathbf{r})$	tangential components of the total magnetic field
$H_n^{(1)}(z)$	n -th order Hankel function of the first kind
$H_n^{(2)}(z)$	n -th order Hankel function of the second kind
\mathbf{I}	identity matrix
$J_n(z)$	n -th order Bessel function
k_o	free space wavenumber
\tilde{k}_o	TE_{10} mode waveguide wavenumber in the air-filled region
\tilde{k}	TE_{10} mode waveguide wavenumber in the dielectric-filled region
$\tilde{k}_{\{j,l\}}$	normalized wavenumber
\tilde{k}_{aux}	waveguide wavenumber in the auxiliary slab
$k_{\{j,o\}}$	wavenumber of the 0-th layer of the j -th rod

L_1	distance between the front reference plane and the front face of sample
L_2	distance between the rear reference plane and the rear face of sample
P	phase factor
\mathbf{S}	scattering matrix of measurement model
$ S_{11} $	magnitude of scattering matrix element S_{11}
r_{mut}	MUT rod radius
r_{aux}	auxiliary rod radius
\mathbf{r}_o	position vector of the observation point
\mathbf{r}_s	position vector of the source point
$\mathbf{r}_{\{i\}}$	position vector of point with polar coordinates $r_{\{i\}}$ and $\varphi_{\{i\}}$
r_m^\pm	distance between the m -th image of the source point and the observation point
R_{aux}	interfacial reflection coefficient for the auxiliary slab face
R_{mut}	interfacial reflection coefficient for the MUT slab face
S_l^\pm	l -th order Schlömilch series
S^{spac}	spacial part of the Schlömilch series
S^{spec}	spectral part of the Schlömilch series
T_{aux}	transmission coefficient for the auxiliary slab
T_{mut}	transmission coefficient for the MUT slab
$\tan \delta_{\text{mut}}$	dielectric loss tangent of MUT
$\tan \delta_{\text{aux}}$	dielectric loss tangent of the auxiliary slab (rod) material
$\tan \delta_{\text{int}}$	dielectric loss tangent of the middle slab material
u_a	standard uncertainty of the waveguide width
$u_{d_{\text{mut}}}$	standard uncertainty of the MUT slab thickness
u_f	standard uncertainty of the frequency
$u_{ S_{11} }$	standard uncertainty of $ S_{11} $
$u_{\epsilon'_{\text{aux}}}$	standard uncertainty of the auxiliary slab material dielectric constant
$u_{\tan \delta_{\text{mut}}}$	standard uncertainty of the MUT loss tangent
$u_{\tan \delta_{\text{aux}}}$	standard uncertainty of the auxiliary slab material loss tangent
x_o	x coordinate of the observation point
x_s	x coordinate of the source point
\mathbf{x}_e	vector containing unknown electric field expansion coefficients
\mathbf{x}_h	vector containing unknown magnetic field expansion coefficients
$Y_n(z)$	n -th order Neumann function
z_o	z coordinate of the observation point
z_s	z coordinate of the source point
Z_0	free space intrinsic impedance
\mathbf{Z}^H	magnetic part of system matrix
\mathbf{Z}^E	electric part of system matrix
\mathbf{Z}^{DH}	diagonal magnetic part of system matrix
\mathbf{Z}^{DE}	diagonal electric part of system matrix

INTRODUCTION

Nowadays, there are countless applications where electromagnetic fields and waves play a central role - electronics, telecommunications and radars, computer technology, military technologies, industrial applications, medicine, biosciences and biotechnologies, geology, agriculture, etc. For most of these applications, it is critical to know how these fields and waves behave in different media and materials, interact with and propagate in and affect them. In electromagnetics, the way the electromagnetic fields interact with materials is described by a set of constitutive relations, which differ between materials and are characterized by a set of electromagnetic constitutive parameters (EMCP), such as dielectric constant, magnetic permeability, and electrical conductivity. The EMCP, in general, may vary with time, position, frequency, as well as pressure, and ambient temperature. Additionally, these parameters may exhibit either linear or non-linear dependence on the aforementioned quantities and even may be dependent on the direction of the fields they interact with - as it occurs in anisotropic media [1].

In some microwave applications, it is essential to know the EMCP of materials with sufficiently high accuracy. Thus, the measurement of the EMCP has been the subject of many studies for several decades. A number of attempts have been made to theoretically describe and predict the EMCP of materials; however, only values obtained through experimental measurements are valid for applications, and numerous different measurement methods for the measurement of material EMCP suitable for a wide range of frequencies have been proposed [2].

Although the range of dielectric (including magneto-dielectric) materials used in various microwave applications is wide [3], a special place in terms of application is occupied by components having a specific shape, e.g., slabs, laminated structures, cylindrical [4] rods, which are extensively employed in microwave devices, including, among others, various microstrip filters, dielectric and magnetic resonators, dielectric antennas substrates, dielectric waveguides, etc. [5]. Consequently, in recent years, great attention has been paid to the EMCP measurement of these materials.

Different methods for the EMCP measurements of materials, as well as their reliability evaluation, have been developed [6]. Companies manufacturing high-precision measurement instrumentation also investigate and describe measurement methods, their advantages, and disadvantages, and develop new measurement equipment and software for the EMCP measurement [7, 8]. However, most of the papers and guidelines concerning the EMCP measurements published to date do not properly reflect such an important aspect that the measurement model sensitivity depends on the shape and dimensions of the sample, as well as frequency and even the measurement method itself, even though there are internationally accepted standards defining how the sensitivity of the model should be evaluated, which shows how the output (measurable quantity) estimate varies with changes in the values of the input estimates, and there are methods for the measurement uncertainty estimation [9].

While there are a number of standard measurement methods developed for use in testing laboratories, most of them are destructive ones (typically resonant methods), especially when measuring MUT with small losses. In addition, these methods are very expensive, time-consuming,

require very careful sample preparation and well-equipped laboratories, and are not well suited for testing ready-to-use products [10]. These test methods are mandatory for manufacturers [11], but due to the rapidly growing number of new dielectric materials possessing properties that make them very attractive for the application in microwave technologies, researchers are forced to seek other measurement models, preferably non-destructive ones (or at least low-destructive) that would be well suited for measurement of these new materials [12]. The main reason the non-destructive methods are more attractive than their destructive counterparts is that they do not require a complex sample preparation procedure, especially in the case of fragile and difficult-to-handle materials, such as various ceramics extensively used at microwave frequencies [13]. Moreover, ceramic materials with low losses [14], and high dielectric constant [15] might be of particular interest in a variety of current applications, as well as some future applications, since their use results in more compact microwave components and devices.

Even in a seemingly simple case when the dielectric constant of non-magnetic solid material with very low losses and simple geometric shape, which are widely used in microwave technologies, needs to be determined, there is no simple, easy-to-use methodology for verification of the validity of the measurement models. Furthermore, in the vast majority of reported studies, only comparison of different measurement methods, as well as the results obtained with them, are presented, while little or no attention has been paid to the sensitivity of the models to the measured EMCP of MUT and the suitability of the models for the EMCP measurements with a specific set of model parameter values or value ranges [16]. Only in a few studies comparison and evaluation of the existing models are made, as well as new models are proposed, e.g., [17], [18] and [19], where more accurate dielectric constant measurement results for specific cases and some models are also evaluated from the point of view of uncertainty reduction.

In most papers, the problem of the suitability of a measurement model involving a specific MUT with a specific set of model parameter values is mentioned or superficially described but not thoroughly investigated, and no attempt has been made to resolve it so far. Often, methodologies for the reduction of the measurement uncertainty are developed without an a priori evaluation of the measurement model in terms of the suitability [20]; however, such a reduction may not be achievable when an unsuitable measurement model is selected.

Aim of the Thesis and Defended Theses

In order to address the problems mentioned above related to the effective evaluation of the suitability of dielectric constant measurement models, the selection of models, and the development of measurement models that ensure sufficiently small measurement uncertainty, the following main objectives of the thesis are put forward:

- Develop a methodology for simple evaluation of the measurement model sensitivity;
- Develop improved measurement models ensuring a sufficiently high model sensitivity in cases where conventional measurement models cannot accomplish it.

In order to achieve the main objectives of the thesis, the following defended theses were defined:

1. The sensitivity of the measurement model depends on the selected measurement method, and for a sample with a specific shape and dimensions at a specific measurement frequency, the sensitivity strongly depends on the expected value of the dielectric constant and takes values in the range from 0 to 20;
2. The sensitivity of the measurement model is related to the measurement uncertainty, and if the model sensitivity is less than 1, then the relative uncertainty of the dielectric constant measurement is greater than 1%;
3. To evaluate the suitability of the measurement model, it is not necessary to solve the time-consuming inverse problems for the measurement uncertainty estimation, as it suffices to evaluate the sensitivity of the model from a solution to the forward problem using the Error Propagation Method, which reduces the model evaluation time by at least an order of magnitude;
4. If the classical measurement model has a measurement sensitivity of less than 1, such a model is considered not suitable for the dielectric constant measurements, and an extended measurement model must be constructed by adding a dielectric slab or rod, the dimensions, position, and dielectric constant of which are calculated in such a way as to ensure the sensitivity of the measurement model greater than 1;
5. To be able to perform the dielectric constant measurement uncertainty estimation for models involving dielectric rods, it is necessary to develop a fast numerical method that is at least 50 times faster than currently existing methods.

Main Tasks

1. To show that one can quickly and easily estimate and evaluate the sensitivity of the measurement model for any specific set of model parameter values to determine whether the model is suitable for the measurement or whether the measurement uncertainty will be unacceptably high. Additionally, the evaluation procedure allows for determining whether the model can ensure a specific measurement uncertainty.
2. To prove that the dielectric constant measurement uncertainty is closely related to the measurement model sensitivity and, therefore, the uncertainty can be reduced by increasing the model sensitivity.
3. To show that it is possible to increase the sensitivity of the measurement model for a specific set of model parameters by extending a conventional measurement model, which is accomplished by placing an additional object (or objects) or by altering the dimensions of the MUT or the frequency, provided that such alterations are permitted.
4. Develop a methodology and computer programs for constructing optimal extended models for specific cases.

5. To develop a numerical method for the calculation of the scattering matrix elements for dielectric constant measurement models involving dielectric rods in a rectangular waveguide, which provides at least 50 times faster measurement uncertainty estimation than currently existing methods.

Research Methods

During the development of the thesis, analytical and numerical calculations, as well as computer modeling, are employed to achieve the objectives of the thesis and perform problem analysis.

For calculating the scattering parameters of the dielectric constant measurement model with dielectric rods in a rectangular waveguide, the fast calculation method developed by the author, namely, the method of surface integral equations, is used.

Commercially available software Ansys HFSS is also used to check the accuracy and efficiency of the Improved Boundary Integral Equation Method developed by the author. The inverse problems are solved by means of the Newton-Rafson method.

Computer programs implemented in Python and C++ programming languages were developed for the calculation of the scattering parameters of the measurement models studied in the thesis, as well as for the evaluation of the dielectric constant measurement uncertainty.

The programs intended for solving time-consuming tasks, for example, the calculation of Schlömilch series using the Ewald method, were implemented in C++ language, and the parallel data processing libraries OpenMP and OpenMPI are used to speed up the calculations.

The other programs were implemented in the Python programming language, including program packages for drawing graphs developed by the author.

Scientific Novelty

- A simple Error Propagation Method based methodology for evaluating the sensitivity of a measurement for quick evaluation of the suitability of a specific measurement model for achieving a certain measurement uncertainty in dielectric constant measurements without extensive computing under non-destructing fixed frequency measurement scenario when the MUT in the measurement model is a slab or a rod in a waveguide or a dielectric slab in free space.
- A new two-slab waveguide or free-space measurement model to reduce the uncertainty in the dielectric constant measurements via increasing the measurement model sensitivity.
- A new three-slab waveguide or free space measurement model to reduce the dielectric constant measurement uncertainty via increasing the measurement model sensitivity.
- A new measurement model, composed of two dielectric rods in a rectangular waveguide, reducing the dielectric constant measurement uncertainty by increasing the measurement model sensitivity.

- A new efficient numerical method for calculating the dominant waveguide mode scattering matrix elements for multi-layered full-height rods in a rectangular waveguide. The rods can have an arbitrary number of dielectric inclusions.

Main Results of the Thesis

1. The developed measurement model sensitivity evaluation methodology for determining whether the range of possible dielectric constant values is in a measurement model low-sensitivity range, giving measurement uncertainty too large to ensure acceptable measurement accuracy under a non-destructive fixed frequency waveguide or free space measurement scenario.
2. The use of the extended dielectric constant measurement models, in some instances, provides model sensitivity that is significantly higher than that of the conventional model, which contains only the object under test (rod or slab), resulting in smaller measurement uncertainty. The measurement models investigated in the thesis are:
 - a dielectric slab, the constant of which is determined from the measured value of the modulus of the scattering matrix element S_{11} measured for the dominant rectangular waveguide mode (in the case of waveguide measurements) or a plane wave (in the case of the free-space measurement model) and extended models with two or three dielectric slabs, one of which is a slab made of the material under test (MUT);
 - a dielectric rod in a rectangular waveguide with a dielectric constant to be determined from the measured absolute value of the scattering matrix element S_{11} for the dominant waveguide mode and extended models with an auxiliary dielectric rod of known constitutive properties and dimensions;
3. The developed numerical methods for solving integral equations, which use the Ewald method for the calculation of slowly converging Schlömilch series, allows for calculating scattering parameters for structures consisting of multiple full-height dielectric rods in a rectangular waveguide, up to 500 times faster than commercially available finite element method based software.

Structure of the Thesis

The thesis is composed of six chapters, conclusion and bibliography. Chapter 1 presents an introductory overview of the measurement uncertainty estimation methods used for the measurement model evaluation. Additionally, several terms for quantities and objects frequently referred to throughout the thesis are defined, and a brief overview of the state-of-the-art in the field of dielectric permittivity measurements is provided. Chapter 2 is devoted to a discussion of three conventional dielectric constant measurement models. Also, the role of the model sensitivity in the dielectric constant measurements is described, and viable approaches to improving the model sensitivity are outlined. In chapter 3 a methodology for improving the measurement

model sensitivity is described and applied to a conventional model involving a flat dielectric slab made of MUT in a rectangular waveguide. The resulting extended model is evaluated by means of the MCM with a view to finding an optimal set of model parameters to reduce the measurement uncertainty. Chapter 4 discusses the application of the proposed sensitivity improvement methodology to a conventional free space measurement model and presents the results of the uncertainty analysis of the resulting extended model. In chapter 5, the proposed sensitivity improvement methodology is applied to the waveguide-based rod measurement model, and the relevant model evaluation results are presented and discussed. Chapter 6 addresses the improved integral equation-based method proposed and developed by the author to considerably reduce the uncertainty estimation time for the models involving dielectric rods.

Publications and Approbation of the Thesis

The results of the Doctoral Thesis have been presented at 5 scientific conferences and workshops, whose full-length paper proceedings are indexed in SCOPUS, WoS, and IEEE databases.

1. Kushnin, R., Semenjako, J. and "Determination of the Optimal Value of the Radius of a Circular Cylindrical Post in a Rectangular Waveguide for Measurement of the Dielectric Permittivity," presented at Progress in Electromagnetic Research Symposium(PIERS 2013), Sweden, Stockholm, 12-15 August, 2013.
2. Kushnin, R., Semenjako, J., and Solovjova, T. "Determination of Optimal Pairs of Radii of Dielectric Samples for Complex Permittivity Measurement of Dispersive Materials," presented at Progress in Electromagnetics Research Symposium (PIERS2015), Czech Republic, Prague, 6-9 July, 2015.
3. Kushnin, R., Semenjako, J., and Shestopalov, Y. "Accelerated Boundary Integral Method for Solving the Problem of Scattering by Multiple Multilayered CircularCylindrical Posts in a Rectangular Waveguide," presented at Progress in Electromagnetics Research Symposium - Spring (PIERS 2017), Russia, Saint Petersburg, 22-25 May, 2017.
4. Kimsis, K., Semenjako, J., Kushnin, and R., Viduzs, A. "Numerical Implementation of Efficient Cross-Section Method for the Analysis of Arbitrarily Shaped Dielectric Obstacles in Rectangular Waveguide," presented at Progress in Electromagnetics Research Symposium - Spring (PIERS 2017), Russia, Saint Petersburg, 22-25 May, 2017.
5. Kushnin, R., Semenjako, J., and Shestopalov Y. "Fast Method for Analysis of Multiple H-Plane Cylindrical Posts with Multiple Cylindrical Inclusions in a Rectangular Waveguide," presented at the 2020 IEEE Microwave Theory and Techniques in Wireless Communications (MTTW), Oct. 2020.

The results of the Doctoral Thesis are presented in 9 out of 14 author's scientific articles and in publications in conference proceeding indexed in SCOPUS, WoS, and IEEE databases.

1. Kushnin, R., Semenjako, J. "Scattering by a Layered Circular Cylindrical Post in a Rectangular Waveguide." *Telecommunications and Electronics*. Vol.11, 2011, pp.41-48. ISSN 1407-8880.
2. Kushnin, R., Semenjako, J. "Determination of the Optimal Value of the Radius of a Circular Cylindrical Post in a Rectangular Waveguide for Measurement of the Dielectric Permittivity," In: *Progress in Electromagnetic Research Symposium(PIERS 2013): Proceedings*, Sweden, Stockholm, 12-15 August, 2013. Stockholm: The Electromagnetics Academy, 2013, pp.52-57.
3. Kushnin, R., Semenjako, J., Solovjova, T. "Determination of Optimal Pairs of Radii of Dielectric Samples for Complex Permittivity Measurement of Dispersive Materials," In: *Progress in Electromagnetics Research Symposium (PIERS2015): Proceedings*, Czech Republic, Prague, 6-9 July, 2015. Prague: The Electromagnetics Academy, 2015, pp.2320-2325.
4. Kushnin, R., Semenjako, J., Shestopalov, Y. "Accelerated Boundary Integral Method for Solving the Problem of Scattering by Multiple Multilayered Circular Cylindrical Posts in a Rectangular Waveguide," In: *2017 Progress in Electromagnetics Research Symposium - Spring (PIERS)*, Russia, St.Petersburg, 22-25 May, 2017. Piscataway: IEEE, 2017, pp.3263-3271.
5. Kimsis, K., Semenjako, J., Kushin, R., Vidužs, A. "Numerical Implementation of Efficient Cross-section Method for the Analysis of Arbitrarily Shaped Dielectric Obstacles in Rectangular Waveguide." In: *2017 Progress in Electromagnetics Research Symposium - Spring (PIERS 2017): Proceedings*, Russia, Saint Petersburg, 22-25 May, 2017. Piscataway: IEEE, 2018, pp.3937-3943.
6. Kushnin, R., Semenjako, J., Shestopalov, Y. "Maximum-Sensitivity Method for Minimizing Uncertainty in the Measurements of Permittivity of a Cylindrical Dielectric Sample in a Rectangular Waveguide." In: *2017 Progress in Electromagnetics Research Symposium - Fall (PIERS - FALL): Proceedings*, Singapore, Singapore, 19-22 November, 2017. Piscataway: IEEE, 2018, pp.570-578. ISBN 978-1-5386-1212-5. e-ISBN 978-1-5386-1211-8.
7. Kushins, R., Semenjako, J., Shestopalov, Y., Vidužs, "A. Two-slab High Sensitivity Technique for Measurement of Permittivity of a Dielectric Slab in a Rectangular Waveguide." In: *Progress in Electromagnetics Research Symposium 2018: Proceedings*, Japan, Toyama, 1-4 August, 2018. Piscataway: IEEE, 2018, pp.176-183.
8. R. Kushin, G. Kuzminovs, J. Semenjako and Y. V. Shestopalov, "Novel High-sensitivity Non-destructive Technique for the Measurement of Permittivity of a Low-loss Dielectric Slab in Free Space," *2019 Photonics & Electromagnetics Research Symposium - Spring (PIERS-Spring)*, 2019, pp. 1723-1731, doi: 10.1109/PIERS-Spring46901.2019.9017638.

9. R. Kushnin, J. Semenjako and Y. Shestopalov, "Fast Method for Analysis of Multiple H-Plane Cylindrical Posts with Multiple Cylindrical Inclusions in a Rectangular Waveguide," 2020 IEEE Microwave Theory and Techniques in Wireless Communications (MTTW), 2020, pp. 190-194, doi: 10.1109/MTTW51045.2020.9244922.

1. MODEL EVALUATION AND UNCERTAINTY ESTIMATION

1.1 Model Evaluation and Uncertainty Estimation

In this thesis, the measurements of the dielectric constant of low-loss cylindrical samples (rods) and dielectric slabs are investigated. The dielectric constant is determined with the aid of a reflection-only method (only the magnitude of scattering matrix element $|S_{11}|$ is measured). The measurement models examined in the present study account for the MUT losses, which are assumed to be known a priori.

For the sake of convenience, several terms used throughout the thesis are introduced. The term **measurement model** throughout this thesis applies to a measurement procedure together with the mathematical relations relating the quantity of the interest (measurable quantity) that in the present case is dielectric constant, and other quantities whose values are required to determine the value of the measurable quantity.

For a specific shape and dimensions of the MUT sample (including the dimensions and the position of the auxiliary model elements, if any), the measurement frequency, and the MUT dielectric constant, the measurement uncertainty may be acceptable but may also be so large that the results of such measurements would be absolutely useless from the practical point of view. It is shown that a considerable measurement uncertainty results from a low sensitivity of the measurement model, which shows how sensitive the magnitude of S_{11} , hereinafter denoted by $|S_{11}|$, to small variations in the dielectric constant. Not only $|S_{11}|$, which is the quantity that is being measured directly, but also the aforementioned parameters are subject to uncertainties and therefore contribute to the total measurement uncertainty. There are myriad random factors affecting measurement accuracy, but in practice, it suffices to take into consideration only those that make the most significant contribution to the overall accuracy [21]. These factors include, among others, limited resolution, residual systematic error, connection mismatch, and geometrical imperfections of the sample, such as a slight shift in the position of the sample and the accuracy of the measurement of the sample dimensions.

Measurement uncertainty estimation methods are employed to determine the total measurement uncertainty for a given model. The most extensively used are the EPM and MCM [9, 22]. The simpler one is the EPM, which, however, is applicable only to models amenable to an adequate linear approximation, which is a severe limitation of the method. Alternatively, to estimate the measurement uncertainty for the range of the measurement model parameter values for which the dependence of the output quantity (measurable quantity) on the parameters is highly nonlinear, the application of the EPM method may result in a considerable over- or under-estimation of the uncertainty, that may lead to highly undesirable consequences if such inaccurate data is used. Another commonly used uncertainty estimation method is the MCM, which is more reliable as it accounts for the non-linearity of the measurement model. Additionally, the uncertainty estimation using the MCM was recently shown to be an effective means of finding optimal dimensions (radius) of a measurement model composed of a cylindrical dielec-

tric MUT in a cylindrical resonant cavity [23] that gives the lowest measurement uncertainty. However, due to its stochastic nature, the uncertainty estimation with the MCM, in many cases, is quite computationally demanding.

As far as sources of measurement uncertainty [24] are concerned, the measurement uncertainty associated with the measurable quantity $|S_{11}|$, as well as other quantities (measurement model parameters) that are not measured directly but affect the value of $|S_{11}|$ and therefore also contribute to the total uncertainty are considered in the present study. In general, however, it is highly desirable to account for the following uncertainties [22]:

- accuracy of the instruments used in the measurements
- effect of the measuring instrument resolution
- repeatability of the results
- reproducibility of the measurement setup

In the present study, all of these sources are considered except the last two (repeatability and reproducibility) are taken into account since it is very difficult to quantify them. There is another type of uncertainty that is also difficult to estimate - systematic uncertainty. Unfortunately, it cannot be removed entirely - even a complex calibration procedure cannot completely eliminate this type of uncertainty, only reduce it.

Systematic uncertainties encountered in microwave waveguide or free space measurements are related to signal leakage, signal reflections, and frequency response. There are six types of systematic errors associated with the measurement by means of VNA [25].

- directivity and cross-talk errors relating to signal leakage
- source and load impedance mismatches relating to reflections
- frequency response errors caused by reflection and transmission tracking within the test receivers

In the present study, the dielectric constant of the MUT is extracted from a measured $|S_{11}|$ by solving the inverse problem. It is assumed that the expected value of the dielectric constant is approximately known. Although the measured $|S_{11}|$ is the only source of information available to retrieve a dielectric constant, it is enough provided that the dielectric constant of the MUT is approximately known a priori; that is the case in most measurements.

In the EPM the total uncertainty in dielectric constant measurements is given by [26]:

$$u(\varepsilon'_{r,\text{mut}}) = \sqrt{u_{|S_{11}|}^2(\varepsilon'_{r,\text{mut}}) + u_{d_{\text{mut}}}^2(\varepsilon'_{r,\text{mut}}) + u_f^2(\varepsilon'_{r,\text{mut}}) + u_{\tan\delta_{\text{mut}}}^2(\varepsilon'_{r,\text{mut}})}. \quad (1.1)$$

Slightly rearranging (1.1), gives the following expression that is more illustrative from a point of view of the main objective of the thesis, namely, it shows how important is the role the factor

$\frac{\partial |S_{11}|}{\partial \varepsilon'_{r,\text{mut}}}$ plays in the model evaluation in terms of the measurement accuracy, as discussed below.

$$u(\varepsilon'_{r,\text{mut}}) = \frac{1}{\frac{\partial |S_{11}|}{\partial \varepsilon'_{r,\text{mut}}}} \cdot \sqrt{(u_{|S_{11}|})^2 + \left(\frac{\partial |S_{11}|}{\partial d_{\text{mut}}} u_{d_{\text{mut}}}\right)^2 + \left(\frac{\partial |S_{11}|}{\partial f} u_f\right)^2 + \left(\frac{\partial |S_{11}|}{\partial \tan \delta_{\text{mut}}} u_{\tan \delta_{\text{mut}}}\right)^2}. \quad (1.2)$$

The quantities appearing in the radicand are the contributions of individual parameters of the measurement model to the total uncertainty of dielectric constant measurements and are given by:

$$u_{|S_{11}|}(\varepsilon'_{r,\text{mut}}) = \frac{\partial \varepsilon'_{r,\text{mut}}}{\partial |S_{11}|} u_{|S_{11}|} - \text{the measurement uncertainty contribution of } |S_{11}|,$$

$$u_{d_{\text{mut}}}(\varepsilon'_{r,\text{mut}}) = \frac{\partial \varepsilon'_{r,\text{mut}}}{\partial d_{\text{mut}}} u_{d_{\text{mut}}} - \text{the MUT slab thickness measurement uncertainty contribution,}$$

$$u_f(\varepsilon'_{r,\text{mut}}) = \frac{\partial \varepsilon'_{r,\text{mut}}}{\partial f} u_f - \text{the frequency measurement uncertainty contribution,}$$

$$u_a(\varepsilon'_{r,\text{mut}}) = \frac{\partial \varepsilon'_{r,\text{mut}}}{\partial a} u_a - \text{the waveguide width measurement uncertainty contribution,}$$

$$u_{\tan \delta_{\text{mut}}}(\varepsilon'_{r,\text{mut}}) = \frac{\partial \varepsilon'_{r,\text{mut}}}{\partial \tan \delta_{\text{mut}}} u_{\tan \delta_{\text{mut}}} - \text{the contribution of the MUT loss tangent measurement uncertainty,}$$

where

$$u_{|S_{11}|} - \text{the standard uncertainty of } |S_{11}|;$$

$$u_{d_{\text{mut}}} - \text{the standard uncertainty of the MUT slab thickness, mm;}$$

$$u_f - \text{the standard uncertainty of the frequency, GHz;}$$

$$u_a - \text{the standard uncertainty of the waveguide width, mm;}$$

$$u_{\tan \delta_{\text{mut}}} - \text{the standard uncertainty of the MUT loss tangent.}$$

Since the value of the dielectric constant is retrieved from $|S_{11}|$, which is measured directly, and its value depends on the other parameters of the measurement model, their contributions can be expressed as follows:

$$u_{d_{\text{mut}}}(\varepsilon'_{r,\text{mut}}) = \frac{\partial \varepsilon'_{r,\text{mut}}}{\partial |S_{11}|} \frac{\partial |S_{11}|}{\partial d_{\text{mut}}} u_{d_{\text{mut}}},$$

$$u_f(\varepsilon'_{r,\text{mut}}) = \frac{\partial \varepsilon'_{r,\text{mut}}}{\partial |S_{11}|} \frac{\partial |S_{11}|}{\partial f} u_f,$$

$$u_a(\varepsilon'_{r,\text{mut}}) = \frac{\partial \varepsilon'_{r,\text{mut}}}{\partial |S_{11}|} \frac{\partial |S_{11}|}{\partial a} u_a,$$

$$u_{\tan \delta_{\text{mut}}}(\varepsilon'_{r,\text{mut}}) = \frac{\partial \varepsilon'_{r,\text{mut}}}{\partial |S_{11}|} \frac{\partial |S_{11}|}{\tan \delta_{\text{mut}}} u_{\tan \delta_{\text{mut}}}.$$

The numerical study carried out by the author, as well as the EPM formula (1.2) reveals that

the slope of the function graph $|S_{11}(\varepsilon'_{r,\text{mut}})|$ when the other model parameters are kept fixed is determined by the derivative $\frac{\partial |S_{11}|}{\partial \varepsilon'_{r,\text{mut}}} = \left(\frac{\partial \varepsilon'_{r,\text{mut}}}{\partial |S_{11}|} \right)^{-1}$.

Hereinafter the curve $|S_{11}(\varepsilon'_{r,\text{mut}})|$ for a given measurement model will be referred to as the **model measurement curve**. From (1.2) it follows that the steepness of $|S_{11}(\varepsilon'_{r,\text{mut}})|$, which in essence is the derivative $\frac{\partial |S_{11}|}{\partial \varepsilon'_{r,\text{mut}}} = \left(\frac{\partial \varepsilon'_{r,\text{mut}}}{\partial |S_{11}|} \right)^{-1}$, is a quantity, which ultimately determines how large the total measurement uncertainty will be, as the contribution of all model parameters is inversely proportional to its value. Hence, in this thesis, the derivative is termed the **model sensitivity coefficient** of the measurement model. The model sensitivity coefficient shows that in the value ranges where the measurement curve is almost parallel to the argument axis $\varepsilon'_{r,\text{mut}}$, it is impossible to measure the dielectric constant for this model as the uncertainty will be very large.

A measurement model containing only a sample made of the material under test (MUT) only, i.e., the material whose dielectric constant is to be determined, is referred to throughout the thesis as a **conventional measurement model**.

In order to find an optimal set of model parameter values giving the smallest uncertainty, the uncertainty estimation needs to be performed for different model parameter combinations. In the present thesis, the MCM is employed as the primary standard uncertainty estimation method due to higher uncertainty estimation accuracy for non-nonlinear measurement models, which is the case for the models examined in this thesis. However, since the model sensitivity concept playing a crucial role in this research is based on the EPM, which is approximate by its nature, it is of particular importance to compare the estimation results obtained using both methods. The comparative study was carried out for the extended models to be described in the following chapters.

The MCM estimation relies on interpreting all the model parameters contributing to the total measurement uncertainty as random quantities whose mean values are the corresponding best estimates. According to the Guide to the expression of uncertainty in measurement (GUM) [27], each input parameter, whether it is measured directly quantity or indirectly, is assigned a probability distribution on the basis of the maximum entropy principle [28], which states that the probability distribution for a model parameter must be chosen based on the available information about the value of the parameter. For example, if only the mean value (the best estimate) and the uncertainty (standard or expanded) are known for a model parameter, then it is assumed to follow a normal distribution [29].

Once the probability distributions are chosen, the MCM generates samples for all model parameters with the same number of elements, each of which is drawn from the corresponding probability distribution. Then, the sample of the model output quantity is obtained by evaluating the model at each set of the model input quantity sample elements until the size of the output sample becomes equal to that of the input ones. Finally, from the obtained model output value sample, the MCM extracts the necessary statistical data, namely, the sample mean and the standard deviation, as they are used as the best estimate of the value of the measurable quantity and the corresponding uncertainty, respectively [30].

In this thesis, the sample for each considered model parameter is produced utilizing a pseudo-random number generator [31–33] in conjunction with the Box-Muller transform [34] used to convert the sample of the standardized uniform distribution to the sample corresponding to the normal distribution. Then for each combination of the model parameter values taken from the respective samples, the corresponding value of the dielectric constant is calculated to obtain the output sample. The dielectric constant values are found via solving the inverse problem by means of the NRM root-finding method [35]. Once the sample of the dielectric constant values is generated, its mean value and standard uncertainty can be calculated in a straightforward manner. For the uncertainty estimation to be reliable, typically, a large number of sample elements (dielectric constant values) is necessary. While for measurement models that can be described by a set of simple closed-form expressions, generating large output data samples does not pose any problem as the relevant computations can be performed very quickly, for models which require solving a system of equations this may lead to a prohibitively large amount of CPU time that may exceed the capacity of modern off-the-shelf computing machines thereby requiring the use of high power computing systems that in most cases is not a cost-effective way of the uncertainty estimation.

Special treatment is necessary when the actual value of the dielectric constant is in the vicinity of a minimum or maximum of the model measurement curve, as in this case, the NRM root-finding algorithm may converge to an incorrect solution since the values of the dielectric constant resulting in the same value of $|S_{11}|$ are very close to each other. In this study, to overcome this issue, the derivative of the measurement curve is evaluated twice: first, at the actual values of the model parameters before the first iteration of the NRM method; the second time, the derivative is evaluated after the root-finding process is completed.

Another issue is that in the course of the MCM-based uncertainty estimation, some of the generated values of $|S_{11}|$ may prove to be greater than the maximum value $|S_{11}|$ can attain for a given set of the other model parameters. This also results in the NRM method algorithm finding an incorrect value of the dielectric constant. Nevertheless, since the value found by the algorithm is, in most cases, very far from the actual one, it can be eliminated from the output sample by applying a simple criterion. Specifically, the dielectric constant value returned by the NRM algorithm is rejected if the ratio of the difference between the actual value and the returned one to the actual value is greater than some prescribed value (threshold) set by the user. The threshold value is chosen based on the average separation between the adjacent maxima of the measurement curve. However, for large values of the MUT dielectric constant and thickness (radius), the shape of the measurement curve becomes so complex that such an approach may prove not to be effective, and therefore more sophisticated "bad dielectric constant value" rejection algorithms must be used. Since the models examined in the present study involve samples with a dielectric constant value that is not so large that the curve shape becomes very complex, the simpler of the above-mentioned approaches, i.e., the one based on the threshold is employed with a very low risk of obtaining an incorrect uncertainty estimate.

In the next chapter, conventional models and the estimation of their measurement uncertain-

ties are considered. It shows whether the model is suitable for the given set of parameter values (measurement uncertainty is acceptable) or not due to unacceptably large measurement uncertainty, e.g., above 1%. (or any other prescribed value). The effect of the sample dimensions, frequency, and dielectric constant value on the dielectric constant measurement accuracy is also addressed in this chapter, as well as possible ways of reducing measurement uncertainties.

1.2 EMCP Extraction Methods

As was mentioned in the introduction, the main focus of this thesis is the transmission/reflection method [36] of characterization of a MUT located in free space or a rectangular waveguide where it fits tightly into the waveguide cross-section. Likewise, there are cases where the MUT is located in a coaxial line and occupies the entire cross-section.

Typically, prior to performing measurements, the measurement setup is calibrated to eliminate the effect of unwanted reflections at the junctions due to mismatch, as well as the effect of the connecting cables and adapters. During the calibration process, the data is collected for the sample holder without the sample and/or employing calibration kits, including standards whose dimensions and EMCP are known with high accuracy. Then, processing of the acquired measurement data is performed, which consists in applying a number of corrections to reduce the systematic component of the dielectric constant measurement uncertainty arising due to the above-mentioned effects. Once the calibration is done, the MUT is introduced in the experimental setup, and the scattering matrix parameters of the model with the MUT are measured. For a detailed discussion and comparison of various calibration techniques, the interested reader is referred to [37–39].

The Nicolson-Ross-Weir (NRW) method [40, 41] has been used over decades as a standard technique for measuring both permittivity and permeability of homogeneous, isotropic materials. The NRW method relies on closed-form expressions for the extraction of the constitutive parameters directly from a complete set of scattering data measured for a slab made of the MUT [36, 42] using the T/R method.

However, the NRW requires a complete set of scattering matrix parameters that considerably limits its use. In the case of amplitude-only measurements, where the phases of scattering parameters are not available, or in the case of the reflection-only or transmission-only measurement method, the NRW is not applicable at all. In this case, to retrieve the EMCP of some material, one has to resort to numerical methods that iteratively reconstruct the desired EMCP. The most extensively used iterative EMCP extraction method is the Newton-Raphson (NRM) root-finding method. Various optimization algorithms are also widely employed to retrieve the EMCP of the MUT from incomplete scattering data measurements. The most extensively used optimization method are the Genetic Algorithm (GA), Particle Swarm Optimization (PSO), and other swarm intelligence-based and various evolutionary methods [43–47]. Here the term "incomplete scattering data" means that only the measured reflection or the transmission coefficient values are used to extract the EMCP, or the amplitude method is used where only magnitudes of the scattering parameters are measured.

Unfortunately, the iterative algorithms require a good initial guess to guarantee convergence to the actual solution. While in many cases, the values of the EMCP to be determined are approximately known, the iterative process may converge to an incorrect solution due to a large difference between the actual value and the approximate one used to initialize the algorithm.

Recently in a number of studies, the Artificial Neural Networks (ANN) algorithms have been applied to the raw measurement data with a view to improving the complex dielectric constant value measurement accuracy [43–45]. The use of the ANN allows for optimizing the existing analytical and numerical extraction techniques by training the underlying neural network on a large quantity of measurement data; however, to achieve satisfactory results, the data collection used for ANN training must be sufficiently large that is the main drawback of that approach.

The fundamental papers by J. Baker-Jarvis [36, 48, 49] show that the model sensitivity varies with model parameters, and in some cases, the measurement uncertainty can be prohibitively large. Nevertheless, a rigorous numerical analysis that would clearly show that a specific model has such model parameter value regions where the model is not suitable for the measurements, to the best of the author's knowledge, has not yet been presented in the literature. In the above-mentioned papers, as well as in many other papers, e.g., [2], specific properties of measurement models are not evaluated, and no attempt is made to deduce the suitability of the models from the model sensitivity coefficient prior to the measurement uncertainty analysis. Although in [36] it indicated that *"Any number of discrete measurement frequencies may be selected in this frequency range. To achieve a maximum measurement accuracy, use of different transmission line sizes and types may be required"*, the paper, in fact, addresses the effect of higher-order modes on the measurement results to ensure sufficiently high accuracy in the case of wide-band measurements, as well as provides some suggestions for choosing dimensions to ensure a single-mode regime, but nothing specific is mentioned about the optimal sample dimensions. Likewise, in [50], some attention is paid to the measurement accuracy, while the importance of the measurement model sensitivity is not taken into consideration; instead, the paper discusses various issues associated with the calibration process, which is also essential but is not always of primary concern, especially when the measurement model exhibits very low sensitivity.

Some papers describe the effect of the half-wavelength resonances on the measurement accuracy and the stability of the EMCP extraction techniques for the T/R method, as well as propose possible ways to overcome or at least mitigate these issues [51]. In [52], it is shown that for a certain set of input parameter values, such as the slab thickness and the frequency, the sensitivity coefficients of the input parameters becomes very large (in fact, they tend to infinity) resulting in unacceptably large measurement uncertainty. Also, in [52], it is shown that there are sample thickness values that yield a lower measurement uncertainty.

A similar study is presented in [53], and in an earlier contribution [54], it was shown that when the T/R method is applied to a MUT loaded transmission line, the measurement uncertainty depends significantly on the normalized (taken relative to a wavelength) sample thickness. In [55] an ANN-enhanced NRW method is proposed for stable and unique retrieval of the complex dielectric constant of low-loss materials from the data acquired with the T/R method that is

invariant to the position of the MUT in the sample holder.

In [56] an attempt was made to improve the measurement uncertainty by introducing additional weighting factors into the objective function [17] to be solved by means of an iterative method. However, the effectiveness of this approach seems questionable due to the fact that in the case when the measurement model sensitivity is not sufficiently high, adjusting the coefficient value to improve the accuracy of the EMCP extraction from the raw measurement data cannot give any significant improvement in the measurement uncertainty, as the sensitivity of the measurement model cannot be increased in this way.

It is worth noting that there are papers devoted to the EMCP extraction from the amplitude-only reflection measurement data for samples whose thickness is small compared to a wavelength which enables one to derive an analytical polynomial-based approximation ensuring unique EMCP extraction [58]. A similar idea has been used in a number of other studies concerned with the use of the T/R method for the dielectric constant retrieval when the MUT is a thin slab [59, 60].

In this thesis, it is proved that the sensitivity of the measurement models is not sufficiently high over a much wider range of the dielectric constant values not only in the vicinity of values giving the $\lambda/2$ resonances, since in the vast majority of cases, e.g., when $|S_{11}|$ peaks are sharp and the uncertainty sensitivity coefficient $1/(d|S_{11}|/d\varepsilon'_{r,\text{mut}})$ takes large values over a relatively wide range of $\varepsilon'_{r,\text{mut}}$ values. It is also demonstrated that the dielectric constant can be simply extracted without having to solve the inverse problem, which in many cases, is not a trivial task. For example, when the MUT is not a single-layer substrate but a multi-layer laminate structure or even a cylindrical rod.

Also, it is worth noting that in some studies where the MUT is a relatively thin slab, it is possible to employ analytical expressions.

Presently there is no methodology that would clearly show how to evaluate the suitability of the measurement model, as well as the measurement model sensitivity and how to make the decision regarding its suitability for performing a specific measurement when the measurements are to be performed at a specific frequency, and the MUT dimensions (thickness of the slab or the radius of the cylindrical rod) cannot be changed.

2. CONVENTIONAL MEASUREMENT MODELS

2.1 Single Slab Models

This section covers the properties, applications, advantages, and disadvantages of three conventional measurement models commonly employed in practice. One of the considered models is composed of an empty waveguide section utilized as a sample holder to accommodate a dielectric slab made of material with the dielectric constant to be determined from the measured scattering matrix elements. The second model also involves a dielectric slab. However, in contrast to the waveguide-based model, in this case, the slab is located in free space, and the dielectric constant is retrieved from the scattering data relating the amplitudes of the incident, reflected, and transmitted plane waves, as the model relies on the plane wave assumption. The third model treated in this section is a conventional model comprising a cylindrical dielectric rod made of the MUT-loaded rectangular waveguide section. Though the third model is similar to the first one, it is considerably more challenging to handle due to the absence of close-form expressions for the scattering matrix element calculation.

2.1.1 Single Slab Waveguide Measurement Model

The first step in measurement model evaluation is the evaluation of conventional measurement models involving a sample made of the MUT only [61].

In this section, the conventional measurement model consisting of a rectangular dielectric sample (slab) made of a MUT in a rectangular waveguide is considered, whereas conventional measurement models consisting of a dielectric sample (slab) in free space or a dielectric centered rod in a rectangular waveguide are treated in the following sections.

Here the waveguide measurement technique where an empty section of a rectangular waveguide employed as a sample holder [63] is examined. The effect of the sample dimensions, frequency, and dielectric constant on the dielectric constant measurement accuracy, as well as possible ways of reducing measurement uncertainties, are also addressed.

In this thesis, the measurement models are analyzed for the cases where the MUT has low losses, and it is chosen so that the magnitude of the scattering matrix element $|S_{11}|$ can be measured to determine the MUT dielectric constant. MUT losses are assumed to be known a priori (measured beforehand). This approach is common [21] and, moreover, in many studies, the MUT is treated as being lossless at all [42].

Additionally, the world leading companies manufacturing electronics testing and measurement equipment and software, as well as developing EMCP measurement methods for various materials, also develop and employ specialized low-loss material EMCP measurement methods based on the waveguide measurement techniques [7, 8]. Despite their apparent shortcomings, waveguide (transmission-line) based measurement models are quite attractive and extensively used owing to their capability to perform measurements at different frequencies - the operating frequency can be easily varied over a certain band whose width is limited only by the equipment involved [7, 8].

For the waveguide technique, it is assumed that the dielectric slab is homogeneous, the MUT

sample fills the waveguide cross-section, and there are no air gaps between the sample faces and waveguide walls. In this model, the sample has smooth, flat faces, normal to the direction of propagation (see Fig. 2.1). Also, it is assumed that the waveguide walls are perfectly conducting and the waveguide is operated in a single-mode (TE_{10}) regime, where all higher order modes are cut-off [7, 8].

These assumptions significantly simplify the mathematical model of the measurement model, thus allowing for obtaining simple closed-form expressions for the calculation of $|S_{11}|$ while not causing any significant discrepancies with experimental results.

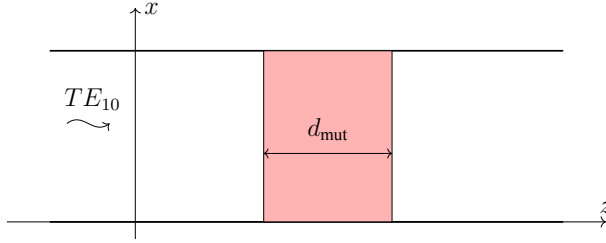


Fig. 2.1. The conventional single slab waveguide measurement model.

The mathematical model of the waveguide technique is simple and relatively easy to realize in practice.

The following expressions for the scattering matrix entries of the model involving a single dielectric slab in a waveguide (or transmission line) are widely described in the literature and can be found in many papers, e.g., [40, 65]:

$$S_{11} = e^{-j2\tilde{k}_0 L_1} \frac{R_{mut}(1 - T_{mut}^2)}{1 - R_{mut}^2 T_{mut}^2}, \quad (2.1)$$

$$S_{22} = e^{-j2\tilde{k}_0 L_2} \frac{R_{mut}(1 - T_{mut}^2)}{1 - R_{mut}^2 T_{mut}^2}, \quad (2.2)$$

$$S_{11} = e^{-j\tilde{k}_0 L_1} e^{-j\tilde{k}_0 L_2} \frac{T_{mut}(1 - R_{mut}^2)}{1 - R_{mut}^2 T_{mut}^2}, \quad (2.3)$$

where

L_1 - the distance between the front reference plane and the front face of the sample, m;

L_2 - the distance between the rear reference plane and the rear face of the sample, m;

$T_{mut} = e^{-j\tilde{k} d_{mut}}$ - the transmission coefficient;

$R_{mut} = (\tilde{k}_0 - \tilde{k}) / (\tilde{k}_0 + \tilde{k})$ - the interfacial reflection coefficient at slab faces;

$\tilde{k}_0 = \sqrt{k_0^2 - (\pi/a)^2}$ - the TE_{10} mode waveguide wavenumber in the air-filled region, 1/m;

$\tilde{k} = \sqrt{k_0^2 \varepsilon_{r,mut} - (\pi/a)^2}$ - the TE_{10} mode waveguide wavenumber in the dielectric-filled region, 1/m;

$\varepsilon_{r,mut} = \varepsilon'_{r,mut} (1 - j \tan \delta_{mut})$ - the complex dielectric constant in the dielectric-filled region;

$k_0 = 2\pi f/c$ - the free space wavenumber, 1/m;
 c - the speed of light, m/s.

For the sake of convenience, the symbols used to denote the single slab waveguide measurement model parameters are summarized in Table 2.1.

Table 2.1
 Single slab waveguide model parameters

Model Parameter	Symbol
MUT dielectric constant	$\epsilon'_{r,\text{mut}}$
MUT loss tangent	$\tan \delta_{\text{mut}}$
MUT slab thickness	d_{mut}
Frequency	f
Waveguide width	a

In the present study, it is assumed that the front and rear reference planes are aligned with the front and rear faces of the slabs, respectively. Hence, $L_1 = 0$ and $L_2 = 2$.

For non-magnetic materials, if the position of the reference planes is not known precisely, factors $e^{-j\tilde{k}_0 L_1}$ and $e^{-j\tilde{k}_0 L_2}$ can be eliminated from the relations giving reference plane invariant equations to extract the EMCP of the MUT [63]. Although there exists an entire family of reference plane independent equations, the most commonly used ones (owing to their particular usefulness) are as follows

$$|S_{11}| = \left| \frac{R_{\text{mut}}(1 - T_{\text{mut}}^2)}{1 - R_{\text{mut}}^2 T_{\text{mut}}^2} \right|, \quad (2.4)$$

$$|S_{21}| = \left| \frac{T_{\text{mut}}(1 - R_{\text{mut}}^2)}{1 - R_{\text{mut}}^2 T_{\text{mut}}^2} \right|. \quad (2.5)$$

The primary focus of this thesis is cases where the dimensions of the MUT cannot be changed, and the measurements are made at a fixed frequency chosen according to standards. However, if it is necessary to perform measurements at multiple frequencies, the only obstacle that stands in the way is ensuring that the waveguide is operated in a single-mode regime.

The requirement that the sample must fit tightly in the waveguide cross-section is a significant drawback of the method, but the advantages are the simplicity of the measurements and the availability of closed-form expression for the scattering matrix calculation. Furthermore, the model is easy to realize to perform measurements at a given frequency and allows for measuring the temperature dependence of the dielectric constant. The gap between the MUT slab and waveguide walls is discussed in many papers [66, 67]. In practice, it was found that the effect of the air-gap on the scattering matrix parameters, resulting from the excitation of higher order modes in the dielectric-filled region, can be significantly mitigated by filling the gaps with a

high conductivity paste.

A typical measurement model using the transmission-line method comprises a VNA, a waveguide serving as a sample holder, and software for dielectric constant extraction. There are a number of dielectric constant extraction techniques and uncertainty estimation methods [64]. The waveguide dielectric constant measurement technique is one of the most widely employed ones for being simple, and cost-effective [68, 69]. Also, commercial software is available, such as the N1500A Materials Measurement Suite [70] featuring nine different dielectric constant extraction algorithms, so that the user can select the one which is more suitable for a particular measurement model, MUT, and applications [40, 71, 72]. Some iterative techniques are also extensively employed despite the fact that they require a good initial guess as described in [70].

In the numerical analysis of the measurement model under consideration, it is assumed the model is based on a standard rectangular waveguide WR-90 with a width of the broader wall of 22.86 mm and the measurements are performed at 10 GHz. It should be noted, however, that the research methodology can be applied just as well to models involving waveguides of different dimensions and operating at different frequencies.

First, examine how the actual value of the MUT dielectric constant affects the measurement uncertainty of the conventional waveguide model. To that end, two models, denoted MUT1 and MUT2, are analyzed. The models have the same parameter values except $\epsilon'_{r,\text{mut}}$, which for the first model (MUT1) is set equal to 10.2 and for the second model (MUT2) is equal to 4.3 (see Table 2.2).

Table 2.2

Model parameters for two single slab models

Model Parameter	Symbol	Value
MUT1 dielectric constant	$\epsilon'_{r,\text{mut1}}$	10.2
MUT1 loss tangent	$\tan \delta_{\text{mut1}}$	0.0023
MUT1 slab thickness	d_{mut1}	2.5 mm
MUT2 dielectric constant	$\epsilon'_{r,\text{mut2}}$	4.3
MUT2 loss tangent	$\tan \delta_{\text{mut2}}$	0.003
MUT2 slab thickness	d_{mut2}	2.5 mm
Frequency	f	10 GHz
Waveguide width	a	22.86 mm

In this example, as well as the other examples presented in this section, the interval-based uncertainty estimation is used in place of the conventional point estimation for being more illustrative; namely, the amount of the measurement uncertainty of the measurable quantity (MUT dielectric constant) and its dependence on the steepness of the curve can be easily deduced just by looking at the measurement curve graph accompanied by horizontal and vertical bars representing the confidence intervals for $|S_{11}|$ and $\epsilon'_{r,\text{mut}}$, respectively.

Most standards require stating the expanded measurement uncertainty with the factor $k = 2$

(expanded uncertainty is k times the standard uncertainty) in lieu of the standard uncertainty, which is equal to the standard deviation for the measurable quantity. This choice is dictated by the fact the interval $[-\text{expanded uncertainty}, +\text{expanded uncertainty}]$ coincides with the confidence interval with the confidence level of 95 % for a normal distribution (typically in standards, it is assumed that the measurable quantity follows a normal distribution unless some more sophisticated uncertainty estimation method is utilized, such as the MCM, which considers the distribution of the measurable quantity, as well). The confidence level of a confidence interval corresponds to the probability of the measurable quantity estimate to be within the interval. This means that the value of the measurable quantity is within the $k = 2$ confidence interval with the probability of approximately 95 %. The purpose of this example is not to properly estimate the measurement uncertainty but to illustrate the effect of the model measurement curve steepness on the uncertainty, namely, to show how the width of the confidence interval for $\varepsilon'_{r,\text{mut}}$ depends on the model parameters. Therefore it is not mandatory to choose the confidence level of 95 % for the confidence interval for $|S_{11}|$.

In this thesis $\Delta|S_{11}|$ and $\Delta\varepsilon'_{r,\text{mut}}$ refer to the confidence interval widths for $|S_{11}|$ and the actual value of the MUT dielectric constant, $\varepsilon'_{r,\text{mut}}$, respectively. In this example, it is assumed that $|S_{11}|$ is a random quantity following a normal distribution, and $\Delta|S_{11}|$ is chosen to be equal to two standard deviations, which corresponds to the confidence level (probability) of approximately 68 % (corresponds to $k = 1$). Also, for both models, it is assumed that $\Delta|S_{11}| = 0.010$.

Fig. 2.2 shows $|S_{11}|$ plotted as a function of $\varepsilon'_{r,\text{mut}}$ for a single slab model.

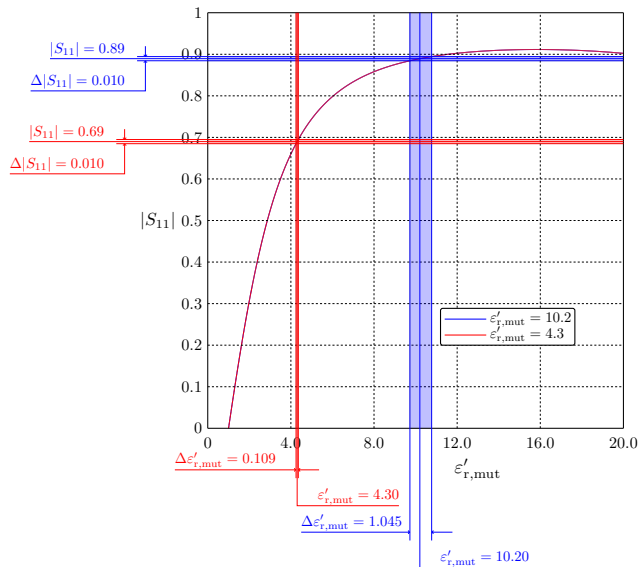


Fig. 2.2. $|S_{11}|$ as a function of $\varepsilon'_{r,\text{mut}}$ for the single slab waveguide model and the confidence intervals for $\varepsilon'_{r,\text{mut}} = 10.2$ and $\varepsilon'_{r,\text{mut}} = 4.3$.

It should be noted that if the confidence level of 95 % were chosen, the width of the cor-

responding interval for $\varepsilon'_{r,\text{mut}}$ would be even wider. Also, the figure displays the confidence intervals with the confidence level of 68% evaluated for two models with different values of $\varepsilon'_{r,\text{mut}}$. The values of the other model parameters of these two models are the same (see Table 2.2).

The blue and red curves, as well as horizontal and vertical bars correspond to the models with $\varepsilon'_{r,\text{mut}} = 10.2$ and $\varepsilon'_{r,\text{mut}} = 4.3$, respectively. The widths of the horizontal bars are equal to the widths of the corresponding confidence intervals for $|S_{11}|$, while the widths of the vertical bars correspond to the widths of the confidence intervals for $\varepsilon'_{r,\text{mut}}$.

As can be seen in Fig. 2.2, the confidence interval width for the measured dielectric constant value, $\Delta\varepsilon'_{r,\text{mut}}$, for the model with $\varepsilon'_{r,\text{mut}} = 4.3$ is considerably narrower than for the model with $\varepsilon'_{r,\text{mut}} = 10.2$. Thus, measuring the dielectric constant using the model with $\varepsilon'_{r,\text{mut}} = 4.3$ results in a measurement uncertainty that is by an order of magnitude smaller than when the measurements are made for the MUT with $\varepsilon'_{r,\text{mut}} = 10.2$. Specifically, values of $\varepsilon'_{r,\text{mut}}$ at which the steepness of the curve is high result in a lower measurement uncertainty than those at which the steepness is low.

This behavior of the model can be explained by the expression for the measurement uncertainty (formula (1.2)). The expression clearly shows the total measurement uncertainty is inversely proportional to the model sensitivity coefficient, which means that for models with a very small model sensitivity coefficient, the dielectric constant measurement uncertainty will be exceedingly large even when the contribution of the other model parameters is small.

Thus, this example shows that the suitability of the conventional measurement model (the same also holds for non-conventional models) can be conveniently evaluated based on the function graph of the derivative $\frac{\partial |S_{11}|}{\partial \varepsilon'_{r,\text{mut}}}$. The main advantage of the model sensitivity-based model evaluation is that it does not require any cumbersome mathematical expressions and time-consuming computations - only the forward problem needs to be solved. This proves the first of the theses put forth by the author, namely, the one concerning the possibility of performing the measurement model suitability evaluation in a simple, convenient, and time-efficient manner when the model parameters cannot be altered for various reasons.

Now, examine how the thickness of the MUT affects the measurement uncertainty. To do so, two single slab waveguide models having the same parameter values except for the MUT thickness, d_{mut} , which is varied in this case, are considered. The MUT thickness of one of the models is set equal to 2.5 mm, while that of the other is 0.635 mm. The dielectric constant and the loss tangent for both models are the same and are equal to 10.2 and 0.0023, respectively. The frequency and the width of the waveguide are the same as in the previous example (see Table 2.2). Similarly to the previous example, the confidence interval concept is utilized to demonstrate the effect of the model parameters (in this case d_{mut}) on the measurement uncertainty.

Fig. 2.3 shows $|S_{11}|$ as a function of $\varepsilon'_{r,\text{mut}}$ calculated for both models. Also, the figure displays the confidence intervals with the confidence level of 68% for both models. The width of the confidence interval for $|S_{11}|$ in this case is set equal to 0.02 for both models ($\Delta|S_{11}| = 0.02$).

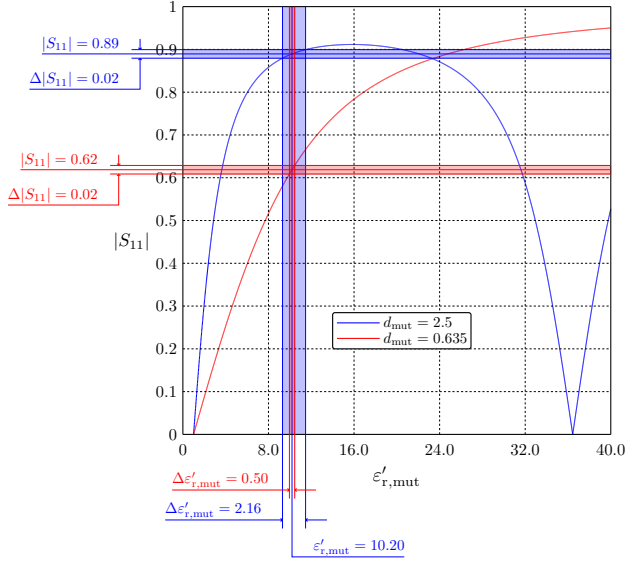


Fig. 2.3. $|S_{11}|$ as a function of $\varepsilon'_{r,\text{mut}}$ for two different values of $d_{r,\text{mut}}$ and the corresponding confidence intervals.

The blue and red curves, as well as horizontal and vertical bars, correspond to the models with $d_{\text{mut}} = 2.5$ and $d_{\text{mut}} = 0.635$, respectively. The widths of the horizontal bars are equal to the widths of the corresponding confidence intervals for $|S_{11}|$, while the widths of the vertical bars correspond to the widths of the confidence intervals ($u_{\varepsilon'_{r,\text{mut}}} = \Delta\varepsilon'_{r,\text{mut}}$ in the figures) for $\varepsilon'_{r,\text{mut}}$.

Fig. 2.3 shows that the measurement uncertainty of the dielectric constant depends considerably on d_{mut} . In the present example, the steepness for the model with $d_{\text{mut}} = 2.5$ mm is appreciably lower than for the model with $d_{\text{mut}} = 0.635$ mm; as a result, the confidence interval for $d_{\text{mut}} = 2.5$ mm is more 6 times wider than for the model with the MUT thickness of 0.635 mm.

The measurement uncertainty can also be reduced by changing the frequency at which measurements are performed; however, in some practical cases the frequency must be kept fixed, e.g., when one needs to determine a dielectric constant at a frequency specified in standards.

As can be seen, the measurement uncertainty depends on all model input parameters, and changing the model parameters can improve the sensitivity of the model. However, in most cases, measurements must be made at given parameters, which means that measurements must be made at a fixed frequency without changing the size of the MUT sample, and therefore the most significant effect has $\frac{\partial |S_{11}|}{\partial \varepsilon'_{r,\text{mut}}}$ value and the uncertainty $u_{|S_{11}|}$ should be as small as possible, but it is limited by the capabilities of the measuring system.

Similar model behavior, as described above, is also exhibited by other measurement models. As can be seen, the measurement uncertainty varies with the MUT dielectric constant, as well as the slab thickness and the measurement frequency. However, in this thesis, these parameters are

treated as fixed, as it is assumed that the dielectric constant of a given value must be measured (it is known approximately). The measurements are performed at a given MUT thickness and frequency.

2.1.2 Single Slab Free Space Measurement Model

In this section, the conventional model for the free-space method is considered. The general principles and parameters of the measurements are similar to those of the previously discussed waveguide method. Since most of the papers cited above also refer to free-space technique measurements, only those not mentioned above and related to the free-space dielectric constant measurement technique will be discussed in this section.

In this thesis, only those models using plane electromagnetic waves incident normal to the MUT surface are considered. In the conventional model, the MUT is a plane-parallel dielectric slab whose broad faces are normal to the wave propagation direction (see. Fig. 2.4)

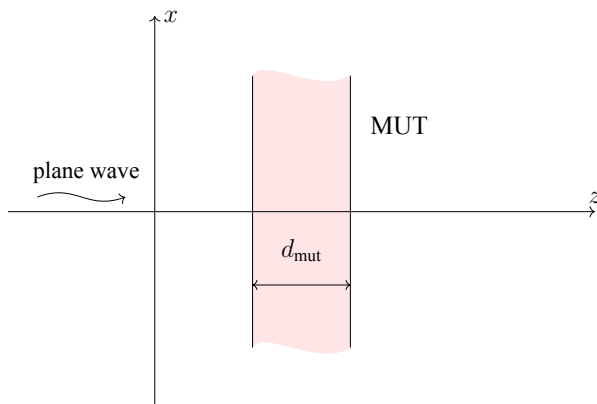


Fig. 2.4. The conventional free space technique measurement model.

Similar to section 2.1.2, the MUT dielectric constant, $\epsilon'_{r,\text{mut}}$, is retrieved from the magnitude of the scattering matrix element S_{11} , $|S_{11}|$. As before, it is assumed that the MUT losses are low and are known a priori (measured beforehand). This approach is commonly employed in studies of free space techniques [73, 74].

For the free space technique, it is assumed that the MUT sample is a large homogeneous dielectric slab with flat parallel faces [75].

In the mathematical model, the slab is assumed to have infinite transverse dimensions and a finite thickness. Such assumptions significantly simplify the mathematical model of the measurement model. The magnitude of the scattering matrix element S_{11} , $|S_{11}|$ is calculated using formula (2.4) $|S_{11}| = \left| \frac{R_{\text{mut}}(1 - T_{\text{mut}}^2)}{1 - R_{\text{mut}}^2 T_{\text{mut}}^2} \right|$, where for a nonmagnetic slab in free space $T_{\text{mut}} = e^{-jk d_{\text{mut}}}$ is the transmission coefficient in free space, $R_{\text{mut}} = \frac{\eta - \eta_0}{\eta + \eta_0} = \frac{1 - \sqrt{\epsilon_r}}{1 + \sqrt{\epsilon_r}}$ is the interfacial reflection coefficient at slab faces, η - intrinsic impedance of MUT medium, Ω ; η_0 - intrinsic impedance of free space, Ω .

The main advantages of the free space technique models are the ability to perform the measurements in a non-contacting and non-destructive manner over a wide range of frequencies and temperatures [7]. The free space technique is widely used in the measurement of dielectric constant of construction materials [73].

The lowest frequency is limited by antenna capabilities and sample dimensions. In many studies, it is assumed sufficient for the sample to have transverse dimensions that are at least three wavelengths in the MUT material. If these conditions are fulfilled, the mathematical model can be constructed for a slab with infinite transverse dimensions, which, in turn, allows for using closed-form expressions for the scattering matrix element calculation.

In [76] a theoretical model was developed to study, in a very general way, the limitations of the plane-wave approximation. The use of lens-equipped horn antennas [77] has also been shown to effectively reduce the edge diffraction effect. Rather complex cases are also studied for finite-size rectangular dielectric cuboid samples [78, 79].

Some commercially available full-wave simulation software can be employed to treat the scattering of waves by a dielectric slab of finite transverse dimension and calculate scattering matrix elements; however, such computations can be accomplished in a reasonable time frame only for slabs with sufficiently small dimensions, but in this case, a problem arises - the sample holder used to fix the position of the slab will affect the result. On the other hand, when the transverse dimensions of the slab are greater than five wavelengths, the simulation time is so long that the correct evaluation of the measurement uncertainty becomes practically unrealistic.

Conventional measurement methods based on the free space technique for the metal-backed dielectric sample measurements are also employed in practice - the dielectric constant in these methods is extracted from the reflection coefficient for a dielectric slab (MUT), whose rear face is completely covered by a thin metal layer [80].

A free space technique for frequency-by-frequency solution or a multi-frequency reconstruction is described in [81], but the measurement considered in this thesis are assumed to be performed at a given fixed frequency.

Similar to section 2.1.2, two important cases are considered for the free space method at the frequency of $f = 10$ GHz:

1) The thickness of the dielectric slab is constant, but the dielectric constant of the model MUT is varied. The results are indicated in Fig. 2.5;

2) The constitutive parameters of the dielectric slabs (MUTs) are the same (with an a priori known expected value of the MUT dielectric constant), but the thicknesses of the slabs are different. The relevant results are shown Fig. 2.6;

The values of the model parameters used in the numerical calculations whose results are displayed in Fig. 2.5 are presented in Table 2.3.

Table 2.3

Two single slab free space model parameters

Model Parameter	Symbol	Value
MUT1 dielectric constant	$\epsilon'_{r,\text{mut1}}$	30
MUT1 loss tangent	$\tan \delta_{\text{mut1}}$	$6.67 \cdot 10^{-5}$
MUT1 slab thickness	d_{mut1}	2.5 mm
MUT2 dielectric constant	$\epsilon'_{r,\text{mut2}}$	4.3
MUT2 loss tangent	$\tan \delta_{\text{mut2}}$	0.003
MUT2 slab thickness	d_{mut2}	2.5 mm
Frequency	f	10 GHz

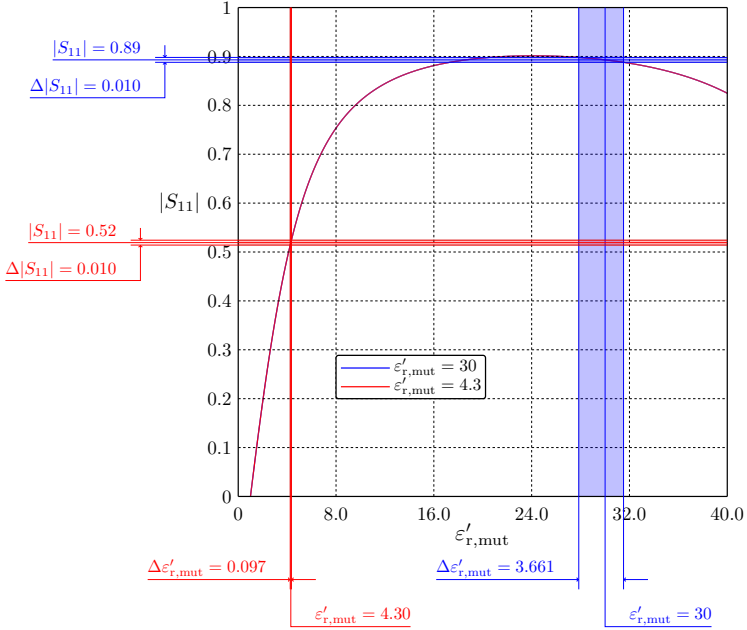


Fig. 2.5. $|S_{11}|$ as a function of $\epsilon'_{r,\text{mut}}$ and the confidence intervals for samples with two different $\epsilon'_{r,\text{mut}}$.

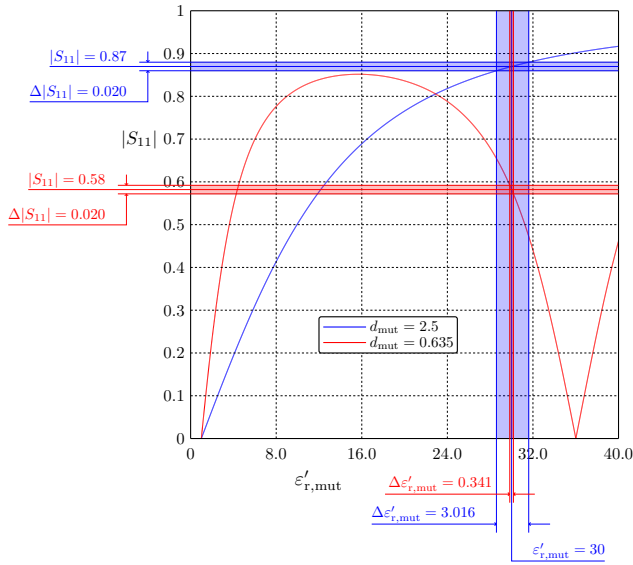
The values of the model parameters used in the numerical calculations whose results are displayed in Fig. 2.6 are presented in Table 2.4.

The results are similar to those of subsection 2.1.2. The figures show that for the models where the MUT is a homogeneous slab, and the dielectric constant is determined from the measured $|S_{11}|$, the measurement uncertainty depends on both the expected value of the dielectric constant and the thickness of the slabs. Furthermore, changing the frequency can affect the model sensitivity since $|S_{11}|$ is a function of d_{mut}/λ (the same applies to the model based on the waveguide technique as described in subsection 2.1.2).

Table 2.4

Single slab free space model parameters

Model Parameter	Symbol	Value
MUT dielectric constant	$\varepsilon'_{r,\text{mut}}$	30
MUT loss tangent	$\tan \delta_{\text{mut}}$	$6.67 \cdot 10^{-5}$
MUT slab thickness 1	$d_{\text{mut}1}$	2.5 mm
MUT slab thickness 2	$d_{\text{mut}2}$	0.625 mm
Frequency	f	10 GHz

Fig. 2.6. $|S_{11}|$ as a function of $\varepsilon'_{r,\text{mut}}$ and the confidence intervals for two different $d_{r,\text{mut}}$.

In both cases, a separate calculation must be performed to evaluate the suitability of the model for a set of specific parameter values (dielectric constant, layer thickness, frequency). At certain parameter values, the model may exhibit a sufficiently high sensitivity, which gives a small measurement uncertainty, but at the same time, there are also ranges of the model parameter values that give very low sensitivity, which means that there are regions where the measurement uncertainty is unacceptably high.

It should be noted that these results show that it is less likely that the expected measurement uncertainty, as well as the measurement model suitability, were considered in papers proposing measurement methods for a wide frequencies band, e.g., [69, 74, 79].

2.2 Single Rod Waveguide Measurement Model

2.2.1 Overview of Single Rod Models

The characterization of cylindrical samples has gained interest owing to the fact that they are easy to machine as compared to their rectangular counterparts [82, 83]. However, in contrast to the slab-shaped sample entirely filling the waveguide cross-section, in this case, closed-form mathematical expressions for the evaluation of the scattering matrix are not available. Although some analytical expressions or simplified equations for solving the forward scattering problem involving a cylindrical rod in a rectangular waveguide have been presented, all of them are derived from Maxwell's equation based on a number of simplifying assumptions. This, however, limits the applicability of the expressions; typically, the expressions ensure satisfactory accuracy of the scattering parameter calculation only for dielectric rods with a diameter much smaller than a wavelength in the rod material. However, in many cases, one needs to measure the ready-to-use product, such as a cylindrical dielectric resonator whose diameter is not electrically small and which must be subjected to non-destructive characterization. In some recent studies, an interesting measurement configuration was utilized [84] where the dielectric constant of a liquid was measured using a flexible pipe passing through two holes made in the broader waveguide walls so that the resulting structure may be treated as a rectangular waveguide with a cylindrical full-height tubular (two-layer) sample whose outer layer is the pipe wall, whereas the liquid pushed through the pipe using a pump and taken from a special reservoir is regarded as the inner layer (core).

An accurate and elegant method for measurement of the dielectric constant of cylindrical objects with arbitrary cross-section is presented [85]. The method relies on expressing the scattered fields in terms of a volume integral over the extent of the MUT, resulting in the integral formulation that is discretized using the Method of Moments. However, in place of solving the resulting system of equation, the eigenanalysis is applied to it, giving a partial fraction representation of the TE_{10} mode reflection coefficient. However, the eigenvalues and eigenvectors of the matrix must be evaluated to construct such an approximation which is quite a time-consuming process, especially when the number of the eigenpairs is large, which limits the use of the method to electrically thin samples. The method is very convenient, as to extract the value of the dielectric constant, one just needs to find the roots of a polynomial obtained by equating the approximate reflection coefficient to the measured one. The roots of the resulting polynomial are found numerically via the use of the conjugate gradient method. Various practical aspects of the dielectric measurement using that technique are also treated in that paper.

In [86], a generic approach for determining the complex permittivity of dielectric materials based on a rectangular waveguide measurement technique is reported. The method first calculates the MUT scattering parameters, whose dielectric constant may take a wide range of values and is known a priori. The forward scattering problem is solved using a unified theory based on a combination of the boundary integral equation technique and the modal expansion approach. The paper presents generic diagrams interrelating the dielectric constant and the measured scat-

tering parameters, and a simple analytical expression was deduced to solve the inverse problem using an easy-to-use analytical formulation. The method requires an a priori knowledge of the MUT dielectric constant and generates a number of diagrams to visualize how the complex dielectric constant varies with the real and imaginary parts of the measured scattering matrix parameters. This way is faster than graphical and iterative approaches.

In [87] an elegant way for the dielectric constant retrieval from the measured set of scattering matrix parameters is proposed. The method relies on a mode-matching-based forward problem solution originally proposed by Sahalos [90] and subsequently improved by Abdulnour [91]. One of the two discontinuities treated in that work is a cylindrical dielectric sample for the analysis of which easy-to-use expressions were derived that outperform iterative methods. Also, as indicated in [87], the methodology can be extended to handle samples with shapes other than cylindrical - a different method for solving the underlying forward problem is needed. In [88] dielectric constant measurements of liquid materials with a tubular sample holder are addressed, and an extension of the method proposed in [87] was developed to analyze a specialized sample holder designed for making measurements at high temperatures. The extended method is based on Abdulnour's extraction model for a cylindrical sample piercing through the broader walls of a rectangular waveguide (WR340 standard). Subsequently, an analytical model for dielectric constant measurements was improved [89] by exploiting the fact that the relation between S_{21} and the MUT dielectric constant resembles a bi-linear transform, which appreciably accelerates the time-consuming optimization process.

In this thesis for the uncertainty analysis of single rod models, the method of Sahalos-Abdulnour [90–92] is utilized, as this method is more rapid than that proposed by Sarabandi [85]. More specifically, Sarabandi's method is more general - it is based on the MoM and therefore is capable of treating not only cylindrical samples with circular cross-sections but also cylindrical samples with an arbitrary cross-section; however, this advantage of Sarabandi's method comes at the expense of higher computational burden. The Sahalos-Abdulnour method, by contrast, is a semi-analytical method developed to address scattering by full-height cylindrical rods only, and therefore it is considerably more rapid than its MoM-based counterpart.

Alternatively, the choice of the method is entirely dictated by the amount of CPU time needed to solve the corresponding forward scattering problem since this aspect is crucial in the MCM-based uncertainty estimation to obtain reliable estimates. An in-depth discussion of various methods for scattering matrix element calculation for a cylindrical object in a rectangular waveguide is presented in chapter 6 of the thesis.

2.2.2 Uncertainty Analysis of Single Rod Model

Examine a conventional model consisting of a dielectric sample (cylindrical rod) in a rectangular waveguide made of the material whose dielectric constant is to be measured. The geometry of the model under consideration is depicted in Fig. 2.7. It is assumed that the dielectric slab is homogeneous and the waveguide walls are perfectly conducting. These assumptions significantly simplify the mathematical model of the measurement model - allow for obtaining simple

analytical expressions for S_{11} , but do not cause a significant deviation from the experimental results.

As in the case slab model examined above, here, the impact of the MUT dielectric constant on the measurement uncertainty is analyzed first. Two dielectric rod waveguide models having the same parameter values other than the dielectric constant are attested. MUT1 and MUT2 refer to the models with $\varepsilon'_{r,\text{mut}} = 10.2$ and 4.3, respectively (see Table 2.5).

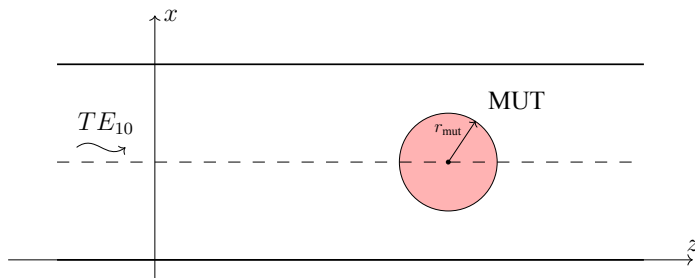


Fig. 2.7. The geometry of the conventional single rod measurement model.

Table 2.5

Two single rod waveguide model parameters

Model Parameter	Symbol	Value
MUT1 dielectric constant	$\varepsilon'_{r,\text{mut1}}$	10.2
MUT1 loss tangent	$\tan \delta_{\text{mut1}}$	0.0023
MUT1 rod radius	d_{mut1}	2.5 mm
MUT2 dielectric constant	$\varepsilon'_{r,\text{mut2}}$	4.3
MUT2 loss tangent	$\tan \delta_{\text{mut2}}$	0.003
MUT2 rod radius	d_{mut2}	2.5 mm
Frequency	f	10 GHz
Waveguide width	a	22.86 mm

It is assumed that $|S_{11}|$ is a random quantity following a normal distribution, and $\Delta|S_{11}|$ is chosen to be equal to two standard deviations, which corresponds to the confidence level of about 68 % (equivalent to $k = 1$). In addition, one assumes that for both models, $\Delta|S_{11}| = 0.01$. It should be noted that if the confidence level of 95 % were chosen, the width of the corresponding interval for $\varepsilon'_{r,\text{mut}}$ would be even wider.

Fig. 2.8 shows $|S_{11}|$ plotted as a function of $\varepsilon'_{r,\text{mut}}$ for a single rod model. Also, the figure displays the confidence intervals with the confidence level of 68 % evaluated for two models with different values of $\varepsilon'_{r,\text{mut}}$. The values of the other model parameters of these two models are the same (see Table 2.4). The blue and red curves, as well as the horizontal and vertical bars, correspond to the models with $\varepsilon'_{r,\text{mut}} = 10.2$ and $\varepsilon'_{r,\text{mut}} = 4.3$, respectively. The widths of the horizontal bars are equal to the widths of the corresponding confidence intervals for $|S_{11}|$, while

the widths of the vertical bars correspond to the widths of the confidence intervals for $\varepsilon'_{r,\text{mut}}$.

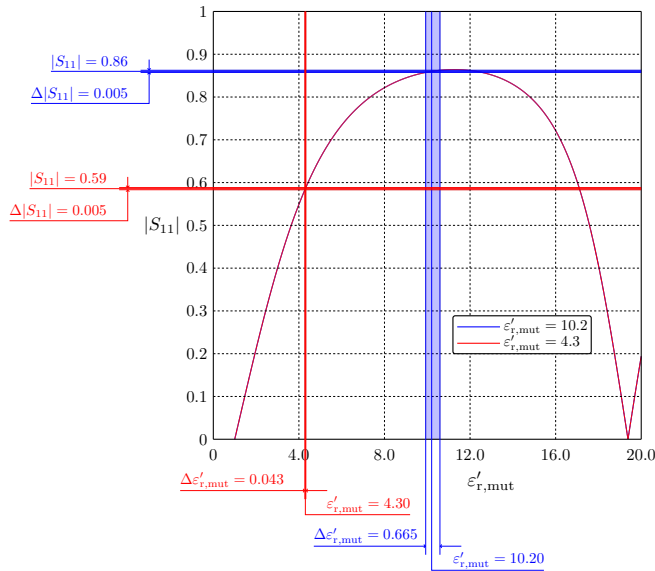


Fig. 2.8. $|S_{11}|$ as a function of $\varepsilon'_{r,\text{mut}}$, and confidence intervals for a model with a cylindrical sample in a waveguide calculated at two different values of $\varepsilon'_{r,\text{mut}}$.

Two single-rod waveguide models are studied to examine the effect of the MUT radius on the measurement uncertainty. The models have the same parameter values except for the MUT radius, r_{mut} , which is varied in this case. The MUT radii of the models are set equal to 2.5 mm and 0.635 mm, respectively. For both models under study, the dielectric constant and the loss tangent are 10.2 and 0.0023, respectively. The frequency and the width of the waveguide are the same as in the previous example (see Table 2.6). Similarly to the previous example, the confidence interval concept is utilized to demonstrate the effect of the model parameters (in this case r_{mut}) on the measurement uncertainty.

Table 2.6

Single rod waveguide model parameters

Model Parameter	Symbol	Value
MUT dielectric constant	$\varepsilon'_{r,\text{mut}}$	10.2
MUT loss tangent	$\tan \delta_{\text{mut}}$	0.0023
MUT rod radius 1	$r_{\text{mut}1}$	2.5 mm
MUT rod radius 2	$r_{\text{mut}2}$	2.0 mm
Frequency	f	10 GHz
Waveguide width	a	22.86 mm

Fig. 2.9 shows $|S_{11}|$ plotted as a function of $\varepsilon'_{r,\text{mut}}$ for the single rod model with two different

radii of the rod, while the other model parameters are kept fixed. The blue and red curves, as well as horizontal and vertical bars, correspond to the models with $r_{\text{mut}} = 2.5$ and $r_{\text{mut}} = 2.0$, respectively. The widths of the horizontal bars are equal to the widths of the corresponding confidence intervals for $|S_{11}|$, while the widths of the vertical bars correspond to the widths of the confidence intervals for $\varepsilon'_{r,\text{mut}}$.

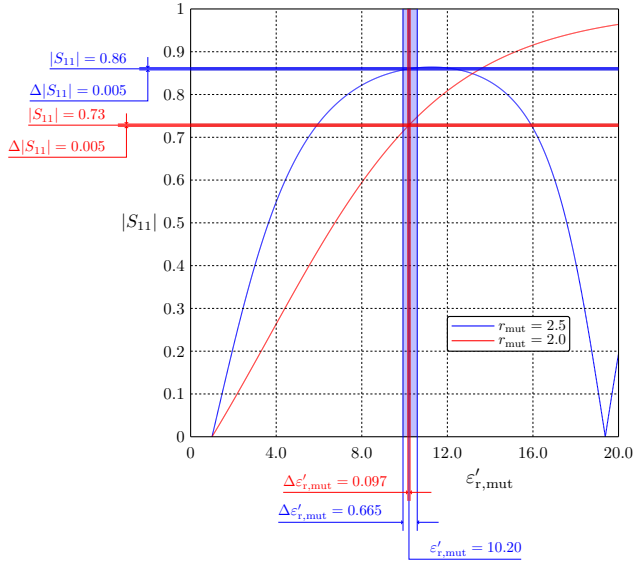


Fig. 2.9. $|S_{11}|$ as a function of $\varepsilon'_{r,\text{mut}}$ for different values of $r_{r,\text{mut}}$.

As can be observed in Fig. 2.9, similar to the slab models considered above, the measurement uncertainty of the dielectric varies considerably with r_{mut} . In this example, the steepness for the model with $r_{\text{mut}} = 2.5$ mm is significantly lower than for the model with $r_{\text{mut}} = 2.0$ mm. The confidence interval for $r_{\text{mut}} = 2.5$ mm is approximately 6.8 times wider than for the model with the MUT radius of 2.0 mm.

2.3 Summary

The analysis of three conventional models shows that for each model, there are model parameter values that give unacceptably large measurement uncertainty, and therefore one should avoid using them. This fact emphasizes the importance of quick and effective measurement model suitability evaluation. Such an evaluation can be accomplished by calculating the model sensitivity coefficient, which is a very computationally efficient way of evaluating measurement models. One does not need to solve the inverse problem and resort to computationally demanding uncertainty estimation algorithms to carry out the sensitivity-based evaluation of a measurement model. Instead, one needs to calculate and plot the model sensitivity coefficient, which, in fact, is the derivative of $|S_{11}|$ with respect to the MUT dielectric constant and can be determined by solving the forward problem only.

3. MULTI-SLAB WAVEGUIDE MEASUREMENT MODEL

3.1 Overview of Extended and Optimized Measurement Models

A number of studies have been carried out with a view to improving the existing conventional measurement models in terms of dielectric constant measurement accuracy. For example, in [19] it is demonstrated that for a shielded dielectric resonator of cylindrical shape, there are values of its radius at which the measurement uncertainty attains a value that is lower than for cylinders with a different radius value. Alternatively, it is possible to minimize the dielectric constant measurement uncertainty by testing samples with optimized dimensions. In [19] the measurement uncertainty is estimated by using the MCM, which is more reliable, as demonstrated in [23]. In [93], and [94], a similar analysis was applied to measurement models consisting of a single dielectric obstacle and two dielectric obstacles in a rectangular waveguide, respectively. In both cases, the obtained results indicate that there exist optimal model parameters that minimize the measurement uncertainty.

Dester in his doctoral thesis, performed a comprehensive investigation, including a thorough measurement uncertainty analysis, of the two-layer, two-thickness, and two-iris waveguide probe methods for measuring conductor-backed materials [18]. His findings also show that measurement uncertainty can be reduced by choosing optimal measurement model dimensions and by extending the original model so that the extended one provides lower measurement uncertainty.

An efficient procedure for finding the optimal value of the β coefficient, appearing in the objective function proposed by Baker-Jarvis [71] to retrieve the MUT dielectric constant for a conventional model composed of a single slab in a rectangular waveguide or coaxial transmission, is proposed in [20]. However, the EPM was used to estimate the uncertainty, and the method is based on a mathematical trick that improves the uncertainty due to the objective function, not the actual measurement uncertainty of the measurement model. Furthermore, in [20], the dielectric constant is extracted from the complete set of complex scattering parameters, but the measurement uncertainties associated with the scattering parameter phase measurements are larger than those of their absolute values, which means that one should avoid using phaseless measurements to achieve higher measurement accuracy. Since, in the vast majority of practical cases, the value of the dielectric constant is approximately known beforehand, the dielectric constant extraction from the measured absolute values of the scattering parameters by means of some simple root-finding algorithm, such as the NRM gives a value that is very close to the actual one and only slightly differs from it due to the measurement uncertainty. In the case of low-loss material measurements, it suffices to measure only $|S_{11}|$ as the other scattering matrix parameters do not provide any additional information about the MUT dielectric constant.

3.2 Two-Slab Waveguide Measurement Model

3.2.1 Extended Model

In this section, an efficient methodology for the uncertainty reduction in nondestructive dielectric constant measurements based on the waveguide technique [133] is proposed and discussed in detail, as well as a numerical study is carried out to demonstrate its effectiveness. The model is also investigated in one of the author's papers [131].

It should be noted that the proposed methodology is intended for measurements of dielectric constant only; it is not intended for loss tangent measurements since the proposed methodology, unfortunately, cannot guarantee a high accuracy in the MUT loss tangent measurements.

For example, the conventional model for slab-based waveguide measurement technique is a model consisting only of a sample made of the material whose dielectric constant is to be measured, placed in an empty section of a rectangular waveguide serving as a sample holder.

3.2.2 Uncertainty Reduction

By the very definition of the model sensitivity, it is parameter dependent; namely, the derivatives of the measurable quantity are also functions of the measurement model parameters, not only the measurable quantity itself. For some models, sensitive coefficients do not exhibit larger variations when one or more parameters are being varied, while for some models, values may differ considerably. Alternatively, it may happen that for certain values of the model parameters, i.e., for a certain combination of frequency and thickness, as well as other parameters, the sensitivity will be so low that it will not be possible to make measurements. On the other hand, this also implies that there may exist optimal sets of parameters giving higher sensitivities and, therefore, higher measurement accuracy.

Typically, conventional and simple measurement models (one-slab models) do not ensure the required sensitivity at a particular frequency and for a specific thickness of the slab made of the material under test MUT. This problem can be mitigated by optimizing the original measurement model, i.e., by reducing the sensitivity of the quantity being measured to the model parameter (dimensions, constitutive properties) values.

In case the interval of possible dielectric constant values coincides or overlaps with a low-sensitivity region of the conventional measurement model, the measurement uncertainty will be substantial. To mitigate this problem, one needs to alter the shape of the measurement curve so that the sensitivity coefficient of the extended measurement model $\frac{\partial |S_{11}|}{\partial \varepsilon'_{r,\text{mut}}}$ is sufficiently large in the interval of possible values of the measured quantity. The main idea of the proposed methodology is to achieve a significant reduction in the measurement uncertainty by increasing the steepness of the curve, thereby increasing the measurement sensitivity, $\frac{\partial |S_{11}|}{\partial \varepsilon'_{r,\text{mut}}}$. Here $\varepsilon'_{r,\text{mut}}$ denotes the relative dielectric constant of the material to be measured. In the calculations, it is assumed that performing measurements in the region where the value of $|S_{11}|$ is less than 0.1 – 0.2 is not desirable, as for such small values of $|S_{11}|$ the corresponding measurement uncertainty is larger. The large uncertainty results from the very high sensitivity of the model to

the distance between slabs and the accuracy of the slab thickness measurements.

Calculations show that the sensitivity of the measurement model can be increased by using an extended two-slab measurement model involving two slabs, one of which has a known dielectric constant, whereas the dielectric constant of the other MUT slab needs to be determined (measured).

In the thesis, formulas are derived for the calculation of the scattering matrix element S_{11} and its magnitude $|S_{11}|$. Also, the software has been developed for calculating the sensitivity coefficient of the conventional models, $c_{cl} = \frac{\partial |S_{11}|}{\partial \epsilon'_{r,mut}}$, as well as one of the extended models $c_{ex} = \frac{\partial |S_{11}|}{\partial \epsilon'_{r,mut}}$. The software also solves the inverse problem to extract the dielectric constant of the MUT, $\epsilon'_{r,mut}$, from a given value of $|S_{11}|$.

The measurement uncertainty $u(\epsilon'_{r,mut})$, when $u_{|S_{11}|}$ and other input parameter measurement uncertainties are known, can also be calculated using the developed software. Therefore it is capable of finding optimal dimensions of the extended models to achieve higher sensitivity than that of the conventional measurement models.

For constructing and evaluating the extended models, a procedure has been developed and validated. The proposed dielectric constant measurement procedure comprises the following six steps:

1. Insert a MUT sample with the dielectric constant to be found, $\epsilon'_{r,mut}$ into the rectangular waveguide, and measure the magnitude of the scattering matrix element $|S_{11}|$. Then From the measured value of $|S_{11}|$, $\epsilon'_{r,mut}$ is deduced by solving the inverse problem. Note that it is assumed that the MUT losses $\tan \delta_{mut}$ are measured beforehand or are given in the relevant documentation.
2. Use $\epsilon'_{r,mut}$ calculated in the previous step to calculate the sensitivity coefficient of the measurement model $c_{cl} = \frac{\partial |S_{11}|}{\partial \epsilon'_{r,mut}}$ and evaluate the suitability of the conventional measurement model:
 - a if the conventional model can provide sufficiently high measurement accuracy, because the sensitivity of the model is sufficient $c_{cl} > 1$ (but a higher sensitivity can also be requested), then no additional measures need to be taken;
 - b if the sensitivity of the measurement model is low $c_{cl} < 1$, then an extended model is created by adding another dielectric slab with known dimensions and dielectric constant to the MUT slab in the conventional model.
3. Select an auxiliary slab with a known dielectric constant $\epsilon'_{r,aux}$ and the loss tangent (it would be wiser to choose a ready-made product whose parameters are specified by the manufacturer). Find the distance between the MUT slab and the auxiliary slab, d_{int} , as well as the thickness of the additional slab d_{aux} , which provides the highest possible sensitivity of the extended measurement model $c_{ex} = \frac{\partial |S_{11}|}{\partial \epsilon'_{r,mut}}$ in the range of possible values of the measured MUT dielectric constant.

4. If for the chosen auxiliary slab it is not possible to find d_{int} and d_{aux} such that the sensitivity coefficient of the extended model is sufficiently large to reach c_{ex} , then the MUT with another $\epsilon'_{\text{r,aux}}$ should be chosen, and the step 3 of the algorithm should be repeated.
5. To make it possible to utilize manufactured ready-to-use slabs as auxiliary slabs, an auxiliary slab is selected for the extended model whose thickness d_{aux} is closest to that calculated in step 3.
6. c_{ex} of the created model is calculated, and in case it is sufficient, the model construction procedure is terminated.

Since it is not possible to produce an auxiliary slab with dimensions that perfectly match the calculated optimal dimensions, it is assumed that auxiliary slabs with different thickness values that differ by 0.01 mm are utilized, so the calculations in step 3 of the procedure are performed only for these values.

3.2.3 Extended Model Analysis

In this chapter, experimental models composed of two slabs located in a rectangular waveguide are investigated. One of the slabs has an unknown dielectric constant to be determined via measurements, while the other one has a priori known constitutive properties, which can be measured by some more accurate, but at the same time more cumbersome method, such as resonant cavity method. The samples considered in the present study are full-height and full-width rectangular slabs. The main reason models involving rectangular slabs are among the most commonly used in dielectric constant measurements is their simplicity from the point of view of experimenters. Alternately, forming slab-shaped samples of some biological or agricultural substances, such as flour, is often easier.

The geometry of the conventional single slab waveguide measurement model is depicted in Fig. 3.1.

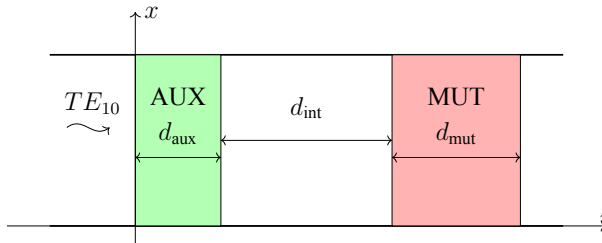


Fig. 3.1. Geometry of the two-slab waveguide measurement model.

It is assumed that the dielectric slabs are homogeneous and the waveguide walls are perfectly conducting. These assumptions significantly simplify the mathematical model of the measurement model - they allow obtaining simple analytical expressions for calculating S_{11} , but do not result in noticeable discrepancies between the results obtained under these assumptions and the actual ones. The measurement uncertainty estimation for the model is performed by means of

the MCM. Probability distributions for the model input quantities are chosen according to the Bayesian Maximum Entropy principle. In the present case, all the model parameters are assumed to follow a normal distribution.

3.2.4 Solution of the Forward Problem

The mathematical formulas derived in this section facilitate the finding of optimal model measurement model parameters that ensure a sufficiently high measurement curve slope and, therefore, lower measurement uncertainty. In this section, only a brief overview of the numerical method for solving the forward scattering problem is presented for the reader's convenience.

The scattering parameters for the auxiliary slab only can be calculated using the following simple closed-form expressions

$$S_{11}^{\text{aux}} = \frac{R_{\text{aux}} (1 - T_{\text{aux}}^2)}{1 - R_{\text{aux}}^2 T_{\text{aux}}^2}, \quad (3.1)$$

$$S_{21}^{\text{aux}} = \frac{T_{\text{aux}} (1 - R_{\text{aux}}^2)}{1 - R_{\text{aux}}^2 T_{\text{aux}}^2}, \quad (3.2)$$

$$S_{12}^{\text{aux}} = \frac{T_{\text{aux}} (1 - R_{\text{aux}}^2)}{1 - R_{\text{aux}}^2 T_{\text{aux}}^2}, \quad (3.3)$$

$$S_{22}^{\text{aux}} = \frac{R_{\text{aux}} (1 - T_{\text{aux}}^2)}{1 - R_{\text{aux}}^2 T_{\text{aux}}^2}, \quad (3.4)$$

where

$R_{\text{aux}} = (\tilde{k}_o - \tilde{k}_{\text{aux}})/(\tilde{k}_o + \tilde{k}_{\text{aux}})$ - the interfacial reflection coefficient for the auxiliary slab faces;

$T_{\text{aux}} = e^{-j\tilde{k}_{\text{aux}}d_{\text{aux}}}$ - the propagation factor of the auxiliary slab;

$\tilde{k}_o = \sqrt{k_o^2 - \pi^2/a^2}$ - the free space waveguide wavenumber, 1/m;

$\tilde{k}_{\text{aux}} = \sqrt{k_o^2 \varepsilon_{r,\text{aux}} - \pi^2/a^2}$ - the waveguide wavenumber in the auxiliary slab, 1/m;

$\varepsilon_{r,\text{aux}} = \varepsilon'_{r,\text{aux}} (1 - j \tan \delta_{\text{aux}})$ - the complex dielectric constant of the auxiliary slab.

These coefficients can be easily derived either by employing the multiple reflection method or by solving the corresponding Helmholtz equation for each slab and homogeneous regions outside them and enforcing continuity of the tangential field components across each interface.

The scattering parameters for the second slab can be derived in a similar manner. For a wave propagating along the z axis, one has

$$S_{11}^{\text{mut}} = \frac{R_{\text{mut}} (1 - T_{\text{mut}}^2)}{1 - R_{\text{mut}}^2 T_{\text{mut}}^2}, \quad (3.5)$$

$$S_{21}^{\text{mut}} = \frac{T_{\text{mut}} (1 - R_{\text{mut}}^2)}{1 - R_{\text{mut}}^2 T_{\text{mut}}^2}, \quad (3.6)$$

$$S_{12}^{\text{mut}} = \frac{T_{\text{mut}} (1 - R_{\text{mut}}^2)}{1 - R_{\text{mut}}^2 T_{\text{mut}}^2}, \quad (3.7)$$

$$S_{22}^{\text{mut}} = \frac{R_{\text{mut}}(1 - T_{\text{mut}}^2)}{1 - R_{\text{mut}}^2 T_{\text{mut}}^2}, \quad (3.8)$$

where

$$\begin{aligned} R_{\text{mut}} &= (\tilde{k}_o - \tilde{k}_{\text{mut}})/(\tilde{k}_o + \tilde{k}_{\text{mut}}) \text{ - the interfacial reflection coefficient for slab faces;} \\ T_{\text{mut}} &= e^{-\tilde{k}_{\text{mut}} d_{\text{mut}}} \text{ - the propagation factor of the MUT slab;} \\ \tilde{k}_{\text{mut}} &= \sqrt{k_o^2 \varepsilon_{r,\text{mut}} - \pi^2/a^2} \text{ - the waveguide wavenumber in the MUT filled region, } 1/m. \\ \varepsilon_{r,\text{mut}} &= \varepsilon'_{r,\text{mut}} (1 - j \tan \delta_{\text{mut}}) \text{ - the complex dielectric constant of the MUT slab.} \end{aligned}$$

The reflection coefficient for a structure consisting of both slabs can be derived by using (3.1)–(3.8) and the multiple reflection method as follows

$$S_{11} = S_{11}^{\text{aux}} + \frac{S_{21}^{\text{aux}} S_{11}^{\text{mut}} S_{12}^{\text{aux}} T_m^2}{1 - S_{22}^{\text{aux}} S_{11}^{\text{mut}} T_m^2}. \quad (3.9)$$

Now, taking the absolute value of (3.9) and applying a number of algebraic manipulations, yields

$$|S_{11}| = \left| \frac{S_{11}^{\text{aux}} - (S_{11}^{\text{aux}} S_{22}^{\text{aux}} - S_{21}^{\text{aux}} S_{12}^{\text{aux}}) S_{11}^{\text{mut}} T_m^2}{1 - S_{22}^{\text{aux}} S_{11}^{\text{mut}} T_m^2} \right|, \quad (3.10)$$

where

$$T_m = e^{-\tilde{k}_o d_{\text{int}}} \text{ - the transmission transmission coefficient for the interslab space.}$$

For the derivation of (3.9), the method of multiple reflections was employed, which will be described in more detail in the next chapter. Since formulas for the waveguide-based slab and the free space-based slab models are very similar, the author decided not to reproduce their derivation twice.

Now, substituting (3.1)–(3.4) into the first factor of the second term of the numerator of (3.10), one has

$$S_{11}^{\text{aux}} S_{22}^{\text{aux}} - S_{21}^{\text{aux}} S_{12}^{\text{aux}} = \frac{S_{11}^{\text{aux}} S_{22}^{\text{aux}} - T_1^2}{1 - S_{11}^{\text{aux}} S_{22}^{\text{aux}} T_1^2}. \quad (3.11)$$

For a lossless auxiliary slab, the absolute value of factor (3.11) is unity, the phase is equal to $\arg(S_{11}^{\text{aux}}) + \arg(S_{22}^{\text{aux}})$ and $|S_{11}^{\text{aux}}| = |S_{22}^{\text{aux}}|$. Thus, (3.10) takes the form

$$|S_{11}| = \left| \frac{|S_{11}^{\text{aux}}| - |S_{11}^{\text{mut}}| P}{1 - |S_{11}^{\text{aux}}| |S_{11}^{\text{mut}}| P} \right|, \quad (3.12)$$

where

$$P = e^{j\varphi_p} = e^{j(\arg(S_{11}^{\text{mut}}) + \arg(S_{22}^{\text{aux}}))} \cdot T_m^2 = e^{j(\arg(S_{11}^{\text{mut}}) + \arg(S_{22}^{\text{aux}}) - 2\tilde{k}_m d_{\text{int}})} \text{ - the phase factor.}$$

As it can be seen, the $|S_{11}|$ depends upon the three real quantities only: $|S_{11}^{\text{aux}}|$, $|S_{11}^{\text{mut}}|$ and φ_p . In [131], it is shown that curve $|S_{11}|(\varepsilon'_{r,\text{mut}})$ attains the highest steepness in the neighborhood of reflection zeros (model resonances) of $|S_{11}|$, however, making measurements in the vicinity of reflection zeros is highly undesirable since the measurement uncertainty of $|S_{11}|$ is large for

small values of $|S_{11}|$. Thus, in practice, it is optimal to make dielectric constant measurements between a reflection zero (minimum) and the maximum, where the slope of the measurement curve is still sufficiently high.

Furthermore, from (3.12) it follows that $|S_{11}|$ reaches zero only when $P = 1$ ($\varphi_p = \pm 2\pi n, n = 0, 1, 2, \dots$) and $|S_{22}^{\text{aux}}| = |S_{11}^{\text{mut}}|$. Since $|S_{11}^{\text{mut}}|$ and $\arg(S_{11}^{\text{mut}})$ are functions of $\epsilon'_{r,\text{mut}}$, whereas $\arg(S_{11}^{\text{aux}})$ does not depend on $\epsilon'_{r,\text{mut}}$ and due to the fact that φ_p is depends linearly on d_{int} , there always exist multiple values of d_{int} , such that $|S_{11}| = 0$, when $|S_{11}^{\text{aux}}| = |S_{11}^{\text{mut}}|$.

In cases when $|S_{11}^{\text{aux}}| \neq |S_{11}^{\text{mut}}|$, the reflection zero can no longer be achieved, but if the difference between these quantities is not large it is possible to find a value of d_{int} giving a measurement curve with a distinct minimum in place of the reflection zero, but the minimum value of $|S_{11}|$ is close to zero. Also, the slope of the measurement curve is still high in the region between the minimum and the closest maximum, and therefore, a high measurement model sensitivity is guaranteed. Moreover, in the low-steepness regions $|S_{11}^{\text{mut}}|$ varies very slowly with $\epsilon'_{r,\text{mut}}$, while φ_p exhibits very rapid variations, which means that the steepness of curve $|S_{11}|$ ($\epsilon'_{r,\text{mut}}$), depends largely on that of φ_p ($\epsilon'_{r,\text{mut}}$).

3.2.5 Numerical Study of The Two-Slab Waveguide Model

To verify whether the proposed two-slab waveguide model allows for achieving a higher measurement sensitivity than the conventional model involving the MUT only with fixed frequency and MUT slab thickness, a numerical analysis was carried out.

The model parameters of the extended model under study are summarized in Table 3.1.

Table 3.1

Two-slab waveguide model parameters

Model Parameter	Symbol	Value	Standard uncertainty value
MUT dielectric constant	$\epsilon'_{r,\text{mut}}$	10.2	-
MUT loss tangent	$\tan \delta_{\text{mut}}$	0.0023	$1.15 \cdot 10^{-4}$
Dielectric constant of the auxiliary slab	$\epsilon'_{r,\text{aux}}$	4.3	0.043
Auxiliary slab loss tangent	$\tan \delta_{\text{aux}}$	0.003	$5.0 \cdot 10^{-5}$
MUT slab thickness	d_{mut}	2.5 mm	0.01 mm
Auxiliary slab thickness	d_{aux}	3.8 mm	0.01 mm
Interslab distance	d_{int}	20 mm	0.01 mm
Frequency	f	10 GHz	35 MHz
Waveguide width	a	22.86 mm	0.01 mm

For the conventional model, the MUT parameters (dielectric constant, loss tangent, and thickness) are the same as in the extended model. In the numerical simulations of the model, it

was assumed that the material under study is the high-frequency ceramic Arlon AD1000 [95], which is widely used in the high-frequency range as the bases of antennas, filters, and other devices. The material has low losses at high frequencies. The data provided in the manufacturer's documentation are as follows: dielectric constant - 10.2 and loss tangent 0.003 at a frequency of 10 GHz. The documentation states that these quantities were measured by the IPC-TM-650 method [10], which is one of the resonance methods. In the description of the method, only the uncertainty in dielectric constant measurements is specified, but it is not specified for the loss tangent, and it is accepted based on the average data of other measurements.

It is assumed that both models are measured using a vector network analyzer (for VNA) P5024B. The analyzer is assumed to be calibrated with calibration standard 85050C (TRL). The calibration method is (Full Two Port Calibrations). The measurement uncertainty after calibration is calculated using a specialized program Keysight VNA Uncertainty Calculator for measuring measurement uncertainty after calibration, and the dependence of $|S_{11}|$ measurement uncertainty on $|S_{11}|$ is shown in Fig. 3.2. As can be seen, the uncertainty increases as $|S_{11}|$ increases.

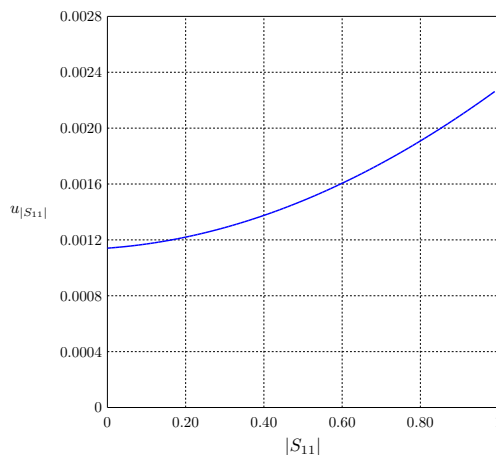


Fig. 3.2. $u_{|S_{11}|}$ as a function of $|S_{11}|$ for vector network analyzer Keysight P5024B.

As far as the material of the auxiliary slab is concerned, it is assumed to be Arlon AD430 [98], with a dielectric constant of 4.3 and a loss tangent equal to 0.003. This material is also widely used in various high-frequency devices due to low losses and high thermal stability. Unlike other high-frequency ceramic materials, it is not so fragile, which simplifies mechanical processing.

Additionally, it is assumed that the thicknesses of the slabs, the width of the broader wall of the waveguide, and the distance between the slabs are measured with the expanded uncertainty of 0.02 mm [97], which corresponds to the standard uncertainty of 0.01 mm. The absolute standard uncertainty associated with the dielectric constant of the auxiliary slab is 0.043, which corresponds to 2% [6] relative expanded measurement uncertainty (the corresponding relative

standard uncertainty is 1%). The absolute standard uncertainty associated with the loss tangent of the auxiliary slab is $5.0 \cdot 10^{-5}$ [6]. It is assumed that the auxiliary slab was characterized beforehand by means of a re-entrant cavity measurement method [6].

Fig. 3.3 shows the calculated $|S_{11}|$ as a function of dielectric constant on $\epsilon'_{r,\text{mut}}$, for the conventional (CSWM) and extended (ETSWM) models. The confidence intervals associated with the $|S_{11}|$ are represented as the horizontal bars in Fig. 3.3. The blue bar corresponds to the confidence interval of the conventional model's $|S_{11}|$, whereas the red one refers to the possible values of the $|S_{11}|$ of the extended model.

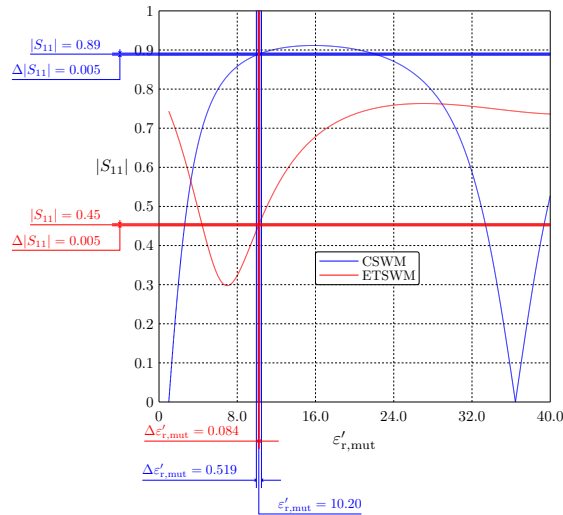


Fig. 3.3. $|S_{11}|$ as a function of $\epsilon'_{r,\text{mut}}$, and widths of confidence intervals for the conventional (CSWM) and the extended (ETSWM) models.

This graph is entirely illustrative, and the width of the coverage intervals does not correspond to the actual for the selected VNA model. Meanwhile, the vertical bars represent the confidence intervals for the measured value of $\epsilon'_{r,\text{mut}}$ that differ from the actual one due to the uncertainty in the measurement of $|S_{11}|$. In this instance, the width of the confidence interval for both models is assumed to be equal to 0.005. The confidence level of the confidence intervals is approximately 68 %, i.e., the confidence interval width is chosen to be one standard deviation of the normal probability distribution.

The obtained results demonstrate that the width of the 68 % confidence interval for $\epsilon'_{r,\text{mut}}$ is approximately 6.2 times smaller, which means that the measurement uncertainty, in this case, is also likely to be smaller. However, in this case, the standard uncertainties associated with $|S_{11}|$ for both models are assumed to be equal, but it is not the case, as the other measurement model parameters also affect the value of $|S_{11}|$ and therefore their uncertainties contribute to $u_{|S_{11}|}$. Alternatively, the resulting uncertainty will be larger since the extended model has more parameters, each contributing to $u_{|S_{11}|}$. That is why Fig. 3.3 may serve only for the evaluation of the measurement model suitability based on its sensitivity. The present model example clearly

shows that the conventional model is not suitable due to very low sensitivity. In case the preliminary evaluation of the model suitability shows that the model sensitivity is not very low and, therefore, it can be employed in the measurements, one needs to perform a more accurate evaluation based on the uncertainty estimation methods.

In Fig. 3.4, the standard dielectric constant measurement uncertainty estimated with the aid of the MCM is displayed.

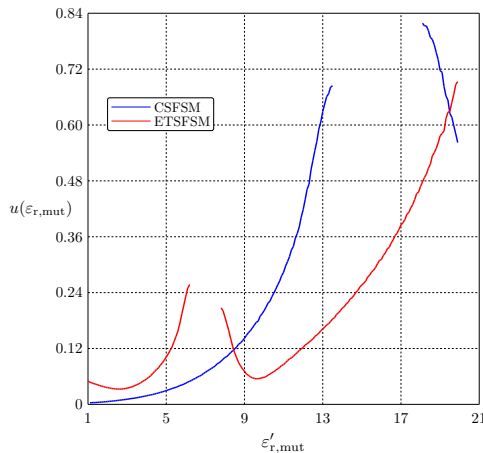


Fig. 3.4. The standard uncertainty as a function of $\epsilon'_{r,mut}$ for the conventional (CSWM) and the extended (ETSWM) models.

The MCM was selected owing to its capability to handle non-linear models more accurately than the EPM, but it is very computationally demanding. For example, to obtain the results presented in Fig. 3.4, the MCM iteration (trial) number was set to 100000. The estimation error does not exceed 2% in the regions of interest, but in the regions where the MCM method fails, the error may be larger. At the end of this chapter, the results of a comparative study carried out to ascertain the amount of discrepancy between the MCM and EPM estimation results are presented.

The missing parts of the curves shown in Fig. 3.4 correspond to the MUT dielectric constant value ranges, where the MCM fails to find an uncertainty estimate. This occurs because more than 10% of the MCM realizations give values of $|S_{11}|$ that are greater than the maximum possible value, which is determined by the definition of this quantity and the VNA capabilities. Such situations arise in the MCM method analysis when the actual dielectric constant is in a low-sensitivity region of the measurement model.

The model is by no means perfect - the main drawback of this model is the fact that the slabs must be precisely positioned in the model, and in situations where the sensitivity of the model is high to even small changes in the distance between slabs, even small changes in the distance between slabs can cause relatively large $|S_{11}|$ changes, which will significantly increase the uncertainty of measurements.

3.3 Three-Slab Waveguide Measurement Model

3.3.1 Shortcomings of Two-slab Measurement Model

Although a relatively simple two-slab model can increase the measurement model sensitivity for a required range of model parameter values, the model has several shortcomings manifested in the practical implementation of the model.

One of the disadvantages of the two-slab model is that it is difficult to ensure the (optimal) distance between the slabs; in practice, it is difficult to place the slabs so that the distance between them is equal to the calculated optimal distance.

Another issue is that slabs with a small thickness are very difficult to place so that their broader faces are perpendicular to the direction of the plane wave propagation. Even a slight displacement can cause a difference between theoretically expected and actual measurement results. This circumstance is less critical if the dielectric constant of relatively thick slabs is measured, but in this case, the effect of the air gap between the slab faces and the waveguide walls on the measurement results must be taken into account - the greater the thickness of the slab, the greater the effect of the air gap on $|S_{11}|$. In practice, the impact of the air gap is reduced by using special pastes with high conductivity.

To mitigate the problems mentioned above, the author proposes to use a three-slab model. In contrast to the two-slab model, in its three-slab counterpart, another dielectric slab is placed between the main slabs (auxiliary slab and MUT slab). The slabs in this model are arranged so that there are no air gaps between them. The main advantage of the three-slab model is the ability to measure the thickness of the middle slab with a high accuracy, which reduces the uncertainty associated with this quantity.

3.3.2 Uncertainty Analysis of the Three Slab Model

Now, investigate a three-slab model shown in Fig. 3.5. The parameters of the three-slab model under consideration are summarized in Table 3.2.

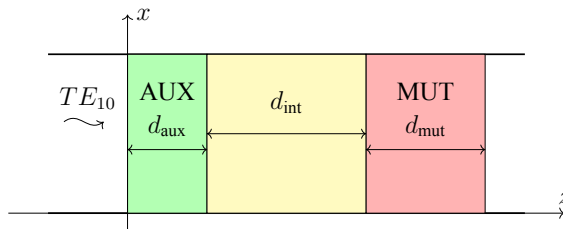


Fig. 3.5. Three-slab waveguide measurement model geometry.

Table 3.2

Three-slab waveguide model parameters

Model Parameter	Symbol	Value	Standard uncertainty value
MUT dielectric constant	$\varepsilon'_{r,\text{mut}}$	10.2	-
MUT loss tangent	$\tan \delta_{\text{mut}}$	0.0023	$1.15 \cdot 10^{-4}$
Dielectric constant of the auxiliary slab	$\varepsilon'_{r,\text{aux}}$	4.3	0.043
Auxiliary slab loss tangent	$\tan \delta_{\text{aux}}$	0.003	$5.0 \cdot 10^{-5}$
Dielectric constant of the middle slab	$\varepsilon'_{r,\text{int}}$	2.2	0.022
Middle slab loss tangent	$\tan \delta_{\text{int}}$	0.0009	$5.0 \cdot 10^{-5}$
MUT slab thickness	d_{mut}	2.5 mm	0.01 mm
Auxiliary slab thickness	d_{aux}	7.0 mm	0.01 mm
Middle slab thickness	d_{int}	7.1 mm	0.01 mm
Frequency	f	10 GHz	35 MHz
Waveguide width	a	22.86 mm	0.01 mm

The expressions for calculating the model's scattering parameters are the same as those derived in the next chapter for the three-slab free space model. The only exception is formulas for the interfacial reflections coefficient that, in the case of the waveguide model, contain waveguide wavenumbers in place of the ordinary ones for free space.

Fig. 3.6 shows $|S_{11}|$ as a function of $\varepsilon'_{r,\text{mut}}$, and the widths of the confidence intervals for the conventional (CSWM) and the extended three-slab model (ETrSWM) models. As can be seen, the extended model gives about 2.6 times smaller confidence interval width.

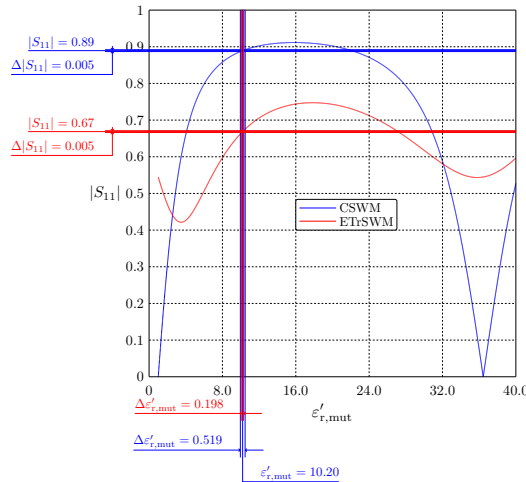


Fig. 3.6. $|S_{11}|$ as a function of $\varepsilon'_{r,\text{mut}}$, and widths of the confidence intervals for the conventional (CSWM) and the extended (CTrSWM) models.

Fig. 3.7 shows the standard dielectric constant measurement uncertainty as a function of the MUT dielectric constant, $\varepsilon'_{r,\text{mut}}$, for the conventional (CSWM) and the extended (ETrSWM) models.

As can be observed, the extended measurement model gives a smaller dielectric constant measurement uncertainty than the conventional one containing the MUT only. Thus, by using the three-slab model, one can also reduce the measurement uncertainty. At the same time, this model is less susceptible to the precise positioning issue described above.

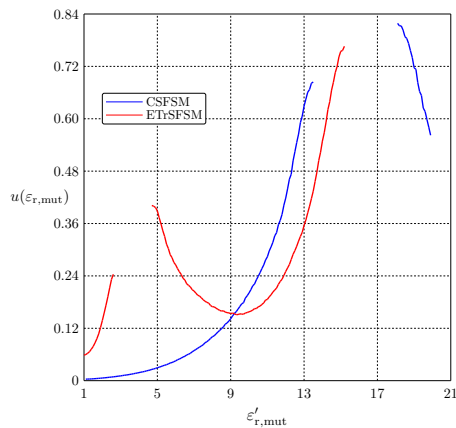


Fig. 3.7. The standard uncertainty as a function of $\varepsilon'_{r,\text{mut}}$ for the conventional (CSWM) and the extended (CTrSWM) models.

3.4 Sensitivity Analysis for Two-Slab Waveguide Model

In order to find the contribution of different model parameters to the total MUT dielectric constant measurement uncertainty using the EPM and also to ascertain the extent to which the estimation results obtained by using the EPM differ from those of the MCM method, the absolute standard uncertainty of the above-mentioned two-slab model is estimated using both the EPM and MCM.

The parameters of the model and their respective uncertainties are the same as for the two-slab model studied in subsection 3.2.5 (see Table 3.1).

The mean value of the MUT dielectric constant obtained by using the MCM method is shown in Fig. 3.8. As it can be seen, the mean value (the best estimate of the measurand) is not equal to its actual value, and, moreover, it depends on the model parameter (in this case the interslab distance). The cause of this discrepancy is the inherent nonlinearity of the measurement model under consideration. Alternatively, for any model with pronounced nonlinearity, the estimate of the actual value will always differ from the true value, regardless of the number of measurements and calibration procedures employed. When all systematic uncertainties are eliminated, the averaging will not reduce the measurement uncertainty when the model is highly non-linear. Therefore, to minimize the measurement uncertainty, one also needs to find a model parameter value or a set of model parameter values that reduce the degree of nonlinearity.

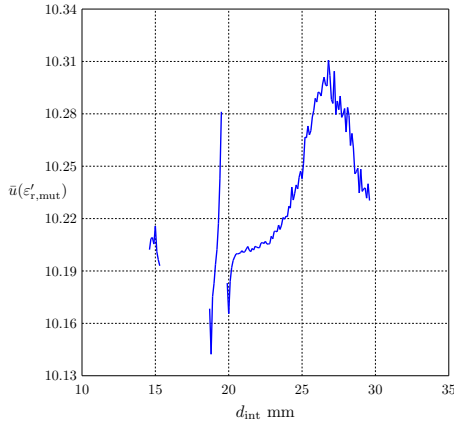


Fig. 3.8. The best estimate (mean value) of $\varepsilon'_{r,\text{mut}}$ as a function of d_{int} .

The estimated standard uncertainty is shown in Fig. 3.9. The figure reveals that there is an optimal value of d_{int} at which the value of the total uncertainty is considerably smaller than at other values.

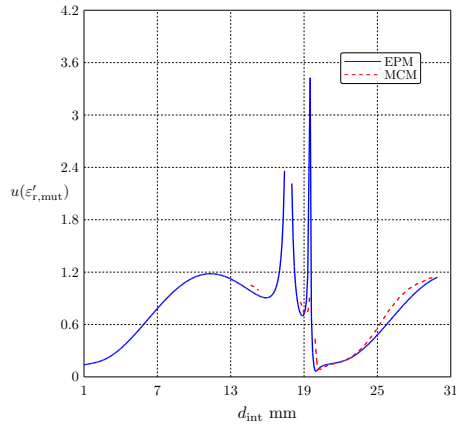


Fig. 3.9. $u(\varepsilon'_{r,\text{mut}})$ as a function of d_{int} .

The narrow maxima seen in Fig. 3.9 correspond to the value of d_{int} at which the measurement model sensitivity coefficient tends to zero, and therefore according to the formula (1.2), the total dielectric constant measurement uncertainty tends to infinity when estimated using the EPM. Regarding the MCM, it fails to converge in the vicinity of these maxima.

Additionally, several uncertainty components (standard uncertainties accounting for the contribution of only one of the model parameters) were computed and plotted as functions of the interslab separation. The sensitivity coefficients were calculated using both the EPM and the MCM to find how large the difference is between the results obtained using these methods. It

should be noted that in contrast to the EPM, the MCM takes into account the nonlinearity of the measurement model, and therefore, there will always be some difference between the results.

Fig. 3.10 shows the uncertainty component due to $|S_{11}|$ as a function of the distance between the MUT and the auxiliary slabs, d_{int} . This uncertainty component characterizes the contribution of the uncertainty associated with $|S_{11}|$ to the total dielectric constant measurement uncertainty. Comparing Fig. 3.9 and Fig. 3.10 reveals that the curves are similar, which means the uncertainty contribution of $|S_{11}|$ dominates in this case.

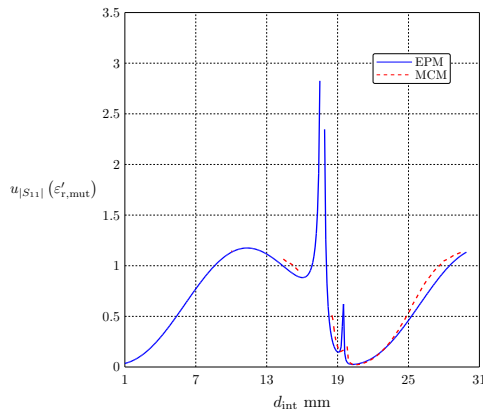


Fig. 3.10. $u_{|S_{11}|}(\epsilon'_{r,\text{mut}})$ as a function of d_{int} .

Fig. 3.11 shows the uncertainty component due to the thickness of the MUT, d_{mut} , as a function of the distance between the MUT and the auxiliary slabs, d_{int} .

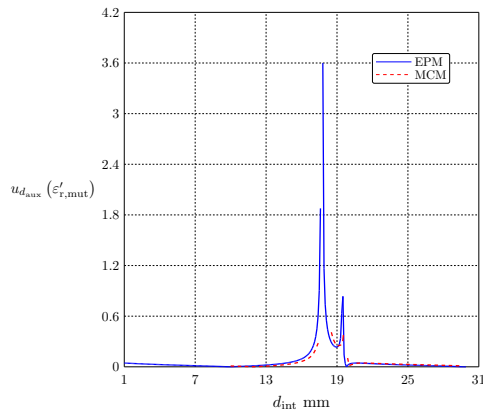


Fig. 3.11. $u_{d_{\text{aux}}}(\epsilon'_{r,\text{mut}})$ as a function of d_{int} .

Fig. 3.12 shows the uncertainty component for the thickness of the auxiliary slab, d_{aux} , as a function of d_{int} . Comparing Fig. 3.11 and Fig. 3.12, it is seen that the uncertainty component

for d_{mut} and d_{aux} are on the same order of magnitude, and therefore their contributions to the total dielectric constant measurement uncertainty are comparable, provided the corresponding measurement uncertainties are the same or comparable.

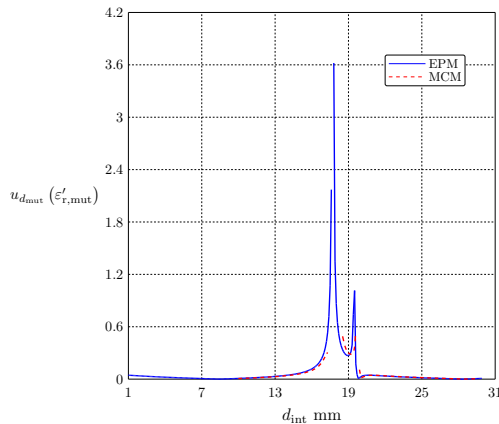


Fig. 3.12. $u_{d_{\text{mut}}}(\epsilon'_{r,\text{mut}})$ as a function of d_{int} .

Also, it is observed that in both cases, there is quite a wide range of the values of d_{int} , where the uncertainty components take small values, namely for $d_{\text{int}} = 8 - 12$. Moreover, in both Fig. 3.11 and Fig. 3.12, there is a noticeable minimum at about $d_{\text{int}} = 21$. This minimum corresponds to the optimal value of d_{int} . However, it is very narrow, which means that the distance between slabs must be ensured with sufficiently high precision. As a result, a slight shift in the position of the slabs may considerably increase the contribution of these two parameter uncertainties to the total one.

Fig. 3.13 shows the uncertainty component for the dielectric constant of the auxiliary slab against d_{int} , while Fig. 3.14 presents the uncertainty component for loss tangent of the auxiliary slab against d_{int} .

As follows from the figures, the contribution of the auxiliary slab loss tangent is considerably smaller than that of the dielectric constant. Also, it is much smaller than the uncertainty component for the other model parameters considered.

Additionally, Fig. 3.13 shows that there are two minima of the uncertainty component as approximately $d_{\text{int}} = 17$ and $d_{\text{int}} = 21$. This means that the contribution of the uncertainty associated with the dielectric constant of the auxiliary slab can be significantly reduced by choosing the auxiliary slab thickness equal to one of these two values. But these minima are very narrow, similar to the case of Fig. 3.11 and Fig. 3.12.

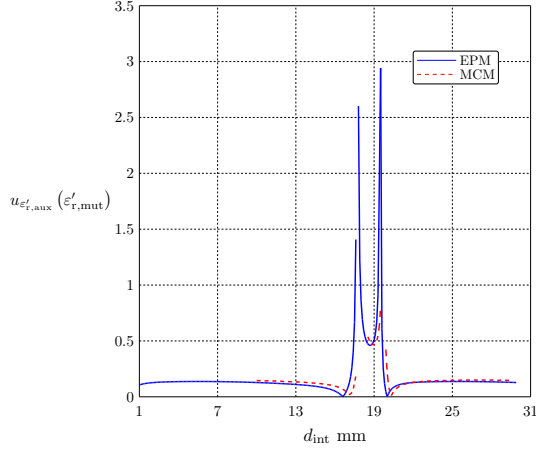


Fig. 3.13. $u_{\epsilon'_{aux}}(\epsilon'_{r,mut})$ as a function of d_{int} .

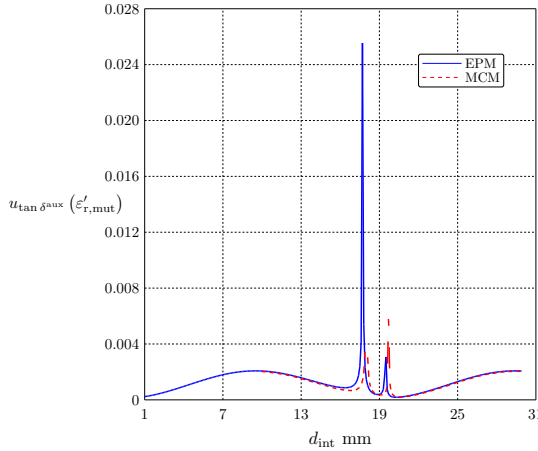


Fig. 3.14. $u_{tan \delta_{aux}}(\epsilon'_{r,mut})$ as a function of d_{int} .

3.5 Summary

Numerical analysis shows that the use of the method of extended models allows for achieving a higher sensitivity of the model even in those intervals of values of dielectric constant, where the conventional measurement model, containing the MUT slab only, exhibits very low sensitivity. The sensitivity of the model is increased by changing the distance between objects d_{int} and the thickness of the auxiliary slab d_{aux} . Additionally, it is shown that despite the presence of the middle slab in the extended three-slab model, it is still possible to achieve a higher measurement model sensitivity in cases where the corresponding conventional model with fixed frequency and the sample dimensions cannot accomplish it.

4. MULTI-SLAB FREE-SPACE MEASUREMENT MODEL

4.1 Two-slab Free Space Measurement Model

4.1.1 Overview of Free Space Measurement Model

This chapter demonstrates that a simple measurement model composed of MUT and two or three dielectric slabs with known constitutive parameters (auxiliary slabs), whose parameters are chosen in an optimal way, allows for a considerable reduction in the total uncertainty [99]. The EMCP of the auxiliary slabs are assumed to be measured by using high-precision equipment in conjunction with more sophisticated measurement techniques. The parameters of the auxiliary slab(s) are chosen so that the resulting sensitivity coefficient of the three-slab model, defined as $\partial|S_{11}|/\partial\varepsilon'_{r,\text{mut}}$, is greater than that of the model containing the MUT only.

The main advantage of the proposed methodology is that it allows for finding optimal parameters of models for which the forward problem cannot be solved in closed form (as in [18]) in a time-efficient way. In addition, the technique is universal and can be successfully applied to a number of similar problems. In order to verify the efficiency of the proposed methodology, the slopes of the measurement curves of both the original model (MUT only) and the extended (two-slab or three-slab) models are compared.

4.1.2 Solution of the Forward Problem

The geometry of the model under consideration is shown in Fig. 4.1. A severe limitation of waveguide measurement models discussed in [131] is a relatively narrow frequency range that can be used for measurements. The lower limit of the range is the cut-off frequency of the dominant waveguide mode, whereas the upper one is the cut-off frequency of the second mode.

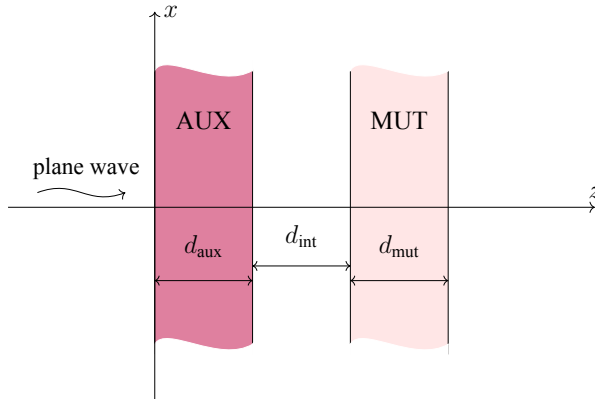


Fig. 4.1. Two-Slab Free Space Measurement Model Geometry.

In contrast to the waveguide measurement technique, the free space technique does not suffer from such a limitation. However, the method considered herein also has a limitation: the

analytical solution can be found only for slabs with infinite width and length. In contrast, only finite-dimensional slabs are available in real-world measurements, resulting in discrepancies between the calculated and measured data due to the diffraction at slab edges. For convenience, in this section, the model scattering parameter expressions are derived for a general case of three slab structures (three-slab model). The two-slab model can be viewed as a special case of the three-slab model when $\varepsilon_{r,int} = 1$.

First, derive the expression for the S_{11} under normal plane wave incidence (it is assumed that the wave propagates along the z -axis). The parameters of the measurement model being considered are as follows: d_{aux} , d_{mut} which are the thicknesses of the auxiliary and the MUT slabs, respectively, d_{int} - the thickness of the middle slab, f is the measurement frequency. Since the reflection coefficients are associated with reference planes, they must be chosen first.

For each slab, it is convenient to choose the reference planes so that they are aligned with the faces of the slab. In the multiple reflection method, the reflected wave can be found by adding all the waves (reflected waves of different order) resulting from multiple reflections of the incident plane wave from the faces of the slab and splitting. The wave splitting into two components occurs upon the wave arrival at the face of the slab.

To simplify the derivation of the expressions for the scattering matrix elements and to make formulas more compact, the entire structure is treated as being composed of five homogeneous dielectric-filled (or air-filled) regions, and the notation used in [99] is adopted. This notation is convenient as it can be applied to both the two-slab model, its three-slab counterpart, and even more general models. Each of the regions is assigned a number as follows: 0 refers to the semi-infinite region to the left of the auxiliary slab, 1 refers to the space occupied by the auxiliary slab, 3 refers to the space occupied by the MUT slab, 2 refers to the space occupied by the middle slab (three-slab model) or air-filled region between the slabs (two-slab model), and 4 refers to the semi-infinite region to the right of the MUT slab.

Similar to the homogeneous regions themselves, the quantities associated with them can also be denoted in a similar manner. For example, for the two-slab model shown in (Fig. 4.1), the thicknesses are denoted as follows: $d_1 = d_{aux}$, $d_2 = d_{int}$, $d_3 = d_{mut}$. The same applies to the respective dielectric constants and loss tangents.

For the wave impinging upon the interface between i -th and j -th regions from the i -th region, the interfacial reflection and transmission coefficients are, respectively, given by

$$\Gamma_{ij} = \frac{\sqrt{\varepsilon_{ri}} - \sqrt{\varepsilon_{rj}}}{\sqrt{\varepsilon_{ri}} + \sqrt{\varepsilon_{rj}}} \quad t_{ij} = \frac{2\sqrt{\varepsilon_{ri}}}{\sqrt{\varepsilon_{ri}} + \sqrt{\varepsilon_{rj}}}, \quad (4.1)$$

where

$\varepsilon_{ri} = \varepsilon'_{ri} (1 - j \tan \delta_i^e)$ - the complex permittivity of the i -th region;

ε'_{ri} - the real part of ε_{ri} ;

$\tan \delta_i^e$ - the dielectric loss tangent of the i -th region.

In addition, they satisfy the following relations

$$\Gamma_{ij} = -\Gamma_{ji} \quad 1 + \Gamma_{ij} = t_{ij}. \quad (4.2)$$

The first-order reflected wave is the result of the reflection of the incident plane wave at the front face of the slab, whereas that of the second-order results from reflection at the rear face of the face. The difference between the 2-nd and n -th reflected wave is that the latter undergoes n more reflections from both the faces of the slab before leaving it, which is equivalent to the multiplication of the intensity of the 2-nd order reflected wave by the factor $(\Gamma_{10}\Gamma_{12}T_1^2)^n$, where $T_i = e^{-j\sqrt{\epsilon_{ri}}k_0d_i}$, $i = 1, 2, 3$. is the phase factor of the i -th region and d_i is the thickness of the i -th region.

Now by adding all the reflected waves, one obtains the total reflected wave, which under the assumption that the intensity of the incident wave is unity, is equal to the reflection coefficient for the first slab only (reflection from other slabs is not considered at this point)

$$\begin{aligned} S_{11}^{\text{aux}} &= \Gamma_{01} + t_{01} t_{10} \Gamma_{12} T_1^2 \lim_{N \rightarrow \infty} \sum_{n=0}^N (\Gamma_{10}\Gamma_{12}T_1^2)^n \\ &= \Gamma_{01} + t_{01} t_{10} \Gamma_{12} T_1^2 \lim_{N \rightarrow \infty} \frac{1 - (\Gamma_{10}\Gamma_{12}T_1^2)^N}{1 - \Gamma_{10}\Gamma_{12}T_1^2}. \end{aligned} \quad (4.3)$$

As the factor $(\Gamma_{10}\Gamma_{12}T_1^2)^N$ tends to zero as $N \rightarrow \infty$, (4.3) takes the form

$$S_{11}^{\text{aux}} = \Gamma_{01} + \frac{t_{01} t_{10} \Gamma_{12} T_1^2}{1 - \Gamma_{10}\Gamma_{12}T_1^2}. \quad (4.4)$$

In view of relations (4.2), one has

$$\begin{aligned} S_{11}^{\text{aux}} &= \Gamma_{01} - \frac{(1 + \Gamma_{01})(1 - \Gamma_{01})\Gamma_{21} T_1^2}{1 - \Gamma_{01}\Gamma_{21}T_1^2} \\ &= \frac{\Gamma_{01} - \Gamma_{01}^2\Gamma_{21}T_1^2 - (1 - \Gamma_{01}^2)\Gamma_{21} T_1^2}{1 - \Gamma_{01}\Gamma_{21}T_1^2} = \frac{\Gamma_{01} - \Gamma_{21} T_1^2}{1 - \Gamma_{01}\Gamma_{21}T_1^2}. \end{aligned} \quad (4.5)$$

Now, derive the transmission coefficient for the plane wave propagating along the z -axis

$$S_{21}^{\text{aux}} = t_{01} t_{12} T_1 \lim_{N \rightarrow \infty} \sum_{n=0}^N (\Gamma_{10}\Gamma_{12}T_1^2)^n = \frac{t_{01} t_{12} T_1}{1 - \Gamma_{10}\Gamma_{12}T_1^2} = \frac{(1 + \Gamma_{01})(1 - \Gamma_{21}) T_1}{1 - \Gamma_{01}\Gamma_{21}T_1^2}. \quad (4.6)$$

Following the same steps as above, one can obtain the scattering parameter expressions for the plane wave propagating in the opposite direction

$$S_{22}^{\text{aux}} = \frac{\Gamma_{21} - \Gamma_{01} T_1^2}{1 - \Gamma_{01}\Gamma_{21}T_1^2}, \quad (4.7)$$

$$S_{12}^{\text{aux}} = \frac{(1 - \Gamma_{01})(1 + \Gamma_{21})T_1}{1 - \Gamma_{01}\Gamma_{21}T_1^2}. \quad (4.8)$$

The scattering parameters for the MUT slab can be derived in a similar fashion

$$S_{11}^{\text{mut}} = \frac{\Gamma_{23} - \Gamma_{43}T_3^2}{1 - \Gamma_{23}\Gamma_{43}T_3^2}, \quad (4.9)$$

$$S_{21}^{\text{mut}} = \frac{(1 + \Gamma_{23})(1 - \Gamma_{43})T_3}{1 - \Gamma_{23}\Gamma_{43}T_3^2}, \quad (4.10)$$

$$S_{21}^{\text{mut}} = \frac{\Gamma_{43} - \Gamma_{23}T_3^2}{1 - \Gamma_{23}\Gamma_{43}T_3^2}, \quad (4.11)$$

$$S_{12}^{\text{mut}} = \frac{(1 - \Gamma_{23})(1 + \Gamma_{43})T_3}{1 - \Gamma_{23}\Gamma_{43}T_3^2}. \quad (4.12)$$

Once the scattering parameters for the auxiliary and the MUT slabs are found, the S_{11} for the entire measurement model, comprising three slabs, can be derived straightforwardly by using (4.5)-(4.12), as well as the method of multiple reflections

$$S_{11} = S_{11}^{\text{aux}} + S_{21}^{\text{aux}} S_{12}^{\text{aux}} S_{11}^{\text{mut}} T_2^2 \lim_{N \rightarrow \infty} \sum_{n=0}^N (S_{22}^{\text{aux}} S_{11}^{\text{mut}} T_2^2)^n = S_{11}^{\text{aux}} + \frac{S_{21}^{\text{aux}} S_{12}^{\text{aux}} S_{11}^{\text{mut}} T_2^2}{1 - S_{22}^{\text{aux}} S_{11}^{\text{mut}} T_2^2}. \quad (4.13)$$

Now taking the absolute value of (4.13), yields

$$|S_{11}| = \left| \frac{S_{11}^{\text{aux}} - (S_{11}^{\text{aux}} S_{22}^{\text{aux}} - S_{21}^{\text{aux}} S_{12}^{\text{aux}}) S_{11}^{\text{mut}} T_2^2}{1 - S_{22}^{\text{aux}} S_{11}^{\text{mut}} T_2^2} \right|. \quad (4.14)$$

Substituting (4.1) into the first factor of the second term of the numerator of (4.14), one has

$$S_{11}^{\text{aux}} S_{22}^{\text{aux}} - S_{21}^{\text{aux}} S_{12}^{\text{aux}} = \frac{\Gamma_{01}\Gamma_{21} - T_1^2}{1 - \Gamma_{01}\Gamma_{21}T_1^2}. \quad (4.15)$$

Now it can be proved that in the case where the first two slabs are lossless, the absolute value of (4.15) is unity

$$\left| \frac{\Gamma_{01}\Gamma_{21} - T_1^2}{1 - \Gamma_{01}\Gamma_{21}T_1^2} \right| = \left| T_1^2 \frac{1 - \Gamma_{01}\Gamma_{21}T_1^{-2}}{1 - \Gamma_{01}\Gamma_{21}T_1^2} \right| = |T_1^2| \frac{|(1 - \Gamma_{01}\Gamma_{21}T_1^2)^*|}{|1 - \Gamma_{01}\Gamma_{21}T_1^2|} = 1, \quad (4.16)$$

Similarly, it can be shown that $|R_1^+| = |R_1^-|$

$$|S_{22}^{\text{aux}}| = |T_1^2| \frac{|\Gamma_{01} - \Gamma_{21}T_1^{-2}|}{|1 - \Gamma_{01}\Gamma_{21}T_1^2|} = \frac{|(\Gamma_{01} - \Gamma_{21}T_1^2)^*|}{|1 - \Gamma_{01}\Gamma_{21}T_1^2|} = \frac{|\Gamma_{01} - \Gamma_{21}T_1^2|}{|1 - \Gamma_{01}\Gamma_{21}T_1^2|} = |S_{11}^{\text{aux}}|. \quad (4.17)$$

Now making use of (4.17), it can be easily proved that the angle of factor (4.15) is equal to $\arg(S_{11}^{\text{aux}}) + \arg(S_{22}^{\text{aux}})$.

$$\begin{aligned}
\arg(S_{11}^{\text{aux}}) + \arg(S_{22}^{\text{aux}}) &= \arg\left(\frac{S_{11}^{\text{aux}}}{S_{22}^{\text{aux}*}}\right) \\
&= \arg\left(\frac{\Gamma_{01} - \Gamma_{21} T_1^2}{1 - \Gamma_{01}\Gamma_{21} T_1^2} \cdot \frac{T_1^2 - \Gamma_{01}\Gamma_{21}}{\Gamma_{21} T_1^2 - \Gamma_{01}}\right) = \arg\left(\frac{\Gamma_{01}\Gamma_{21} - T_1^2}{1 - \Gamma_{01}\Gamma_{21} T_1^2}\right).
\end{aligned} \tag{4.18}$$

Then using (4.16)-(18), (4.14) becomes

$$|S_{11}| = \left| \frac{|S_{11}^{\text{aux}}| - |S_{11}^{\text{mut}}| P}{1 - |S_{11}^{\text{aux}}| |S_{11}^{\text{mut}}| P} \right|, \tag{4.19}$$

where

$$P = e^{j\varphi_p} = e^{j(\arg(S_{22}^{\text{aux}}) + \arg(S_{11}^{\text{mut}}))}. T_2^2 = e^{j(\arg(S_{22}^{\text{aux}}) + \arg(S_{11}^{\text{mut}}) - 2k_0 \sqrt{\varepsilon_{r,\text{int}}} d_{\text{int}})} - \text{the phase factor.}$$

From (4.19) it follows that $|S_{11}|$ can be treated as a function of the three real quantities: $|S_{11}^{\text{aux}}|$, $|S_{11}^{\text{mut}}|$ and φ_p . As it was shown in [131], the curve $|S_{11}|(\varepsilon'_{r,\text{mut}})$ has the highest slope in the neighborhood of minima (resonances) or zeros of $|S_{11}|(\varepsilon'_{r,\text{mut}})$.

Additionally, from (4.19) it follows that when the condition $|S_{11}^{\text{aux}}| = |S_{11}^{\text{mut}}|$ is satisfied, i.e., when the absolute values of the reflection coefficients for both slabs are equal, it is always possible to achieve $P = 1$ (zeros of $|S_{11}|(\varepsilon'_{r,\text{mut}})$) by varying only $d_2 = d_{\text{int}}$, where d_{int} is the distance between the MUT slab and the auxiliary slab in the case of a two-slab free space model. In the case of the three-slab model, this represents the thickness of the middle slab. $|S_{11}^{\text{mut}}|$ depends on both $\varepsilon'_3 = \varepsilon'_{r,\text{mut}}$ and $d_3 = d_{\text{mut}}$. Note that d_{mut} cannot change in the case of non-destructive measurements, and therefore, for the condition $|S_{11}^{\text{aux}}| = |S_{11}^{\text{mut}}|$ to be satisfied $|S_{11}^{\text{aux}}|$ should be changed by varying d_{aux} .

To increase the slope of $|S_{11}|(\varepsilon'_{r,\text{mut}})$ (high sensitivity), it is not necessarily for the model to be resonant, i.e., for the condition $|S_{11}^{\text{aux}}| = |S_{11}^{\text{mut}}|$ to be strictly satisfied. When $|S_{11}^{\text{aux}}| \neq |S_{11}^{\text{mut}}|$, but their values differ slightly, the curve has minima (not zero in this case) in a low-sensitivity region of the original model. In the vicinity of these minima, the slope is lower than in the case of the resonant model, but it is still sufficiently high to improve the measurement accuracy.

Now, check whether it is always possible to find d_{int} , such that $|S_{11}^{\text{aux}}| = |S_{11}^{\text{mut}}|$. The low-sensitivity regions of the original model are always the neighborhoods of maxima. In such regions, $|S_{11}|$ attains large values that differ only slightly from the maximum and vary very slowly with $\varepsilon'_{r,\text{mut}}$.

From (4.4) it follows that when $\tan \delta_{\text{aux}}^e = 0$, S_{11}^{aux} takes the maximum value only when $T_1^2 = -1$. Since by varying d_{aux} one can always achieve $T_1^2 = -1$, substituting $T_1^2 = -1$ into (4.4), one obtains the maximum value of $|S_{11}^{\text{aux}}|$ that is possible to achieve by varying d_{aux} with a fixed $\varepsilon'_{r,\text{aux}}$

$$|S_{11}^{\text{aux}}|_{\text{max}} = \left| \frac{\Gamma_{01} + \Gamma_{21}}{1 + \Gamma_{01}\Gamma_{21}} \right| = \left| \frac{\sqrt{\varepsilon'_{r,\text{int}}} - \sqrt{\varepsilon'_{r,\text{aux}}}}{\sqrt{\varepsilon'_{r,\text{int}}} + \sqrt{\varepsilon'_{r,\text{aux}}}} \right|. \tag{4.20}$$

From (4.20), it follows that $|S_{11}^{\text{aux}}|_{\text{max}}$ increases with $\varepsilon'_{r,\text{aux}}$; therefore, to increase the slope of models containing MUT with high $\varepsilon'_{r,\text{mut}}$, one has to employ auxiliary slabs with comparable or greater dielectric constant than that of MUT. On the other hand, the rate at which the value of $|S_{11}^{\text{aux}}|$ varies with d_{aux} for slabs with large $\varepsilon'_{r,\text{aux}}$ is higher, except for low-slope regions around each maximum of $|S_{11}^{\text{aux}}|$. In simple terms, the greater the value of $\varepsilon'_{r,\text{aux}}$, the worse, since the component of uncertainty associated with d_{aux} is proportional to the slope of curve $|S_{11}^{\text{aux}}|(d_{\text{aux}})$. This issue can be mitigated by introducing a lossy middle slab into the model. However, in this case, formula (4.19) cannot be used, as the absolute value of factor (4.15) is no longer equal to unity, and the argument of (4.15) becomes different from $\arg S_{11}^{\text{aux}} + \arg S_{22}^{\text{aux}}$. However, in one of author's papers [131] it is demonstrated that for middle slabs with low $\varepsilon'_{r,\text{int}}$ and $\tan \delta_{\text{int}}^{\varepsilon}$ the absolute value of $S_{11}^{\text{aux}} S_{22}^{\text{aux}} - S_{21}^{\text{aux}} S_{12}^{\text{aux}}$ differs only slightly from unity. At the same time, due to losses T_2 decreases exponentially with d_{int} .

Thus, the absolute value of the second term in the numerator of (4.14), namely,

$$(S_{11}^{\text{aux}} S_{22}^{\text{aux}} - S_{21}^{\text{aux}} S_{12}^{\text{aux}}) S_{11}^{\text{mut}} T_2^2 \quad (4.21)$$

can be reduced by using larger resonant values of d_{int} that makes it possible to achieve a reflection zero and, therefore, high sensitivity in models consisting of an optimizing slab with low $\varepsilon'_{r,\text{aux}}$ and MUT with high $\varepsilon'_{r,\text{mut}}$.

Due to the fact that $\arg (S_{11}^{\text{aux}} S_{22}^{\text{aux}} - S_{21}^{\text{aux}} S_{12}^{\text{aux}}) S_{11}^{\text{mut}} T_2^2$ still depends linearly on φ_p , one can find d_{int} , such that $\arg (S_{11}^{\text{aux}} S_{22}^{\text{aux}} - S_{21}^{\text{aux}} S_{12}^{\text{aux}}) S_{11}^{\text{mut}} T_2^2 = \arg (S_{11}^{\text{aux}})$ which implies that $|S_{11}| = 0$ when the condition $|(S_{11}^{\text{aux}} S_{22}^{\text{aux}} - S_{21}^{\text{aux}} S_{12}^{\text{aux}}) S_{11}^{\text{mut}} T_2^2| = |S_{11}^{\text{aux}}|$ is also satisfied.

Another interesting case is a model with a MUT having medium losses, as in this case, it is still possible to achieve resonances. However, the maximum possible slope of the measurement curve in such models is less than that of their lossless counterparts. Furthermore, the higher the losses, the smaller the maximum attainable slope for the model.

The reason the models with a lossy MUT exhibit low measurement model sensitivity to variations in $\varepsilon'_{r,\text{mut}}$ is the fact that φ_p varies slowly with $\varepsilon'_{r,\text{mut}}$ compared to the case of lossless MUT. Alternatively, the larger the loss tangent of material, the lower the slope of $\varphi_p(\varepsilon'_{r,\text{mut}})$ that together with the slope of $|S_{11}|(\varphi_p)$ determines that of $|S_{11}|(\varepsilon'_{r,\text{mut}})$.

4.1.3 Uncertainty Analysis of Free Space Models

A numerical analysis was carried out to verify whether the proposed two-slab model (see Fig. 4.1) can ensure higher measurement sensitivity than that of the conventional model involving the MUT only with fixed frequency and MUT slab thickness. The model parameters of this extended model are summarized in Table 4.1. It is assumed that the MUT parameters for the extended model (dielectric constant, loss tangent, and thickness) are identical to those for the conventional one.

As before, it is assumed that the measurements are performed with a calibrated (two-port calibration method) VNA P5024B. For this measuring device, the uncertainty of the reflection coefficient is around 0.003. In the calculation example, a high-frequency ceramic with an ex-

pected relative dielectric constant equal to 30 and a loss tangent equal to 0.000067 [96] was as the MUT, while the material Arlon AD1000 [95] was selected for the auxiliary slab.

Table 4.1

Two-slab free space model parameters

Model Parameter	Symbol	Value	Standard uncertainty value
MUT dielectric constant	$\epsilon'_{r,\text{mut}}$	30	-
MUT loss tangent	$\tan \delta_{\text{mut}}$	$6.67 \cdot 10^{-5}$	$3.33 \cdot 10^{-6}$
Dielectric constant of the auxiliary slab	$\epsilon'_{r,\text{aux}}$	10.2	0.0102
Auxiliary slab loss tangent	$\tan \delta_{\text{aux}}$	0.0023	$5.0 \cdot 10^{-5}$
MUT slab thickness	d_{mut}	2.0 mm	0.01 mm
Auxiliary slab thickness	d_{aux}	2.6 mm	0.01 mm
Interslab distance	d_{int}	13.1 mm	0.01 mm
Frequency	f	10 GHz	35 MHz

The absolute standard uncertainty associated with the dielectric constant of the auxiliary slab is 0.0102, which corresponds to 2% [6] relative expanded measurement uncertainty. The absolute standard uncertainty associated with the loss tangent of the auxiliary slab is $5.0 \cdot 10^{-5}$ [6]. It is assumed that the auxiliary slab was characterized by means of a re-entrant cavity measurement method.

The calculated $|S_{11}|$ as a function of $\epsilon'_{r,\text{mut}}$ for both the conventional model containing the MUT only and the extended model formed from it by adding one more slab is shown in Fig. 4.2.

Similar to the previous model, in this case, the dimensions of the MUT and the measurement frequency are such that the sensitivity of the conventional model is pretty low, which means that this model is not suitable for dielectric constant measurements as it would give a large measurement uncertainty. As can be seen, the presence of the auxiliary slab affects the slope of the measurement curve; namely, it is significantly higher than in the case of the conventional model.

The horizontal bars in Fig. 4.2 represent the confidence intervals associated with the $|S_{11}|$. The blue bar corresponds to the confidence interval of the $|S_{11}|$ of the conventional model, whereas the red one refers to the possible values of the $|S_{11}|$ of the extended model. The confidence interval width for both models is assumed to be equal to 0.005. The confidence level of confidence intervals is 68%. The results show that the width of the confidence interval for $\epsilon'_{r,\text{mut}}$ is approximately 5.8 times smaller; thus, the extended model is more suitable for measurements than the conventional one. The results clearly indicate that the conventional model is unsuitable due to very low sensitivity.

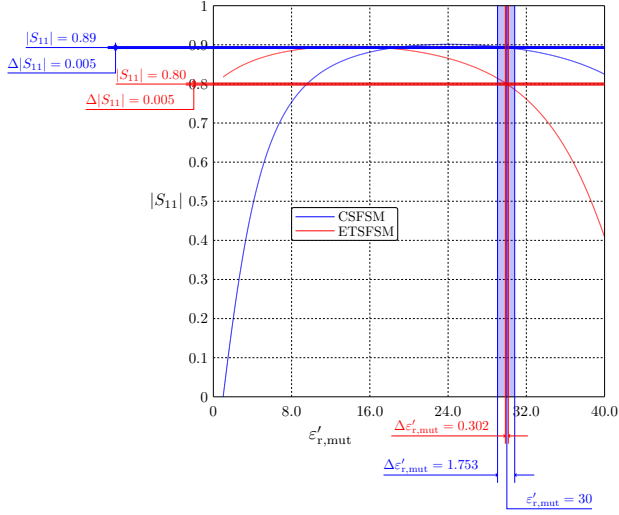


Fig. 4.2. $|S_{11}|$ as a function of $\varepsilon'_{r,\text{mut}}$, and confidence interval widths for the conventional (CSFSM) and the extended (ETSFSM) models.

In Fig. 4.3, the standard dielectric constant measurement uncertainty estimated with the aid of the MCM is displayed. The MCM method was used with 100000 iterations (trials) to obtain the results presented in Fig. 4.3. The estimation error does not exceed 2% in the regions of interest.

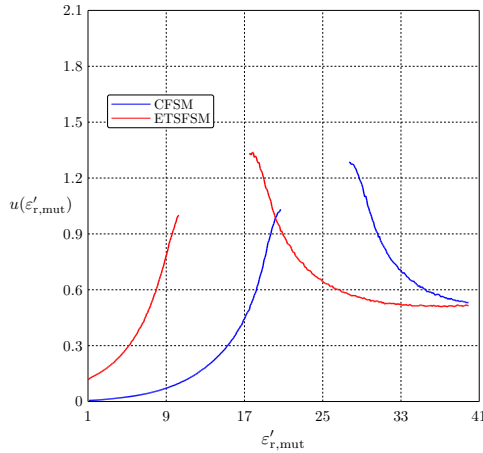


Fig. 4.3. The standard uncertainty as a function of the interslab distance for the conventional (CSFSM) and the extended (ETSFSM) models.

4.2 Three Slab Free Space Measurement Model

Similar to the two-slab-based free space measurement model, the waveguide-based two-slab model also exhibits a considerable sensitivity of the measured quantity $|S_{11}|$ to small changes in

the interslab distance. However, because the sample size, in this case, is sufficiently large, this problem can be mitigated by using specially made sample holders that ensure precise positioning of the slabs. This issue can be addressed by a three-slab model, similar to the one examined and described in the previous chapter of the thesis, in which, unlike the two-slab model, there is another dielectric slab between the main slabs (auxiliary and MUT). The geometry of the three-slab model under consideration is shown Fig. 4.4, and the parameters as summarized in Table 4.2.

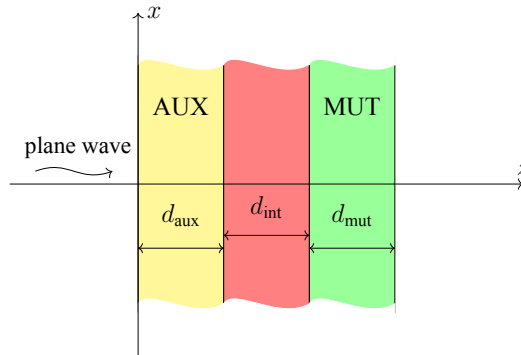


Fig. 4.4. Three-slab free space measurement model geometry.

Table 4.2

Three-slab free space model parameters

Model Parameter	Symbol	Value	Standard uncertainty value
MUT dielectric constant	$\epsilon'_{r,mut}$	30	-
MUT loss tangent	$\tan \delta_{mut}$	$6.67 \cdot 10^{-5}$	$3.33 \cdot 10^{-6}$
Dielectric constant of the auxiliary slab	$\epsilon'_{r,aux}$	10.2	0.0102
Auxiliary slab loss tangent	$\tan \delta_{aux}$	0.0023	$5 \cdot 10^{-5}$
Dielectric constant of the middle slab	$\epsilon'_{r,int}$	2.2	0.022
Middle slab loss tangent	$\tan \delta_{int}$	0.0009	$5 \cdot 10^{-5}$
MUT slab thickness	d_{mut}	2.4 mm	0.01 mm
Auxiliary slab thickness	d_{aux}	5.7 mm	0.01 mm
Middle slab thickness	d_{int}	9.6 mm	0.01 mm
Frequency	f	10 GHz	35 MHz

Fig. 4.5 shows $|S_{11}(\epsilon'_{r,mut})|$ as a function of $\epsilon'_{r,mut}$ and the corresponding measurement uncertainties for the conventional and extended three-slab models. From the figure, it is evident that the sensitivity of the expanded model (its calculated parameters are presented in Table 2.4) is ap-

preciably higher, which results in a considerable reduction in the uncertainty of MUT dielectric constant measurements, $u(\varepsilon'_{r,\text{mut}})$, which in this case is approximately 3.5 times.

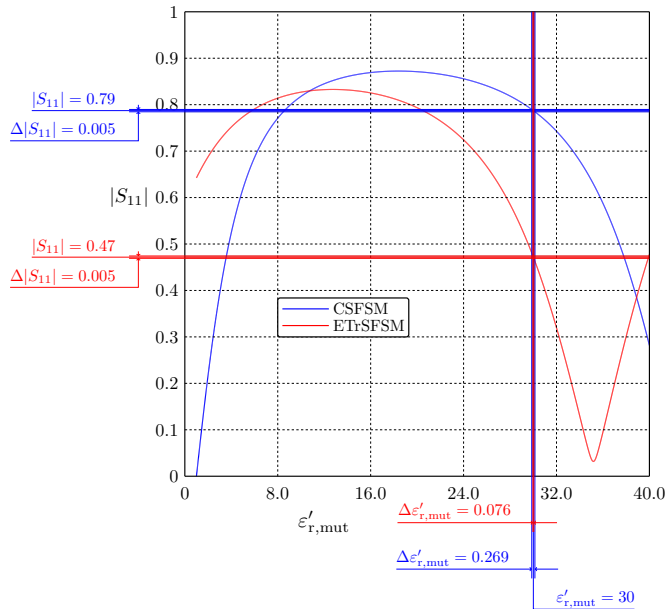


Fig. 4.5. $|S_{11}|$ as a function of $\varepsilon'_{r,\text{mut}}$, and the confidence interval widths for the conventional (CSFSM) and the extended (ETrSFSM) models.

It is worth noting that the increase in sensitivity of the extended models and the corresponding reduction in their measurement uncertainty compared to the conventional model becomes smaller as $\varepsilon'_{r,\text{mut}}$ increases, which in this example is 30.0 and for measurements when measuring MUT with a lower dielectric constant value, the benefits of three-slab models are significantly greater compared to conventional models, and the advantage of using extended models is undeniable.

Fig. 4.6 indicates the measurement uncertainty, $u(\varepsilon'_{r,\text{mut}})$, as a function of $\varepsilon'_{r,\text{mut}}$ for the conventional and extended three-slab model. However, the obtained results show that in constant to its two-slab counterpart, the three-slab model fails to provide better measurement uncertainty, even though its model sensitivity is considerably higher. The cause of such a behavior of the three-slab model is the fact that the MUT dielectric constant in the present example is relatively large. Specifically, for large values of the dielectric constant the contribution of the MUT slab thickness uncertainty cannot be sufficiently reduced by increasing the measurement model sensitivity only since a higher rate of change of $|S_{11}|$ with $\varepsilon'_{r,\text{mut}}$ overwhelms the reduction in the uncertainty component due to d_{mut} resulting from an increase in $\frac{\partial |S_{11}|}{\partial \varepsilon'_{r,\text{mut}}}$. Furthermore, additional numerical studies, whose results are not presented in this thesis, show that for smaller dielectric constant values, such as 10.2, the three-slab model may ensure smaller dielectric constant measurement uncertainty than the conventional model.

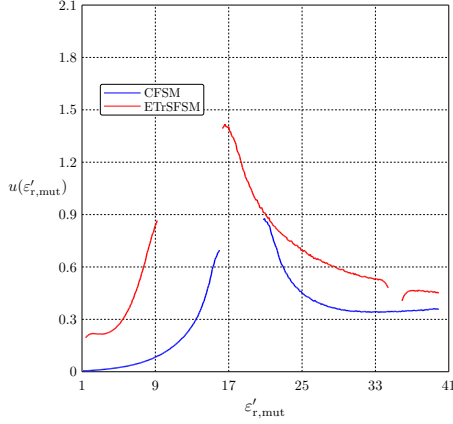


Fig. 4.6. The standard uncertainty as a function of the interslab distance for the conventional (CFM) and the extended (ETrFSM) models.

4.3 Sensitivity Analysis of Two-Slab Free Space Model

Again in order to find the contribution of different model parameters to the total MUT dielectric constant measurement uncertainty using the EPM and compare the EPM and MCM uncertainty estimation results, which is very important for the present study since the model sensitivity concept proposed and treated in the thesis relies on the EPM, the standard uncertainty and several uncertainty components are calculated at different values of d_{int} . The mean value of the MUT dielectric constant obtained by using the MCM method is shown in Fig. 4.7.

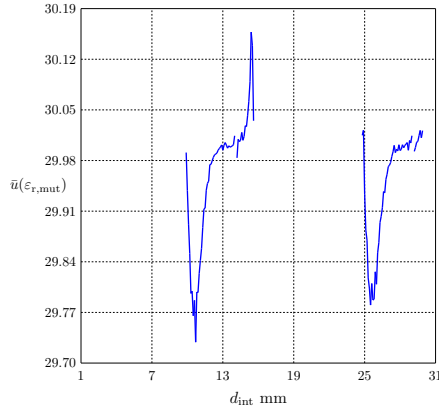


Fig. 4.7. The best estimate of $\varepsilon'_{r,\text{mult}}$ as a function of d_{int} .

The parameters of the model and their respective uncertainties are the same as for the two-slab model studied in subsection 4.1.3 (see Table 4.1).

Similar to the two-slab waveguide model, in the present case, the mean value (the best estimate of the measurand) differs from the actual value and varies with the distance between the

slabs. Of course, it also varies with other model parameters, but the objective was to show the dependence on d_{int} as this quantity plays a crucial role in the model under consideration - it serves as an optimization parameter. The source of the difference is the inherent non-linearity of the measurement model under consideration.

The estimated standard uncertainty is shown in Fig. 4.8, while Fig. 4.9 shows the uncertainty component due to $|S_{11}|$ as a function of the distance between the MUT and the auxiliary slabs, d_{int} .

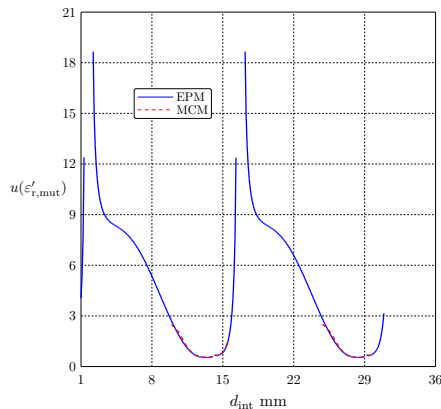


Fig. 4.8. $u(\varepsilon'_{r,\text{mut}})$ as a function of d_{int} .

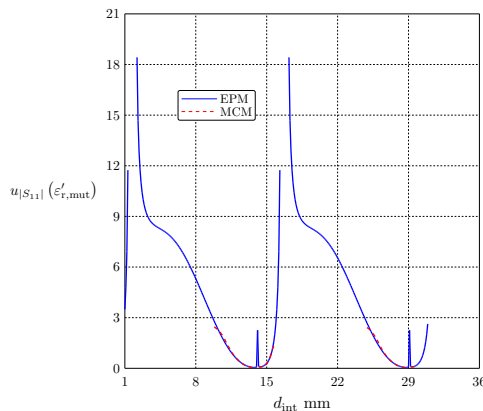


Fig. 4.9. $u_{|S_{11}|}(\varepsilon'_{r,\text{mut}})$ as a function of d_{int} .

Fig. 4.8 reveals that there are optimal values of d_{int} at which the value of the total uncertainty is considerably smaller than at other values. In this case the optimal values of d_{int} are approximately $d_{\text{int}} = 14$ and $d_{\text{int}} = 28$.

Fig. 4.10 shows the uncertainty component due to the thickness of the MUT, d_{mut} , as a function of the distance between the MUT and the auxiliary slabs, d_{int} .

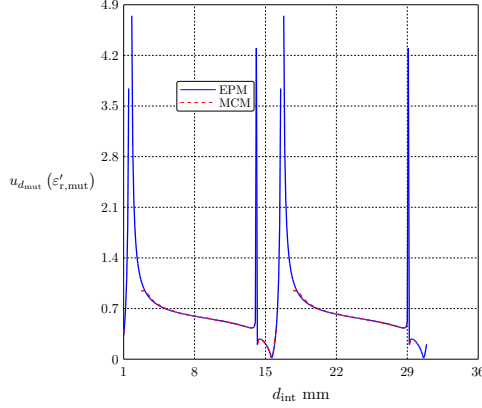


Fig. 4.10. $u_{d_{mut}}(\epsilon'_{r,mut})$ as a function of d_{int} .

Similar to the case of the two-slab waveguide model, comparing Fig. 4.9 and Fig. 4.10, one can conclude that the curves are similar and the uncertainty components are on the same order of magnitude, which means the uncertainty contribution of $|S_{11}|$ dominates in this case, as well.

Fig. 4.11 shows the uncertainty component for the thickness of the auxiliary slab, d_{aux} , as a function of d_{int} for the two-slab free-space model under study. Comparing Fig. 4.10 and Fig. 4.11 shows that the uncertainty components for d_{mut} and d_{aux} are on the same order of magnitude.

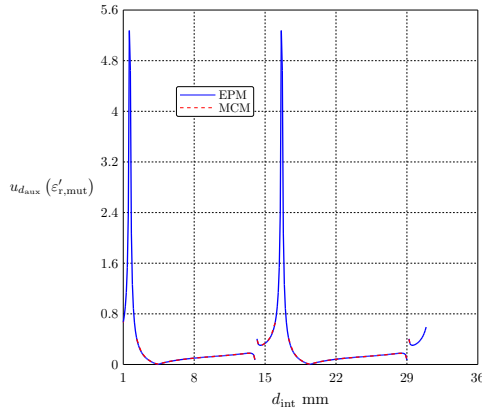


Fig. 4.11. $u_{d_{aux}}(\epsilon'_{r,mut})$ as a function of d_{int} .

Therefore, if the corresponding measurement uncertainties are the same or comparable, they will contribute comparably to the total dielectric constant measurement uncertainty.

As can be seen in Fig. 4.11, the uncertainty component for the auxiliary slab thickness exhibits two noticeable minima at $d_{int} = 4$ and $d_{int} = 18$. In contrast to the two-slab waveguide measurement method, in this case, the minima are not very narrow. However, the uncertainty component for the MUT slab thickness takes minimum values at different d_{int} , namely, 16 and

31, which means that in this case, it is not possible to reduce both uncertainty components simultaneously significantly. Fig. 4.12 shows the uncertainty component for the dielectric constant of the auxiliary slab against d_{int} and Fig. 4.13 presents the uncertainty component for the loss tangent of the auxiliary slab against d_{int} .

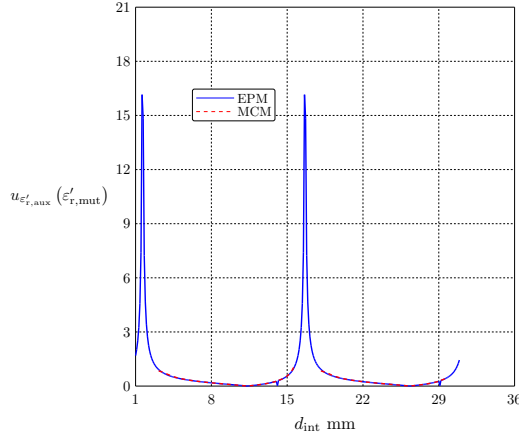


Fig. 4.12. $u_{\epsilon'_{\text{aux}}}(\epsilon'_{\text{r,mult}})$ as a function of d_{int} .

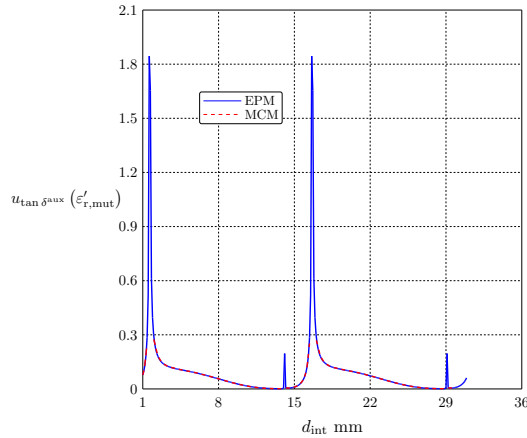


Fig. 4.13. $u_{\tan \delta_{\text{aux}}}(\epsilon'_{\text{r,mult}})$ as a function of d_{int} .

The contribution of the auxiliary slab loss tangent is smaller than that of the dielectric constant, but it is not considerably smaller compared to the case of the two-slab free space model studied in section 3.4. Furthermore, Fig. 4.12 indicates that there are two minima of the uncertainty component for the dielectric constant of the auxiliary slab at approximately $d_{\text{int}} = 12$ and $d_{\text{int}} = 28$. These minima almost coincide with those observed in Fig. 4.13, however, they are located close to the values of d_{int} , which give prohibitively large uncertainty component values.

4.4 Summary

The results of the present study show that it is possible to reduce uncertainty in the dielectric constant reconstruction of a dielectric slab in free space antenna measurements by extending the set of degrees of freedom and finding optimal values of some parameters of the extended model. To extend the conventional model, one or two slabs whose EMCP are assumed to be measured a priori with sufficiently high accuracy are added to the model. It is shown that in the case of small losses, the behavior of the model under study differs only slightly from that of the lossless model. The two-slab model has a shortcoming that the shape of the measurement curve is highly sensitive to the uncertainty in the distance between the slabs. The three-slab model also exhibits the same issue, but to a lesser extent, since for a rigid material, there is no need to measure the distance between the main slabs each time the dielectric constant needs to be measured; it suffices to measure it only once. The thickness of the middle slab can be measured beforehand by using high-precision measurement instruments to reduce the uncertainty component associated with it. However, as the results obtained for the three-slab free space model show, this model is by no means a panacea; namely, for large values of the MUT dielectric constant, it may fail to ensure lower measurement uncertainty than the conventional one.

5. TWO-ROD MEASUREMENT MODEL

5.1 Two-Rod Model

5.1.1 Overview of Two-Rod model

This chapter describes an extended measurement model composed of two H-plane full-height dielectric rods in a rectangular waveguide [132]. One of these rods is made of the material under study, the dielectric constant of which is to be determined from a measured $|S_{11}|$. The second rod is an auxiliary rod whose dimensions and material properties are known and the dielectric constant measurements are made at a frequency chosen so that only the fundamental mode can propagate in the waveguide. The distance between the rods and the radius of the auxiliary rods are treated as model optimization parameters. The fast integral equation method developed by the author is utilized to solve the forward scattering problem as it gives accurate results while requiring significantly less computing time compared to other methods. The geometry of the model is shown in Fig. 5.1.

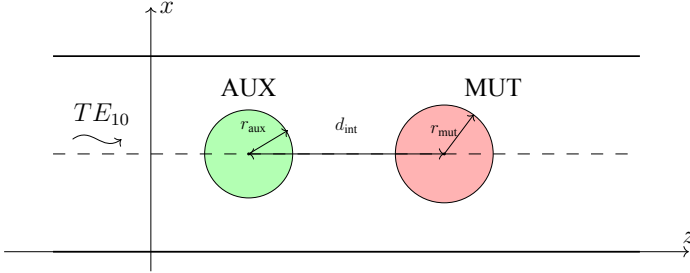


Fig. 5.1. Extended two-rod measurement model geometry.

Cylindrical samples are considered since most of the microwave resonators supplied by the world's leading manufacturers are cylindrical owing to the fact that they are easier to produce.

5.1.2 Uncertainty Analysis for Two-rod model

The rods are assumed to be located in a standard rectangular waveguide WR-90 with a width of the broader wall of 22.86 mm. The MUT is assumed to be made of Arlon AD1000 [95], whereas the auxiliary rod is assumed to be made of Arlon AD430 [98]. The standard uncertainties associated with the radii of the rods, waveguide width, and interrod distance are equal to 0.02 mm. The absolute standard uncertainty associated with the dielectric constant of the auxiliary rod is assumed to be 0.043, which corresponds to 2% [6] relative expanded measurement uncertainty. The absolute standard uncertainty associated with the loss tangent of the auxiliary rod is $5.0 \cdot 10^{-5}$ [6]. It is assumed that the auxiliary rod was characterized using a re-entrant cavity measurement method [6].

The parameters of the examined two-rod measurement model are summarized in Table 5.1.

It is assumed that the reflection coefficient is measured with the aid of Vector Network Analyzer P5024B. In general, Spectrum Analyzers can also be utilized since they measure the absolute value of the reflection coefficient and the absolute value of the reflection, which is the

quantity of interest in the present study; however, the uncertainty associated with the $|S_{11}|$ for these devices is larger than for VNAs. This is due to the calibration - knowing only one of the four scattering parameters does not suffice to eliminate multiple error terms, such as reflection tracking, transmission tracking, directivity, and isolation.

Table 5.1

Two-rod waveguide model parameters

Model Parameter	Symbol	Value	Standard uncertainty value
MUT dielectric constant	$\epsilon'_{r,mut}$	10.2	-
MUT loss tangent	$\tan \delta_{mut}$	0.0023	$1.15 \cdot 10^{-4}$
Dielectric constant of the auxiliary rod	$\epsilon'_{r,aux}$	4.3	0.043
Auxiliary rod loss tangent	$\tan \delta_{aux}$	0.003	$5.0 \cdot 10^{-5}$
MUT rod radius	r_{mut}	2.5 mm	0.01 mm
Auxiliary rod radius	r_{aux}	5.7 mm	0.01 mm
Interrod distance	d_{int}	8.6 mm	0.01 mm
Frequency	f	10 GHz	35 MHz
Waveguide width	a	22.86 mm	0.01 mm

The calculated $|S_{11}|$ as a function of $\epsilon'_{r,mut}$ for both the conventional model (CSRWM) containing the MUT only and the extended model (ETRWM) formed from it by adding one more slab is shown in Fig. 5.2. Similar to the previous model, in this case, the dimensions of the MUT and the measurement frequency are such that the sensitivity of the conventional model is pretty low, which means that this model is not suitable for dielectric constant measurements as it would give a large measurement uncertainty. As can be seen, the presence of the auxiliary slab affects the slope of the measurement curve; namely, it is significantly higher than in the case of the conventional model.

The horizontal bars appearing in the figure represent the confidence intervals associated with the $|S_{11}|$ are represented in Fig. 5.2. The blue bar corresponds to the confidence interval of the $|S_{11}|$ of the conventional model, whereas the red one refers to the possible values of the $|S_{11}|$ of the extended model. The width of the confidence interval for $|S_{11}|$ for both models is assumed to be equal to 0.005, and the confidence level of the confidence intervals is 68%. As can be seen, the width of the confidence interval for $\epsilon'_{r,mut}$ is approximately 5.4 times smaller. Thus, the conventional model is less suitable because of low sensitivity, but direct uncertainty estimation is required to find the amount by which the extended model reduces the measurement uncertainty.

The results of the MCM estimation for the given measurement model are presented in Fig. 5.3. The MCM iteration (trial) number was set to 100000. The error of the estimation does not exceed 2% in the regions of interest, but in the regions where the MCM method fails, the

error may be larger.

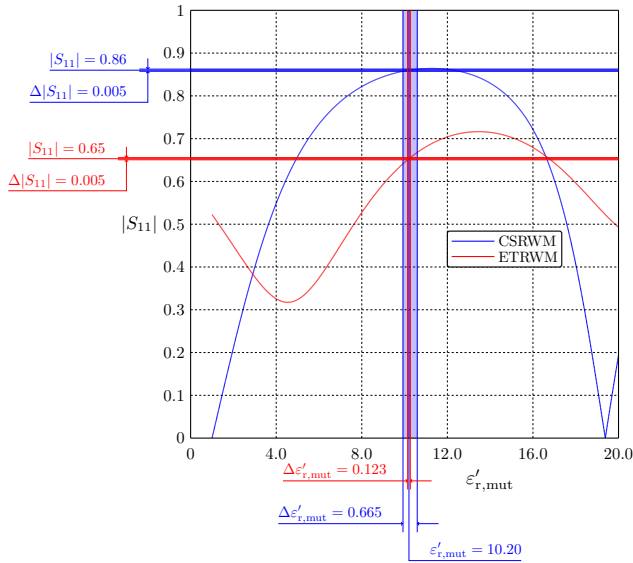


Fig. 5.2. $|S_{11}|$ as a function of $\epsilon'_{r,mut}$ and confidence interval widths for the conventional (CSRWM) and the extended (ETRW) models.

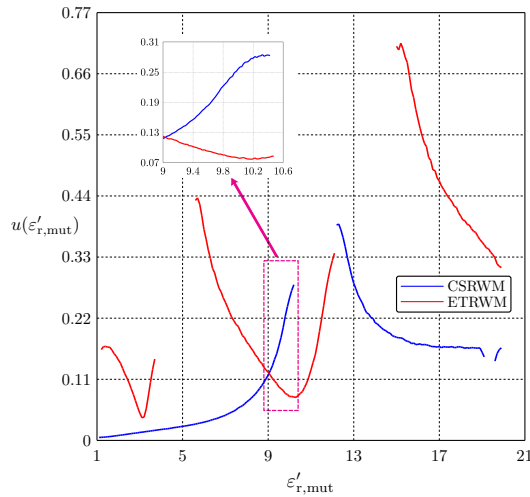


Fig. 5.3. The standard uncertainty as a function of $\epsilon'_{r,mut}$ for the conventional (CSRWM) and the extended (ETRW) models.

The estimation results show that the uncertainty obtained with the extended model is approximately 4.1 times smaller, namely, 0.29 and 0.07 obtained with the conventional and extended models, respectively.

For large values of $\varepsilon_{r,\text{aux}}$ and r_{aux} , the measurement procedure becomes slightly more complicated because of the presence of spikes (resonances exhibiting very rapid variation of $|S_{11}|$ as $\varepsilon'_{r,\text{aux}}$ is varied) in low-sensitivity regions, which are not observed in the slab-based measurement models. The effects of the spikes can be reduced by varying slightly the frequency at which the measurements are performed. Fortunately, the width of the region containing the spike is usually so small that the variation of the dielectric constant due to dispersion can be considered negligible. Also, these spikes can be easily detected, as large variations in the absolute value of the reflection coefficient due to small frequency deviations may indicate a spike's presence.

5.2 Summary

To verify the efficiency of the proposed methodology, several numerical studies were carried out. It is shown that the extended two-rod model constructed from a conventional model involving the MUT slab only exhibits much higher measurement model sensitivity. The MCM estimation was performed to evaluate the standard dielectric constant measurement uncertainty. The number of MCM trials was set to 100000, which guarantees that the uncertainty estimation error is approximately 2 – 3%. Also, it was assumed that estimation for a specific set of model parameter values is invalid if the number of physically meaningless outcomes is greater than 10% of the total number of MCM trials, which allows for eliminating incorrect estimates. The estimation results show that the uncertainty obtained with the extended model is approximately 1.6 times smaller (0.29 and 0.18 obtained with the conventional and extended models, respectively) for the MUT made of Arlon AD1000. This means that the extended two-rod measurement model is a simple and sufficiently efficient means of reducing the measurement uncertainty. Thus, the obtained results successfully prove the hypothesis that it is possible to reduce the uncertainty when the conventional model is unsuitable for dielectric constant measurements due to low sensitivity and the dimensions, and the frequency cannot be changed.

6. FAST INTEGRAL EQUATION METHOD

6.1 Multiple Dielectric Rod Structures

At the beginning of this section, an introductory overview of various methods for solving the forward scattering problems by dielectric cylindrical rods in a rectangular waveguide is presented. The main objective of this survey is to ascertain which of the methods is the most suitable method for the computation of the reflection and transmission coefficients of the dominant mode scattered by a circular cylindrical rod in a rectangular waveguide and to extend it to handle multi-layered dielectric rods, as well.

The main motivation behind the development of a rapid method for calculating the scattering data in the case of multi-layered configurations is the fact that some samples to be characterized may not have a purely cylindrical shape but may, for example, have an annular cross-sectional shape. Additionally, in the measurements of the dielectric constant of various liquids, including, among others, human blood, and seawater, the material under test must be placed in some container whose walls must be penetrable to electromagnetic waves, i.e., must be made of some dielectric materials. The same applies to the measurement of pulverized materials, such as various powders, flour, etc. For example, a cylindrical container with thin dielectric walls may be regarded as a two-layered rod whose inner layer is the material under study, whereas the container wall corresponds to the outer layer.

In order to accelerate the uncertainty estimation process, one needs to find a fast approach; otherwise, a prohibitively large amount of CPU time makes the characterization completely impractical. In addition, the algorithm for solving the corresponding inverse scattering problem can be employed for the measurements of the complex dielectric constant, as a plastic tube filled with a liquid with the complex dielectric can be treated as a two-layered rod.

6.1.1 Overview of General Purpose Numerical Methods

Several most commonly used general-purpose numerical methods are the method of moments [101], finite element method (FEM), finite difference method (FD) [102], and transmission line matrix (TLM), just to name a few. Which method to choose depends on the structure under consideration and type of excitation: short pulse or wide spectrum signal. For the sake of convenience, as well as to explain the reason why the author uses some specialized methods of solving the problem at hand, a brief discussion of the most widely used methods, as well as their advantages and disadvantages, is given below.

Transmission line matrix method. In this method, media under study or structures are treated as an array (matrix, hence the name of the method) composed of two sets of parallel transmission lines arranged in such a way that the lines of these two sets are mutually perpendicular. The pulses traveling down these lines exhibit behavior similar to that of the plane wave in the free space, provided that the distance between the nodes of the matrix, i.e., points where the lines meet, is much smaller compared to a wavelength in the medium being modeled. As a result, modeling of high dielectric constant rods or, in general, objects of other shapes becomes a highly computationally expensive task due to the large number of discretization cells needed

to guarantee satisfactory field resolution.

Finite difference time domain. This method is based on the FD approximation of the derivatives in the governing partial differential equations that results in a set of update equations that allows one to calculate the values of electric and magnetic fields for all the time instants starting from a given initial values at all the points in the computational domain.

Finite element method. In the FEM, the governing differential equations are solved via discretization of the function being sought that, in turn, involves the discretization of the modeling domain – some region of space where the fields are confined or just part of the region of interest like in the case of antenna modeling and study of the scattering of incident electromagnetic wave, e.g., a plane wave, by a dielectric or any other body of arbitrary shape.

Method of Moments. The method of moment, or integral equation method, or when applied to surfaces only, is referred to as the Boundary Integral method (Boundary element method). This method is based on the surface or volume equivalence principle that enables one to derive a set of integral equations from Maxwell's equations using the so-called fundamental solution or Green's function. The function can be regarded as the field electric due to a unit point source, i.e., a source that is a unit amplitude charge or current (dipole) of infinitely small size. One can derive the integral equations by combining the governing wave equations (in general inhomogeneous – due to the presence of sources) with the equation for Green's function with the aid of the well-known second Green's identity. The integral equation derived this way does not need to satisfy any boundary conditions on the boundary surface of the domain explicitly. Thus, there is no need to discretize space around the object under study in contrast to other methods such as the FEM, etc. However, the evaluation of the system matrix entries, in this case, is far more time-consuming as one has to integrate the function (integrand) that exhibits singular behavior, i.e., as the source point approaches the observation point, the value of the function grows unboundedly [100].

6.1.2 Semi-Analytic Methods for Handling Cylindrical Obstacles

Although the problem can be solved using one of the well-established general-purpose methods or software employing them (e.g., Ansys HFSS, CST Studio, Comsol, etc.), they are typically highly computationally demanding. This is because these methods do not account for some useful properties of the problem geometry, such as the capability of being divided into regions with simple geometry, e.g., cylindrical, spherical, elliptical, spheroidal, etc. These geometrical properties reduce computational effort by solving part of the forward scattering problem analytically or at least by converting a problem to its simpler equivalent that is less computationally expensive to handle.

A number of approaches exploiting the geometrical peculiarities of the problem have been proposed during the last decades. The first work devoted to discontinuities in waveguides was the Notes on Lectures by J. Schwinger [103]. This work presents solutions to a number of waveguide discontinuity problems, among which there is a solution to a problem of scattering by a circular rod in a rectangular waveguide obtained via the use of the variational method.

The method consists in replacing the original problem with a problem of finding the stationary point of a functional. Schwinger formed the functional from the quantities characterizing the equivalent T network for an inductive rod. The scattering problem by a perfectly conducting metal rod and a dielectric one was treated separately in [103]. In addition to deriving mathematical expressions for the evaluation of the equivalent circuit parameters, two useful differential operators were utilized, allowing lowering and raising the order of the so-called cylindrical harmonics to be discussed in what follows. In the case of the dielectric rod, the fields inside it were approximated using a truncated cylindrical wave expansion, as these functions are the most suitable for homogeneous objects with a cylindrical shape. More specifically, they allow one to use the same functions for approximating magnetic and electric fields.

The expressions derived in [103] were subsequently used by Marcuwitz to calculate the equivalent circuit parameters for both centered and offset rods in a rectangular waveguide, as reported in [104]. However, for the handbook, Marcuwitz used only a first-order approximation of fields inside the rods; namely, only the first term was retained in both odd- and even-case series. Furthermore, numerical results presented in [105] demonstrate that Schwinger's variational method with the first-order field approximation yields accurate results only for rods of small radius and small dielectric constant. In contrast, for rods with a large electrical size, the discrepancy between the calculated and experimentally obtained results becomes impractically large. In addition, the first-order approximation gives a substantial error in the vicinity of the resonant dielectric constant values, i.e., values at which the reflection coefficient attains a minimum value. For lossless rods, the minimum value of the reflection coefficient is zero, whereas for low-loss or medium-loss rods, the reflection coefficient no longer reaches zero but takes a very small value. Araneta [105] improved Schwinger's variational solution by retaining two more cylindrical terms in series expansions, thereby obtaining the second-order approximation. Although the approach provides more accurate results, it is found that in the case of second-order approximation, expressions become quite cumbersome, which makes it inconvenient to use them in practice.

An attempt to treat the problem of the scattering by a magnetized ferrite rod in a rectangular waveguide using an approach relying on the fact that the scattered fields can be computed by successively finding fields scattered by the rod ignoring the effect of the waveguide walls as if the rod was located in free space was made in [134]. The expressions derived, however, are valid only for rods with small electrical dimensions due to a number of assumptions and approximations made to derive them. Although, the method can be made more accurate by taking into account the second-order scattered-reflected fields. Theoretically, as the number of iterations tends to infinity, the sequence of approximations converges to the actual solution of the problem. In practice, however, this method proves to be useful only for rods of small electrical dimensions, as in this case, an acceptable approximation can be found just after a few iterations of the process. A rigorous multipole treatment of the same problem was proposed by Nakamoto [135]. To approximate the fields scattered by a ferrite rod, they employed a multipole expansion-based method adapted to waveguide settings. Namely, the effect of waveguide wall

reflections was accounted for through the use of the mirror image technique [100]. The fields inside the cylindrical rod are expressed in terms of an infinite sum of cylindrical waves, and the system of equations was obtained by enforcing the continuity of the fields at the surface of the rod. Although the method was applied to a single magnetized rod, it is capable of handling dielectric rods, as well, since the problem of scattering by a dielectric rod may be viewed as a special case of the one for an axially magnetized ferrite rod.

A multifilament moment solution proposed in [106] allows finding the reflection and transmission coefficients of the dominant mode scattered by a metallic rod. The scattered field produced by a rod is simulated by a set of elementary current sources infinite in extent and with unknown amplitudes to be determined. These sources are positioned on a closed surface enclosing the rod to produce an approximation of fields in the exterior of the obstacle. Also, it was shown that greater accuracy of the calculated scattering data could be achieved in the case when the shape of the closed surface is reminiscent of that of the obstacle. Subsequently, the method was extended to address the problem of scattering by dielectric [107] and composite rods [108], as well. Other authors have developed an approach to solving the problem of scattering by structures comprising a number of rods located in a rectangular waveguide [109]. In that case, the total field inside the rod is represented as a superposition of the incident wave and the unknown scattered field produced by the polarization current inside the rod. Then with the use of the waveguide Green's function, the inhomogeneous wave equation is converted to a Fredholm integral equation of the second kind containing the unknown function both under the integral sign and explicitly outside it. The integral equation is solved by dividing the cross-section of each rod into a number of elements of simple shape and applying numerical integration (numerical quadrature) [110]. Despite the great flexibility of the method, its major shortcoming is a high computational burden, in particular for rods with a high dielectric constant, as the side lengths of the simplices used to discretize the cross-section of the rod under study must be much shorter than a wavelength in the rod. In addition, the last two approaches involve the use of the waveguide Green's function, which is represented in terms of an infinite series of waveguide modes. For the computation of each entry of the generalized impedance matrix, the waveguide Green's function must be truncated and added up, which leads to a considerable increase in CPU time.

The first approach based on the division of the geometry of a problem into a number of homogeneous regions of simple geometry was proposed by Nielsen in [111]. The fact that the fields in the regions can be expressed in terms of a series of eigenfunctions of the Laplacian allows for solving a boundary problem on the interfaces between layers of the rod analytically, that, in turn, considerably reduces the computational burden and provides sufficiently high resolution of field distribution. The last step of the approach is the derivation of a system of linear equations, which is attained by using the point-matching procedure and infinite eigenfunction series truncation. However, this approach applies only to the centered rods, namely, the rods with its axis placed at equal distances from the walls of the waveguide. Furthermore, numerical studies revealed that the approach guarantees accurate results for rods with sufficiently small electrical radii only. In an attempt to overcome this limitation, the method was modified [90].

The modified subdomain method differs from the original one [111] in that the fictitious surface termed the interaction region consists of four straight line segments (in the equivalent 2D problem), two of which lie on the opposite walls of the waveguide. At the same time, the other two join their endpoints, thus forming a rectangle, which was replaced with a circular one enclosing the rod under study and centered at its axis. Hence, the radius of this imaginary surface necessary for the point-matching procedure equals half the width of the broader waveguide wall. It was shown that the circular interaction region-based method is entirely free from the divergence issue of Nielsen’s method when thick rods are considered. Additionally, it demonstrates stable convergence even for rods with a very high dielectric constant. Moreover, the approach is faster than the aforementioned approaches in terms of the computation time and provides a sufficiently high degree of accuracy of results.

To the best of the author’s knowledge, for circular centered rods in a rectangular waveguide, there is only one point-matching procedure with a circular interaction region proposed by Sahalos in [106] and subsequently improved and extended by other researchers [91, 92, 112–114] to handle composite centered rods with an arbitrary number of layers, as well as offset rods and two rods situated inside the circular interaction region [107].

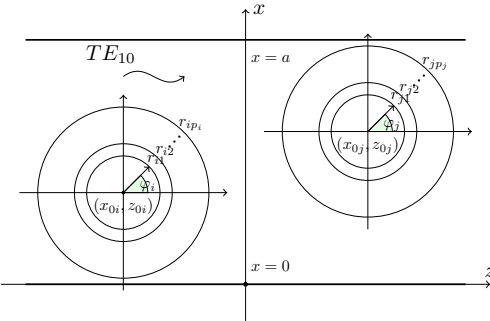


Fig. 6.1. The geometry of a multi-rod structure. [128]

The method employed here belongs to the family of boundary integral methods and is also described in one of the author’s papers [128]. The integral equations are typically obtained from the governing differential equations by using Green’s identities. However, when the object under consideration has a simple (canonical) shape, such as cylindrical, spherical, or elliptical, one can exploit the fact that the fields on surfaces can be expressed in terms of the so-called entire-domain basis functions, which typically are solutions of an appropriate differential equation and satisfy certain boundary conditions. The most appropriate in the case of cylindrical objects are periodic boundary conditions.

Solutions of the harmonic equation subject to periodic boundary conditions are obtained in the form of well-known periodic complex exponential functions. Both source and weighting surface integrals required for calculating each matrix entry can be evaluated analytically, resulting in infinite Schlömilch series. However, the series exhibit very slow convergence, thereby

degrading the efficiency of the method dramatically. From a number of approaches that have been proposed to accelerate the convergence of these series, the Ewald method [117] that for a long time was used mainly for accelerating the calculation of periodic lattice potentials [118] and only recently gained popularity in the microwave community, proves to be efficient. It is worth noting that the Ewald technique has found use in a wide variety of other applications where it is utilized to speed up the evaluation of free space Green functions [119], waveguide Green functions [120], etc. [121–123].

The comparative analysis of three different acceleration techniques presented by Linton in [124] shows that the contour integral and Ewald's summation techniques are more efficient than the Euler-Maclaurin method and the most efficient from the computational point of view is the contour integral technique. However, the numerical analysis performed by the author shows that in some cases, Ewald's summation technique is more advantageous. Specifically, for large number dielectric rods, Ewald's method converges faster than the contour integral method, since it does not require expanding Hankel functions appearing in the Schlömilch series into another series by using Graf's addition theorem, whose convergence rate decreases as the distance between the rods increases. Since in this Thesis, the general case is addressed, where the number of rods may be arbitrary, and the distances between them may also be arbitrarily large, the most suitable of the three techniques treated in [124] in terms of the rate of convergence and accuracy is that proposed by Ewald. Thus, this method has been selected for the boundary integral equation method for dielectric rods employed to speed up the scattering parameter calculation for the two-rod measurement model investigated in the present thesis, which results in a considerable acceleration of the MC uncertainty estimation process for the model.

6.1.3 Discretization of Boundary Integral Equation

It is assumed that only the dominant mode can propagate in a rectangular waveguide along the z axis. A possible geometry of the structure under consideration is illustrated in Fig. 6.1. In the general case, P inductive circular rods are placed in the rectangular waveguide, and the i -th rod consists of p_i layers. The number of layers may also be $p_i = 1$.

The problem is two-dimensional; therefore, all surface integrals over the surfaces of rods reduce to contour integrals around the circumferences of rods. Using the surface equivalence theorem, one can obtain the following surface integral equation to be solved for unknown functions $E_y(\mathbf{r})$ and $H_\varphi(\mathbf{r})$ [125]

$$E_y^i(\mathbf{r}_o) = E_y(\mathbf{r}_o) - \oint_L \left(E_y(\mathbf{r}_s) \frac{\partial G(\mathbf{r}_o, \mathbf{r}_s)}{\partial n} + jZ_0 k_0 H_\varphi(\mathbf{r}_s) G(\mathbf{r}_o, \mathbf{r}_s) \right) dl_s, \quad (6.1)$$

where

$G(\mathbf{r}_o, \mathbf{r}_s)$ - the waveguide Green's function;

$E_y^i(\mathbf{r})$ - the incident electric field, V/m;

Z_0 - the free space intrinsic impedance, Ω ;

k_0 - the free space wavenumber, 1/m;

$E_y(\mathbf{r})$ - the tangential components of the total electric fields, V/m;

$H_\varphi(\mathbf{r})$ - the tangential components of the total magnetic field, A/m.

Also, in (6.1) the subscripts s and o refer to the variables associated with the source and observation points, respectively. Here Green's function and the above-mentioned fields are considered on the surfaces of the rods, $L = \{L_1 \cup \dots \cup L_P\}$ and L_i is the circumference of the i -th rod. In order to find the unknown functions $E_y(\mathbf{r})$ and $H_\varphi(\mathbf{r})$ equation (6.1) must be recast into a weak form, by multiplying both sides of the equation by appropriate weighting functions $T_{h,\{i\}}(\varphi_{\{i\}}) = e^{-jh\varphi_{\{i\}}}$, $h = -N, -N + 1, \dots, N$ and integrating over each L_i , $i = 1, 2, \dots, P$. Then, approximating the unknown distributions of the electric $E_y(r_{\{j\}}, \varphi_{\{j\}})$ and magnetic $H_\varphi(r_{\{j\}}, \varphi_{\{j\}})$ fields on the surface of the j -th rod by a series of basis functions of the form $e^{jn\varphi_{\{j\}}}$, $n = -N, -N + 1, \dots, N$ with unknown expansion coefficients $\tilde{E}_{n,\{j\}}$ and $\tilde{H}_{n,\{j\}}$, and substituting them into (6.1), one obtains the following expressions for the entries of the submatrices \mathbf{Z}_{ij}^E and \mathbf{Z}_{ij}^H of the system matrix \mathbf{Z} and the subvector e_i of the excitation vector \mathbf{e}

$$\begin{aligned} z_{ij;(h+N+1)(n+N+1)}^E &= r_{0,\{i\}} r_{0,\{j\}} \int_0^{2\pi} \int_0^{2\pi} e^{-jh\varphi_{\{i\}}} e^{jn\varphi_{\{j\}}} \frac{\partial G(\mathbf{r}_{\{i\}}, \mathbf{r}_{\{j\}})}{\partial r_{\{j\}}} d\varphi_{\{i\}} d\varphi_{\{j\}}, \\ z_{ij;(h+N+1)(n+N+1)}^H &= -jZ_0 k_0 r_{0,\{i\}} r_{0,\{j\}} \int_0^{2\pi} \int_0^{2\pi} e^{-jh\varphi_{\{i\}}} e^{jn\varphi_{\{j\}}} G(\mathbf{r}_{\{i\}}, \mathbf{r}_{\{j\}}) d\varphi_{\{i\}} d\varphi_{\{j\}}, \\ e_{o;h+N+1} &= r_{0,\{i\}} \int_0^{2\pi} e^{-jh\varphi_{\{i\}}} E_y^i(\mathbf{r}_{\{i\}}) d\varphi_{\{i\}}, \quad h, n = -N, -N + 1, \dots, N. \end{aligned} \quad (6.2)$$

where

$\mathbf{r}_{\{i\}}$ - the position vector of point with polar coordinates $r_{\{i\}}$ and $\varphi_{\{i\}}$.

In the case of a cylindrical obstacle, the integration in (6.2) can be carried out analytically, resulting in infinite Schlömilch series. To obtain this series, one first decomposes the waveguide Green's function in the spatial form given by

$$G(\mathbf{r}_o, \mathbf{r}_s) = \frac{j}{4} \sum_{m=-\infty}^{+\infty} H_0^{(2)}(k_0 r_m^-) - \frac{j}{4} \sum_{m=-\infty}^{+\infty} H_0^{(2)}(k_0 r_m^+), \quad (6.3)$$

where

$r_m^\pm = \sqrt{(x_o \pm x_s + 2am)^2 + (z_o - z_s)^2}$ - the distance between the m -th image point of the source point and the observation point, m ;

a - the width of the broader wall of the waveguide, m .

Using the Graf addition theorem for cylindrical functions [116] one finds the decomposi-

tion of the m -th term of both sums in (6.3) in terms of the local coordinates $(r_{\{i\}}, \varphi_{\{i\}})$ and $(r_{\{j\}}, \varphi_{\{j\}})$ with origins at $(x_{0,\{i\}}, z_{0,\{i\}})$ and $(x_{0,\{j\}}, z_{0,\{j\}})$ associated with the i -th and j -th rods, respectively

$$H_0^{(2)}(k_0 r_m^\mp) = \sum_{k,l=-\infty}^{+\infty} H_{-l\pm k}^{(2)}(k_0 r_{m,\{i,j\}}^\mp) J_{\pm k}(k_0 r_j) J_l(k_0 r_i) e^{j((-l\pm k)\varphi_m^- - k\varphi_j + l\varphi_i)}, \quad (6.4)$$

where

$$\begin{aligned} r_{m,i,j}^\pm &= \sqrt{(x_{0,\{i\}} \pm x_{0,\{j\}} + 2am)^2 + (z_{0,\{i\}} - z_{0,\{j\}})^2}; \\ \varphi_m^\pm &= \arctan((x_{0,\{i\}} \pm x_{0,\{j\}} + 2am)/(z_{0,\{i\}} - z_{0,\{j\}})); \\ r_k &= \sqrt{(x - x_{0,\{k\}})^2 + (z - z_{0,\{k\}})^2}; \\ \varphi_i &= \arctan((x_s - x_{0,\{i\}})/(z_s - z_{0,\{i\}})); \\ \varphi_j &= \arctan((x_s - x_{0,\{j\}})/(z_s - z_{0,\{j\}})). \end{aligned}$$

Substituting (6.4) into (6.3), and then the resulting expression into (6.2), as well as performing integration of both source and test integrals the original triple series reduces, due to orthogonality, to a single one

$$\begin{aligned} z_{ij;(h+N+1)(n+N+1)}^H &= -jZ_0 \left(S_{n-h}^- - (-1)^n S_{-(n+h)}^+ \right) J_h(k_0 r_{0,\{i\}}) J_n(k_0 r_{0,\{j\}}), \\ z_{ij;(h+N+1)(n+N+1)}^E &= \left(S_{n-h}^- - (-1)^n S_{-(n+h)}^+ \right) J_h(k_0 r_{0,\{i\}}) J'_n(k_0 r_{0,\{j\}}), \end{aligned} \quad (6.5)$$

where

$$S_l^\pm = jk_0 \pi^2 r_{0,\{i\}} r_{0,\{j\}} \sum_{m=-\infty}^{+\infty} H_l^{(2)}(k_0 r_{m,i,j}^\pm) e^{il\varphi_m^\pm} - \text{the } l\text{-th order Schl\"omilch series.}$$

In order to accelerate the convergence of the Schl\"omilch series S_0^+ and S_0^- appearing in (6.5), the Ewald summation method [117] is utilized. The improvement in the convergence is achieved by splitting the original series into a slowly and a rapidly convergent series in such a way that the convergence of the slowly convergent one can be substantially accelerated by means of the Poisson summation method. The expressions for S_l^+ and S_l^- can be obtained from those for S_0^+ and S_0^- using forward and backward recurrence relations for Hankel functions [126]. For $i = j$ the term $m = 0$ in the first sum in (6.2) must be excluded and treated separately

$$\begin{aligned} z_{ii;(n+N+1)(n+N+1)}^{DH} &= Z_0 k_0 \pi^2 r_{0,\{i\}}^2 H_n^{(2)}(k_0 r_{0,\{i\}}) J_n(k_0 r_{0,\{i\}}), \\ z_{ii;(n+N+1)(n+N+1)}^{DE} &= jk_0 \pi^2 r_{0,\{i\}}^2 H_n^{(2)}(k_0 r_{0,\{i\}}) J'_n(k_0 r_{0,\{i\}}). \end{aligned} \quad (6.6)$$

Finally, one has

$$(\mathbf{Z}^H + \mathbf{Z}^{DH}) \mathbf{x}^h + (\mathbf{I}^r + \mathbf{Z}^E + \mathbf{Z}^{DE}) \mathbf{x}^e = \mathbf{e}, \quad (6.7)$$

where

$$\mathbf{I}_{ii}^r = 2\pi r_{0,\{i\}} \mathbf{I} - \text{the } (i\text{-th}, i\text{-th}) \text{ submatrix of matrix } \mathbf{I}^r;$$

I - the $2N + 1 \times 2N + 1$ identity matrix;

\mathbf{x}^e - the vector containing unknown expansion coefficients $\tilde{E}_{n,\{j\}}$;

\mathbf{x}^h - the vector containing unknown expansion coefficients $\tilde{H}_{n,\{j\}}$.

To find the relations between the tangential components of the magnetic and electric fields on the surface of the j -th rod, one first needs to find expansions for the fields in each layer of the rod. The electric field in the o -th layer of the j -th rod satisfies the homogeneous Helmholtz equation; consequently, the electric field inside this layer can be expanded into the series of solutions to this equation in cylindrical coordinates

$$E_y^{(j,o)}(r_{\{j\}}\varphi_{\{j\}}) = \sum_{n=-\infty}^{+\infty} (A_{n,\{j,o\}}J_n(k_{\{j,o\}}r_{\{j\}}) + B_{n,\{j,o\}}Y_n(k_{\{j,o\}}r_{\{j\}})) e^{in\varphi_{\{j\}}}, \quad (6.8)$$

where

$k_{\{j,o\}}$ - the wavenumber of the zeroth layer of the j -th rod, $1/m$;

$A_{n,\{j,o\}}$ and $B_{n,\{j,o\}}$ - the unknown expansion coefficients.

The corresponding expansion for the magnetic field can be found by using Maxwell's equations. The relation between $A_{n,\{j\}}$ and $B_{n,\{j\}}$ can be determined by enforcing continuity of the tangential components of the fields on each interface of the j -th rod, as well as taking advantage of the orthogonality with respect to $\varphi_{\{j\}}$ that results in infinitely many decoupled systems of equations, each involving only n -th unknown expansions coefficients for all layers of the rod. Then, $g_{n,\{j\}} = B_{n,\{j\}}/A_{n,\{j\}}$ can be found by means of the following recurrence relation, which can be obtained by eliminating all unknown coefficients successively, except $A_{n,\{j\}}$ and $B_{n,\{j\}}$ from the corresponding set of equations, starting with the innermost layer

$$g_{n,\{j,o\}} = \frac{\tilde{k}_{\{j,o\}}J_{n-1}(\tilde{k}_{\{j,o\}})Q_{n,\{j,o\}}(\tilde{k}_{\{j,(o-1)\}}) - \tilde{k}_{\{j,(o-1)\}}J_n(\tilde{k}_{\{j,o\}})Q_{(n-1),\{j,o\}}(\tilde{k}_{\{j,(o-1)\}})}{\tilde{k}_{\{j,(o-1)\}}Y_n(\tilde{k}_{\{j,o\}})Q_{(n-1),\{j,o\}}(\tilde{k}_{\{j,(o-1)\}}) - \tilde{k}_{\{j,o\}}Y_{n-1}(\tilde{k}_{\{j,o\}})Q_{n,\{j,o\}}(\tilde{k}_{\{j,(o-1)\}})}, \quad (6.9)$$

where

$$Q_{n,\{j,o\}}(x) = J_n(x) + g_{n,\{j,(o-1)\}}Y_n(x);$$

$$\tilde{k}_{\{j,o\}} = k_{\{j,o\}}r_{\{j,(o-1)\}} - \text{the normalized wavenumber};$$

$$g_{n,\{j,1\}} = 0.$$

By using this result and continuity of the electric and magnetic fields across the surface of the j -th rod, the following relation between the two sets of unknown expansion coefficients $\tilde{E}_{n,\{j\}}$ and $\tilde{H}_{n,\{j\}}$ can be found

$$\begin{aligned} x_{j;n+N+1}^e &= d_{j;n+N+1}x_{j;n+N+1}^h \\ &= jZ_{\{j,p_j\}} \frac{J_n(k_{\{j,p_j\}}r_{\{j,p_j\}}) + g_{n,\{j,p_j\}}Y_n(k_{\{j,p_j\}}r_{\{j,p_j\}})}{J'_n(k_{\{j\}}r_{\{j,p_j\}}) + g_{n,\{j,p_j\}}Y'_n(k_{\{j,p_j\}}r_{\{j,p_j\}})} x_{j;n+N+1}^h. \end{aligned} \quad (6.10)$$

Substituting this expression into (6.7), yields

$$\left((\mathbf{Z}^H + \mathbf{Z}^{DH}) + (\mathbf{I}_r + \mathbf{Z}^E + \mathbf{Z}^{DE}) \mathbf{D} \right) \mathbf{x}_h = \mathbf{e}. \quad (6.11)$$

Solving equation system (6.11) gives the field expansion coefficients from which both the reflection and transmission coefficients can be readily extracted by carrying out integration over the surface of each rod. Fortunately, in this case, the integral can be evaluated in closed form owing to the well-known Jacobi-Anger expansion of the exponential function. Furthermore, the expansion is valid not only for the real angles but also for complex ones arising when higher-order mode scattering data (generalized scattering matrix elements) need to be retrieved. This advantageous property appreciably facilitates the analysis of the rod-based structures under consideration.

For the sake of convenience, henceforth, the general case mathematical expressions for the zeroth order term of Schlömilch series will be considered. To obtain from the general case expression those corresponding to S_0^+ one needs to substitute $x_{0,\{i\}} + x_{0,\{j\}} + 2ma$ and $z_{0,\{i\}} - x_{0,\{j\}}$ for x_m and z , respectively. Regarding the other type of the Schlömilch series, namely, S_0^- , the relevant expressions can be readily obtained by making the following substitution: $x \rightarrow x_{0,\{i\}} - x_{0,\{j\}} + 2ma$ and $z \rightarrow x_{0,\{i\}} - x_{0,\{j\}}$

Additionally, in what follows, the use will be made of two differential operators for raising and lowering the order of the Hankel function appearing in the Schlömilch series, which considerably simplifies the derivation of the expressions for Schlömilch series of orders other than 0.

The order raising operator is defined as

$$-\frac{1}{k_0} \left(\frac{\partial}{\partial z} + j \frac{\partial}{\partial x} \right) \mathbf{H}_n^{(2)} \left(k_0 \sqrt{x^2 + z^2} \right) \mathbf{e}^{jn\varphi} = \mathbf{H}_{n+1}^{(2)} \left(k_0 \sqrt{x^2 + z^2} \right) \mathbf{e}^{j(n+1)\varphi} \quad (6.12)$$

and its order-lowering counterpart as

$$-\frac{1}{k_0} \left(\frac{\partial}{\partial z} - j \frac{\partial}{\partial x} \right) \mathbf{H}_n^{(2)} \left(k_0 \sqrt{x^2 + z^2} \right) \mathbf{e}^{jn\varphi} = \mathbf{H}_{n-1}^{(2)} \left(k_0 \sqrt{x^2 + z^2} \right) \mathbf{e}^{j(n-1)\varphi} \quad (6.13)$$

where

$$\varphi = \begin{cases} \arctan \frac{x}{z} & \text{if } x \geq 0 \\ \varphi = \pi - \arctan \frac{x}{z} & \text{if } x < 0 \end{cases}.$$

For the above-mentioned general case, the Schlömilch series can be expressed as

$$\hat{S} = \sum_{m=-\infty}^{+\infty} \mathbf{H}_0^{(2)} \left(k_0 \sqrt{x_m^2 + z^2} \right). \quad (6.14)$$

Now, to transform this into the dual series by means of the Poisson summation method, one needs to find the following Fourier transform that can be recognized as one of several integral

representations of the zeroth order Hankel function of the second kind

$$H_0^{(2)}\left(k_0\sqrt{x^2+z^2}\right) = -\frac{j}{\pi^2} \int_{-\infty}^{+\infty} \int_{-\infty}^{+\infty} \frac{e^{-jk_x x} e^{-jk_z z}}{k_0^2 - k_x^2 - k_z^2} dk_z dk_x. \quad (6.15)$$

Thus, using the double integral representation of the zeroth order Hankel function of the second kind for the above-mentioned general case, the Schlömilch series can be expressed as

$$\hat{S} = -\frac{j}{\pi^2} \sum_{m=-\infty}^{+\infty} \int_{-\infty}^{+\infty} \int_{-\infty}^{+\infty} \frac{e^{-jk_x x_m} e^{-jk_z z}}{k_0^2 - k_x^2 - k_z^2} dk_z dk_x. \quad (6.16)$$

The integral appearing on the right-hand side of (6.16) can be regarded as the two-dimensional Fourier transform of the following function with respect to spectral variables k_x and k_z

$$\frac{1}{k_0^2 - k_x^2 - k_z^2}, \quad (6.17)$$

which can be expressed as

$$\frac{1}{k_0^2 - k_x^2 - k_z^2} = -\int_0^{-j\infty} e^{t(k_0^2 - k_x^2 - k_z^2)} dt. \quad (6.18)$$

In (6.18) the integration is performed along the negative imaginary axis to ensure convergence of the improper integral irrespective of whether $k_0^2 - k_x^2 - k_z^2$ is positive or not. Note that this integral is convergent only when the imaginary part of k_0 is positive. The case of real k_0 can be obtained by taking the limit as the imaginary part tends to zero.

Now, using (6.18), the Hankel function can be written as

$$\int_{-\infty}^{+\infty} \int_{-\infty}^{+\infty} \frac{e^{-jk_x x} e^{-jk_z z}}{k_0^2 - k_x^2 - k_z^2} dk_x dk_z = -\int_{-\infty}^{+\infty} \int_{-\infty}^{+\infty} \int_0^{-j\infty} e^{-jk_x x} e^{-jk_z z} e^{t(k_0^2 - k_x^2 - k_z^2)} dt dk_x dk_z. \quad (6.19)$$

The integration with respect to k_x and k_z can be evaluated in closed form as the functions being transformed are, in fact, Gaussian functions in k_x and k_z , respectively. However, in the present case, it is unnecessary, as the main objective is to speed up the convergence of the Schlömilch series. To that end, the integral along the imaginary axis can be divided into two integrals by deforming the contour of integration. This trick will finally lead to two rapidly converging series. The parameter α must be a positive real number, and as will be seen later, it allows one to control the convergence of the two series. More specifically, the contour of integration is deformed so that the resulting one consists of two parts, one being the straight line segment that emerges from the origin and goes to the point α^2 on the real axis. The second part is a ray that emerges from point α^2 and goes to infinity parallel to the imaginary axis.

Thus, by dividing the integration contour as described above, one obtains

$$\int_0^{-j\infty} e^{t(k_0^2 - k_x^2 - k_z^2)} dt = \int_0^{\alpha^2} e^{t(k_0^2 - k_x^2 - k_z^2)} dt + \int_{\alpha^2}^{-j\infty} e^{t(k_0^2 - k_x^2 - k_z^2)} dt. \quad (6.20)$$

Substituting (6.20) into (6.16), one achieves the following splitting of the original series into two parts

$$\hat{S} = \hat{S}^{\text{spec}} + \hat{S}^{\text{spac}} = -\frac{j}{\pi^2} \sum_{m=-\infty}^{+\infty} I_m^{\text{spec}} + \frac{j}{\pi^2} \sum_{m=-\infty}^{+\infty} I_m^{\text{spac}}, \quad (6.21)$$

where

$$I_m^{\text{spec}} = - \int_{-\infty}^{+\infty} \int_{-\infty}^{+\infty} \int_{\alpha^2}^{-j\infty} e^{-jk_x x m} e^{-jk_z z} e^{t(k_0^2 - k_x^2 - k_z^2)} dt dk_x dk_z;$$

$$I_m^{\text{spac}} = \int_{-\infty}^{+\infty} \int_{-\infty}^{+\infty} \int_0^{\alpha^2} e^{-jk_x x m} e^{-jk_z z} e^{t(k_0^2 - k_x^2 - k_z^2)} dt dk_x dk_z.$$

The first of the resulting series is termed the spectral series and can be evaluated as it stands owing to sufficiently rapid convergence. However, the other series exhibits prohibitively slow convergence and therefore needs to be accelerated. In the present work, as well as in many other works, it is achieved by means of the Poisson summation formula, which relies upon Fourier transform, as well as the fact that rapidly decaying functions have wide spectra and vice versa.

6.1.4 Evaluation of the Spectral Series Terms

The Poisson method requires applying the Fourier transform to the generating function of the original series to obtain that of the dual series. The generating function for slowly converging series \hat{S}^{spec} is obtained by performing integration along the imaginary axis, which in this case can be accomplished analytically

$$I^{\text{spec}}(x) = \int_{-\infty}^{+\infty} \int_{-\infty}^{+\infty} e^{-jk_x x} e^{-jk_z z} \frac{e^{\alpha^2(k_0^2 - k_x^2 - k_z^2)}}{k_0^2 - k_x^2 - k_z^2} dk_x dk_z \quad (6.22)$$

Then the Fourier transform with respect to x is applied to (6.23) to derive the generating function for the equivalent dual series

$$I^{\text{spec}}(\hat{k}_x) = \int_{-\infty}^{+\infty} e^{j\hat{k}_x x} \int_{-\infty}^{+\infty} \int_{-\infty}^{+\infty} e^{-jk_x x} e^{-jk_z z} \frac{e^{\alpha^2(k_0^2 - k_x^2 - k_z^2)}}{k_0^2 - k_x^2 - k_z^2} dk_x dk_z dx$$

$$= 2\pi \int_{-\infty}^{+\infty} \int_{-\infty}^{+\infty} \delta(k_x - \hat{k}_x) e^{-jk_z z} \frac{e^{\alpha^2(k_0^2 - k_x^2 - k_z^2)}}{k_0^2 - k_x^2 - k_z^2} dk_x dk_z = 2\pi \int_{-\infty}^{+\infty} e^{-jk_z z} \frac{e^{\alpha^2(k_0^2 - \hat{k}_x^2 - k_z^2)}}{k_0^2 - \hat{k}_x^2 - k_z^2} dk_z. \quad (6.23)$$

Hence, the series dual to the slowly converging spectral series are

$$\hat{S}^{\text{spec}} = \frac{1}{2a} \sum_{m=-\infty}^{+\infty} I^{\text{spec}}(\gamma_m) = \frac{\pi}{a} \sum_{m=-\infty}^{+\infty} \int_{-\infty}^{+\infty} e^{-jk_z z} \frac{e^{\alpha^2(k_0^2 - \gamma_m^2 - k_z^2)}}{k_0^2 - \gamma_m^2 - k_z^2} dk_z, \quad (6.24)$$

where

$$\gamma_m = \frac{m\pi}{a} - \text{the transverse wavenumber for the TE}_{m0} \text{ mode, } 1/m.$$

The Fourier integral with respect to k_z appearing in (6.24) can be conveniently found by treating the function being transformed as the product of two functions, namely, the Gaussian function

$$\Psi(k_z) = e^{\alpha^2(k_0^2 - \gamma_m^2 - k_z^2)}, \quad (6.25)$$

and the following function

$$\Xi(k_z) = \frac{1}{k_0^2 - \gamma_m^2 - k_z^2}, \quad (6.26)$$

and then finding the convolution of their Fourier transforms

$$\text{Int}^{\text{spec}}(z) = \frac{1}{2\pi} \int_{-\infty}^{+\infty} \xi(z-v)\psi(v) dv, \quad (6.27)$$

where

$$\xi(z) = \int_{-\infty}^{+\infty} \Xi(k_z) e^{-jk_z z} dk_z;$$

$$\psi(z) = \int_{-\infty}^{+\infty} \Psi(k_z) e^{-jk_z z} dk_z.$$

The expression for $\psi(k_z)$ can be found with the aid of integration on the complex plane using Jordan's lemma [127], and is as follows

$$\xi(z) = j \frac{\pi}{k_m} e^{-jk_m |z|}. \quad (6.28)$$

The expression for $\xi(k_z)$ is a Gaussian function, as the Fourier transform of a Gaussian function is another Gaussian function. Thus,

$$\psi(z) = \frac{\sqrt{\pi}}{\alpha} e^{\alpha^2(k_0^2 - \gamma_m^2)} e^{-\frac{z^2}{4\alpha^2}}. \quad (6.29)$$

As a result, the convolution integral becomes

$$I^{\text{spec}}(\gamma_m) = j \frac{\sqrt{\pi}^3}{\alpha} \frac{1}{k_m} e^{\alpha^2(k_0^2 - \gamma_m^2)} \int_{-\infty}^{+\infty} e^{-\frac{v^2}{4\alpha^2}} e^{-jk_m|z-v|} dv. \quad (6.30)$$

The presence of the absolute sign requires splitting the integral into two parts by choosing the integration limits appropriately

$$I^{\text{spec}}(\gamma_m) = j \frac{\sqrt{\pi}^3}{\alpha} \frac{1}{k_m} e^{\alpha^2(k_0^2 - \gamma_m^2)} \left[\int_{-\infty}^z e^{-\frac{v^2}{4\alpha^2}} e^{-jk_m(z-v)} dv + \int_z^{+\infty} e^{-\frac{v^2}{4\alpha^2}} e^{jk_m(z-v)} dv \right]. \quad (6.31)$$

By slightly rearranging, one has

$$I^{\text{spec}}(\gamma_m) = j \frac{\sqrt{\pi}^3}{\alpha} \frac{1}{k_m} e^{\alpha^2(k_0^2 - \gamma_m^2)} \left[e^{jk_m z} \int_z^{+\infty} e^{-\frac{v^2}{4\alpha^2}} e^{-jk_m v} dv + e^{-jk_m z} \int_{-\infty}^z e^{-\frac{v^2}{4\alpha^2}} e^{jk_m v} dv \right]. \quad (6.32)$$

Then, for the first integral appearing in (6.32), one obtains

$$\int_z^{+\infty} e^{-\frac{v^2}{4\alpha^2}} e^{-jk_m v} dv = e^{-k_m^2 \alpha^2} \int_z^{+\infty} e^{-\frac{(v+j2\alpha^2 k_m)^2}{4\alpha^2}} dv = \alpha \sqrt{\pi} e^{-k_m^2 \alpha^2} \text{Erfc} \left(\frac{z + j2\alpha^2 k_m}{2\alpha} \right). \quad (6.33)$$

Similarly, the second integral can be expressed as

$$\begin{aligned} \int_{-\infty}^z e^{-\frac{v^2}{4\alpha^2}} e^{jk_m v} dv &= e^{-k_m^2 \alpha^2} \int_{-\infty}^z e^{-\frac{(v-j2\alpha^2 k_m)^2}{4\alpha^2}} dv \\ &= e^{-k_m^2 \alpha^2} \int_{-z}^{+\infty} e^{-\frac{(v+j2\alpha^2 k_m)^2}{4\alpha^2}} dv = \alpha \sqrt{\pi} e^{-k_m^2 \alpha^2} \text{Erfc} \left(\frac{-z + j2\alpha^2 k_m}{2\alpha} \right), \end{aligned} \quad (6.34)$$

where $\text{Erfc}(x)$ is the complementary error function defined as

$$\text{Erfc}(z) = \frac{2}{\sqrt{\pi}} \int_z^{+\infty} e^{-t^2} dt = 1 - \frac{2z}{\sqrt{\pi}} \int_0^1 e^{-(zt)^2} dt. \quad (6.35)$$

By substituting (6.33) and (6.34) into (6.32), eventually results in

$$I^{\text{spec}}(\gamma_m) = j \frac{\pi^2}{k_m} \left[e^{-jk_m z} \text{Erfc} \left(\frac{-z + j2\alpha^2 k_m}{2\alpha} \right) + e^{jk_m z} \text{Erfc} \left(\frac{z + j2\alpha^2 k_m}{2\alpha} \right) \right]. \quad (6.36)$$

Now, to obtain expressions for the dual series of the spectral part of S_0^\pm , one needs to substitute z with $z_{\{i\}} - z_{\{j\}}$ in (6.37). Since (6.37) does not depend on x explicitly, to obtain the series for

$x_{\{i\}} + x_{\{j\}} + 2am$ rather than $x_m = 2am$, the shift property of the Fourier transform needs to be applied, giving

$$S_0^{\pm, \text{spec}} = \frac{1}{2a} \sum_{m=-\infty}^{+\infty} e^{-j\gamma_m(x_{\{i\}} \pm x_{\{j\}})} \frac{1}{k_m} [I_m^{+, \text{spec}} + I_m^{-, \text{spec}}], \quad (6.37)$$

where

$$I_m^{\pm, \text{spec}} = e^{\mp j k_m(z_{\{i\}} - z_{\{j\}})} \text{Erfc} \left(\frac{\mp(z_{\{i\}} - z_{\{j\}}) + j2\alpha^2 k_m}{2\alpha} \right).$$

In order to obtain Schlömilch series of orders other than the zeroth, one can make use of differential operators (6.12) and (6.13), as well as the Leibniz rule in conjunction with the Binomial theorem.

$$\begin{aligned} S_n^{\pm, \text{spec}} &= \frac{(-1)^n}{k_0^n} \left(\frac{\partial}{\partial z_{\{i\}}} + j \frac{\partial}{\partial x_{\{i\}}} \right)^n S_0^{\pm, \text{spec}} = \frac{(-1)^n}{k_0^n} \sum_{l=0}^n C_n^l \frac{\partial^l}{\partial z_{\{i\}}^l} j^{n-l} \frac{\partial^{n-l}}{\partial x_{\{i\}}^{n-l}} S_0^{\pm, \text{spec}} \\ &= \frac{1}{2a} \frac{(-1)^n}{k_0^n} \sum_{m=-\infty}^{+\infty} e^{-j\gamma_m(x_{\{i\}} \pm x_{\{j\}})} \sum_{l=0}^n C_n^l \gamma_m^{n-l} [I_{m,l}^{+, \text{spec}} + I_{m,l}^{-, \text{spec}}], \end{aligned} \quad (6.38)$$

where

C_n^l - the binomial coefficient;

$$I_{m,l}^{\pm, \text{spec}} = \frac{\partial^l I_m^{\pm, \text{spec}}}{\partial z_{\{i\}}^l} = e^{\mp j k_m(z_{\{i\}} - z_{\{j\}})} \sum_{k=0}^l C_l^k (\mp j k_m)^{l-k} \frac{\partial^k}{\partial z_{\{i\}}^k} \text{Erfc} \left(\frac{\mp(z_{\{i\}} - z_{\{j\}}) + j2\alpha^2 k_m}{2\alpha} \right).$$

6.1.5 Evaluation of the Spatial Series Terms

Now, consider the spatial part of (6.20). By changing the order of integration, the m -th term of the spatial part of the Schlömilch series becomes.

$$I_m^{\text{spac}} = \int_0^{\alpha^2} e^{t k_0^2} \int_{-\infty}^{+\infty} e^{-t k_x^2} e^{-j k_x x_m} dk_x \int_{-\infty}^{+\infty} e^{-t k_z^2} e^{-j k_z z} dk_z dt \quad (6.39)$$

Since the functions being transformed are, in fact, Gaussian functions, for both Fourier integrals, there exist closed-form expressions

$$\int_{-\infty}^{+\infty} e^{-t k_x^2} e^{-j k_x x_m} dk_x = \sqrt{\frac{\pi}{t}} e^{-\frac{x_m^2}{4t}} \quad (6.40)$$

and

$$\int_{-\infty}^{+\infty} e^{-t k_z^2} e^{-j k_z z} dk_z = \sqrt{\frac{\pi}{t}} e^{-\frac{z^2}{4t}} \quad (6.41)$$

In view of (6.40) and (6.41), (6.39) can be written as

$$I_m^{\text{spac}} = \pi \int_0^{\alpha^2} \frac{1}{t} e^{tk_0^2} e^{-\frac{1}{4t}(x_m^2+z^2)} dt = \pi \int_{1/\alpha^2}^{+\infty} \frac{1}{t} e^{\frac{k_0^2}{t}} e^{-0.25t(x_m^2+z^2)} dt. \quad (6.42)$$

The second integral in (6.42) is obtained by making substitution $t \rightarrow \frac{1}{t}$. To make the notation more compact write u_m for $(x_m^2 + z^2)/(4\alpha^2)$. Also, for convenience the substitution $t \rightarrow t/\alpha^2$ is made, giving

$$S^{\text{spac}} = \pi \sum_{m=-\infty}^{+\infty} I_m^{\text{spac}} = \pi \sum_{m=-\infty}^{+\infty} \int_1^{\infty} \frac{1}{t} e^{\frac{k_0^2 \alpha^2}{t}} e^{-tu_m} dt. \quad (6.43)$$

For the positive orders, the corresponding Schlömilch series term expressions can be derived by means of the order raising operator (see [103]) as follows

$$S_n^{\text{spac}} = \pi \sum_{m=-\infty}^{+\infty} \frac{(-1)^n}{k_0^n} \left(\frac{\partial}{\partial z} + j \frac{\partial}{\partial x_m} \right)^n \int_1^{\infty} \frac{1}{t} e^{\frac{k_0^2 \alpha^2}{t}} e^{-tu_m} dt \quad (6.44)$$

$$= \pi \sum_{m=-\infty}^{+\infty} \frac{1}{(2\alpha^2 k_0)^n} (z + jx_m)^n \int_1^{\infty} \frac{1}{t^{1-n}} e^{\frac{k_0^2 \alpha^2}{t}} e^{-tu_m} dt. \quad (6.45)$$

Although the integral cannot be evaluated in closed form, one can expand the first exponential factor in (6.45) into a Taylor series around 0. Thus, by letting $\alpha^2 = \bar{\alpha}/k_0^2$, expanding (6.45) into a Taylor series about 0 and truncating it, (6.45) becomes

$$S_n^{\text{spac}} = \pi \sum_{m=-\infty}^{+\infty} \left[\frac{k_0(z + jx_m)}{2\bar{\alpha}} \right]^n \int_1^{\infty} \frac{1}{t^{1-n}} \sum_{p=0}^P \frac{\bar{\alpha}^p}{t^p p!} e^{-tu_m} dt. \quad (6.46)$$

It can be shown by using the integration by parts that the exponential integral of the n -th order can be expressed in terms of the 0-th order exponential integral and some simple algebraic functions. Additionally, it turns out that the number of terms retained in the power series can be reduced while preserving the same accuracy by expanding (6.48) into a Taylor series about 0.5 rather than 0. Of course, it comes at the cost of the increased complexity of mathematical expressions. Hence, by expanding the exponential function around 0.5, not 0, one arrives at

$$S_n^{\text{spac}} = \pi \sum_{m=-\infty}^{+\infty} \left[\frac{k_0(z + jx_m)}{2\bar{\alpha}} \right]^n \int_1^{\infty} \frac{1}{t^{1-n}} e^{0.5} \sum_{p=0}^P \frac{1}{p!} \left(\frac{\bar{\alpha}}{t} - 0.5 \right)^p e^{-tu_m} dt. \quad (6.47)$$

Now, interchanging the order of the summation and the integration yields a series of exponential integrals of different orders. The exponential integral function for non-zero real values of the

argument, x , is defined as

$$\text{Ei}(x) = \int_1^{\infty} \frac{e^{-xt}}{t} dt. \quad (6.48)$$

The definition of the exponential integral can be generalized to powers of t other than -1 . The most commonly encountered in the literature definition is the following one

$$\text{Ei}_n(x) = \int_1^{\infty} \frac{e^{-xt}}{t^n} dt. \quad (6.49)$$

The integral function is termed the exponential integral of n -th order. There exist straightforward recurrence relations relating these functions of orders differing by one. Similar to cylindrical functions, the recurrence relations allow for efficient computation of the expressions involving functions of different orders. The recurrence relation can be easily derived by applying integration by parts to (6.49), giving

$$\text{Ei}_n(x) = \frac{1}{x}e^{-x} - \frac{n}{x}\text{Ei}_{n+1}(x), \quad (6.50)$$

and the equivalent backward recurrence relation is as follows

$$\text{Ei}_{n+1}(x) = \frac{1}{n}e^{-x} - \frac{x}{n}\text{Ei}_n(x), \quad (6.51)$$

Thus, for $n = 1$, the generalized exponential integral can be written as

$$\text{Ei}_1(x) = \sum_{m=0}^{\infty} \frac{(-1)^m m!}{x^{m+1}}. \quad (6.52)$$

Unfortunately, this inverse power series representation converges slowly for $x < 10$, and the presence of the factorial in the numerator of terms causes overflow when computed using floating point arithmetics. Nevertheless, it is possible to rewrite the series in terms of a continued fraction that converges much quicker than the series it is derived from

$$\text{Ei}_1(x) = \frac{e^{-x}}{x + \frac{1}{1 + \frac{1}{x + \frac{2}{1 + \dots}}}}. \quad (6.53)$$

For small values of x , the conventional power series expansion is used, which converges very quickly. Using the definition of the generalized exponential integral of the n -th order, one has

the following identity

$$\int_1^{+\infty} \frac{e^{-t u_m^2}}{t^n} dt = \text{Ei}_n(u_m^2 k_0^2), \quad (6.54)$$

In order to simplify (6.47), Newton's binomial formula can be applied to the p -th term of the summation in the integrand resulting in

$$\frac{(\bar{\alpha} - 0.5t)^p}{t^{p-n+1}} = \frac{\sum_{l=0}^p \mathbf{C}_p^l \bar{\alpha}^{p-l} (-0.5)^l t^l}{t^{p-n+1}} = \sum_{l=0}^p \frac{\mathbf{C}_p^l \bar{\alpha}^{p-l} (-0.5)^l}{t^{p-n+1-l}}. \quad (6.55)$$

Thus,

$$S_n^{\text{spac}} = e^{0.5} \pi \sum_{m=-\infty}^{+\infty} \left[\frac{k_0(z + jx_m)}{2\bar{\alpha}} \right]^n \int_1^{\infty} \sum_{p=0}^P \frac{1}{p!} \sum_{l=0}^p \bar{\alpha}^{p-l} (-0.5)^l \mathbf{C}_p^l \frac{e^{-tu_m}}{t^{p-n-l+1}} dt \quad (6.56)$$

By interchanging integration and summation, (6.56) becomes

$$S_n^{\text{spac}} = \pi \sqrt{e} \sum_{m=-\infty}^{+\infty} \left[\frac{k_0(z + jx_m)}{2\bar{\alpha}} \right]^n \sum_{p=0}^P \sum_{l=0}^p \frac{1}{p!} \mathbf{C}_p^l \bar{\alpha}^{p-l} (-0.5)^l \int_1^{\infty} \frac{e^{-tu_m}}{t^{p-n-l+1}} dt, \quad (6.57)$$

and using (6.54), results in

$$S_n^{\text{spac}} = \pi \sqrt{e} \sum_{m=-\infty}^{+\infty} \left[\frac{k_0(z + jx_m)}{2\bar{\alpha}} \right]^n \sum_{p=0}^P \sum_{l=0}^p \frac{1}{p!} \mathbf{C}_p^l \bar{\alpha}^{p-l} (-0.5)^l \text{Ei}_{p-n-l+1}(u_m). \quad (6.58)$$

Expression (6.58) can be further simplified by using the recurrence relations for the generalized exponential integral (6.50) and (6.51), yielding the following finite series

$$\text{Ei}_{n+1}(x) = \sum_{k=0}^{n-1} e^{-x} \left(\frac{(n-k-1)!(-x)^k}{n!} \right) + \frac{(-x)^n}{n!} \text{Ei}(x) \quad (6.59)$$

Now, using (6.59), one eventually obtains

$$S_n^{\text{spac}} = \pi \sqrt{e} \sum_{m=-\infty}^{+\infty} \left[\frac{k_0(z + jx_m)}{2\bar{\alpha}} \right]^n \sum_{p=0}^P \sum_{l=0}^p \frac{1}{p!} \mathbf{C}_p^l \bar{\alpha}^{p-l} (-0.5)^l T_{p-n-l}(u_m), \quad (6.60)$$

where

$$T_n(\hat{u}) = \begin{cases} e^{-\hat{u}} \sum_{k=0}^{n-1} \left[\frac{(n-k-1)!(-\hat{u})^k}{n!} \right] + \frac{(-x)^n}{n!} \text{Ei}(\hat{u}), & \text{if } n > 0 \\ e^{-\hat{u}} \left[\sum_{k=0}^{-n-2} \frac{(-n-1)!}{(-n-k-1)! \hat{u}^{k+1}} + \frac{(-n-1)!}{\hat{u}^{-n}} \right], & \text{if } n < 0 \\ \text{Ei}(\hat{u}), & \text{if } n = 0 \\ e^{-\hat{u}}/\hat{u}, & \text{if } n = -1 \end{cases}$$

The expression for $T_n(\hat{u})$ in the case when $n < 0$, was obtained by repeatedly (6.49) integrating by parts until the integral of an exponential function is obtained. Note that for $n < 0$, the expression $T_n(\hat{u})$ does not contain the exponential integral compared to the case when $n > 0$.

As far as the expressions for $S^{+, \text{spac}}$ and $S^{-, \text{spac}}$ are concerned, they can be readily derived from (6.60) by replacing x_m and z with $x_{0, \{i\}} + x_{0, \{j\}} + 2ma$ and $z_{0, \{i\}} - z_{0, \{j\}} + 2ma$, and x_m and z with $x_{0, \{i\}} - x_{0, \{j\}} + 2ma$ and $z_{0, \{i\}} - z_{0, \{j\}} + 2ma$, respectively.

6.1.6 Evaluation of Excitation Vector Entries

The incident dominant mode in the rectangular waveguide is given by

$$E_y^i(x, z) = \sin(\gamma_1 x) e^{-j\tilde{k}_1 z}, \quad (6.61)$$

where

$$\begin{aligned} \gamma_1 &= \pi/a - \text{the transverse wavenumber for the dominant waveguide mode, } 1/m; \\ \tilde{k}_1 &= \sqrt{k_0^2 - \gamma_1^2} - \text{the waveguide wavenumber for the dominant waveguide mode, } 1/m. \end{aligned}$$

Using the well-known Euler's identity, one can rewrite (6.61) in a form which is more convenient for the derivation of the expressions for excitation vector entries

$$E_y^i(x, z) = \frac{1}{2j} (e^{j\gamma_1 x} - e^{-j\gamma_1 x}) e^{-j\tilde{k}_1 z}, \quad (6.62)$$

First, consider the expression for the first term in (6.62). To obtain the entries of the excitation vector, expression (6.61) should be rewritten in terms of local coordinates of the i -th rod

$$E_y^i(x, z) = \frac{1}{2j} e^{j\gamma_1 x} e^{-j\tilde{k}_1 z} = \frac{1}{2j} e^{j\gamma_1 x_{0, \{i\}}} e^{j\gamma_1 r_{\{i, p_i\}} \sin \varphi_{\{i\}}} e^{-j\tilde{k}_1 z_{0, \{i\}}} e^{-j\tilde{k}_1 r_{\{i, p_i\}} \cos \varphi_{\{i\}}}. \quad (6.63)$$

Then, multiplying the resulting expression by weighting functions and integrating with respect to $\varphi_{\{i\}}$ over the interval $[0, 2\pi]$, as well as making use of the Jacobi-Anger expansion [126], one eventually obtains

$$\begin{aligned} & \frac{1}{2j} \int_0^{2\pi} e^{jn\varphi_i} e^{j\gamma_1 x_{0, \{i\}}} e^{-j\tilde{k}_1 z_{0, \{i\}}} e^{jk_0 r_{\{i, p_i\}} (-\cos \varphi_{\{i\}} \cos \varphi_k + \sin \varphi_{\{i\}} \sin \varphi_k)} r_{\{i, p_i\}} d\varphi_{\{i\}} \\ &= -j\pi (-j)^n r_{\{i, p_i\}} J_n(k_0 r_{\{i, p_i\}}) e^{j\gamma_1 x_{0, \{i\}}} e^{-j\tilde{k}_1 z_{0, \{i\}}} e^{-jn\varphi_k} \end{aligned} \quad (6.64)$$

where

$$\begin{aligned} \varphi_k &= \arctan(\gamma_1 / \tilde{k}_1); \\ \varphi_i &= \arctan((x - x_{0, \{i\}}) / (z - z_{0, \{i\}})). \end{aligned}$$

The expression for the second term in (6.62), can be readily found in a similar way. Combining the expressions and slightly rearranging them, one finally obtains the expression for the

n -th excitation vector coefficient for the i -th rod

$$e_{i,(n+N+1)} = 2\pi r_{\{i,p_i\}} (-j)^n J_n(k_0 r_{\{i,p_i\}}) e^{-j\tilde{k}_1 z_{0,\{i\}}} \sin(\gamma_1 x_{0,\{i\}} + n\varphi_k). \quad (6.65)$$

6.1.7 Numerical Validation

To validate the proposed method, one compares the frequency responses and $|S_{11}|$ as a function of the dielectric constant of two waveguide sections obtained by employing the proposed method (IBIM) and the commercially available software HFSS and CST studio. One of the structures to be considered contains two solid dielectric rods, whereas the other includes two two-layer rods. In the case of a single centrally placed dielectric rod, the results obtained by the proposed method agree well with those obtained by the method outlined in [90], which exhibits very rapid convergence while maintaining reasonably good accuracy of results. For notational simplicity, hereinafter the following dimensionless model parameters are introduced $\tilde{r}_{j_o} = r_{\{j,o\}}/a$, $\tilde{x}_{0j} = x_{0,\{j\}}/a$ and $\tilde{z}_{0,j} = z_{0,\{j\}}/a$.

The values of the first structure parameters are as follows: $\tilde{x}_{01} = 0.3$, $\tilde{x}_{02} = 0.7$, $\tilde{z}_{01} = 0.3$, $\tilde{z}_{02} = 0.1$, $\tilde{r}_{11} = 0.15$, $\tilde{r}_{21} = 0.2$, and $\varepsilon_{r21} = 5$. The parameter values of the second structure are as follows: $\tilde{x}_{01} = 0.3$, $\tilde{x}_{02} = 0.7$, $\tilde{z}_{01} = 0.3$, $\tilde{z}_{02} = 0.1$, $\tilde{r}_{11} = 0.05$, $\tilde{r}_{12} = 0.12$, $\tilde{r}_{21} = 0.1$, $\tilde{r}_{22} = 0.2$, $\varepsilon_{r12} = 5$, $\varepsilon_{r21} = 10$, and $\varepsilon_{r22} = 5$.

The scattering data ($|S_{11}|$ and $|S_{21}|$) for the first of the examined structures calculated at 1000 different values of the dielectric constant of the first rod is shown in Fig. 6.2, whereas the scattering data ($|S_{11}|$ and $|S_{21}|$) for the second structure calculated at 1000 different values of the dielectric constant of the outer layer of the first rod is shown in Fig. 6.3. In both cases, a/λ was set equal to 0.73.

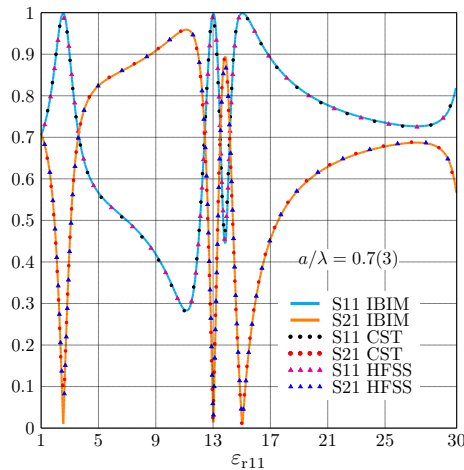


Fig. 6.2. $|S_{11}|$ and $|S_{21}|$ as a function of ε_{r11} . Two solid dielectric rods. [131]

The frequency responses of the first and second structures are displayed in Fig. 6.4 and

Fig. 6.5, respectively. The parameters of both structures are the same as before except that ϵ_{r11} and ϵ_{r12} were set to 10 for the single rod and the double rod structures, respectively.

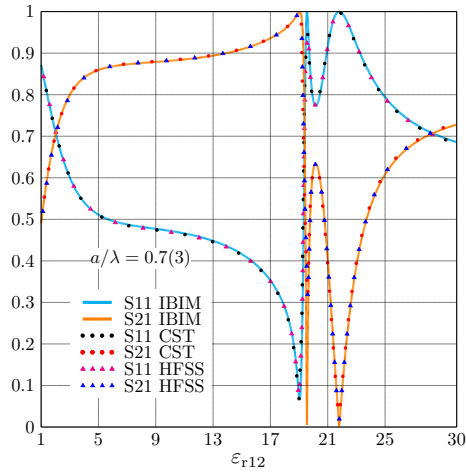


Fig. 6.3. $|S_{11}|$ and $|S_{21}|$ against ϵ_{r12} . Two two-layered dielectric rods. [131]

The frequency responses obtained by means of Ansys HFSS are computed using the fast broadband frequency sweep, which is based on the Adaptive Lanczos-Pade Approximation. The number of test and trial functions used to approximate fields in the IBIM was 11. Overall, the results obtained by the IBIM are in excellent agreement with the ones computed by using Ansys HFSS, but the IBIM significantly outperforms Ansys HFSS.

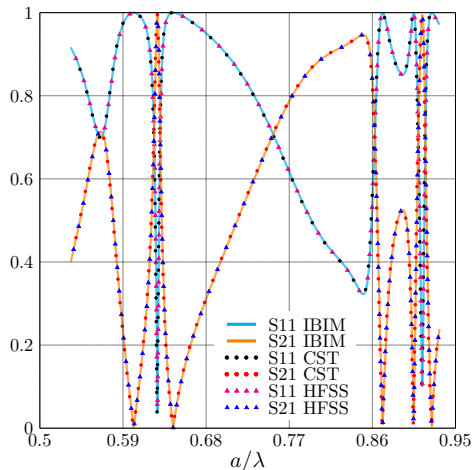


Fig. 6.4. $|S_{11}|$ and $|S_{21}|$ as a function of a/λ . Two solid dielectric rods. [131]

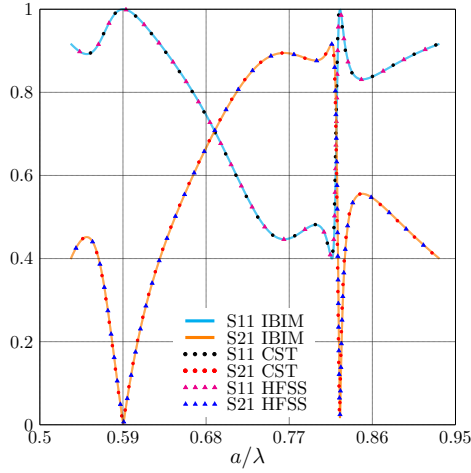


Fig. 6.5. $|S_{11}|$ and $|S_{21}|$ as a function of a/λ . Two two-layered dielectric rods. [131]

To further verify the method, $|S_{11}|$ was calculated for the structure shown in Fig. 6.6. The calculation results are shown in Fig. 6.7, and the calculation times are summarized in Table 6.1. The parameters of the structure are presented in Table 6.2, and the number of test and trial functions used to approximate fields in the IBIM was 11.

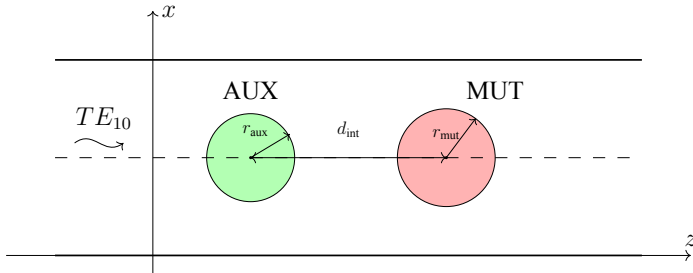


Fig. 6.6. Two dielectric rods in a rectangular waveguide.

Table 6.1

Comparison of computation times

Model Parameter	Symbol
Method	Time s
IBIM	8.2
Ansys HFSS	824.6

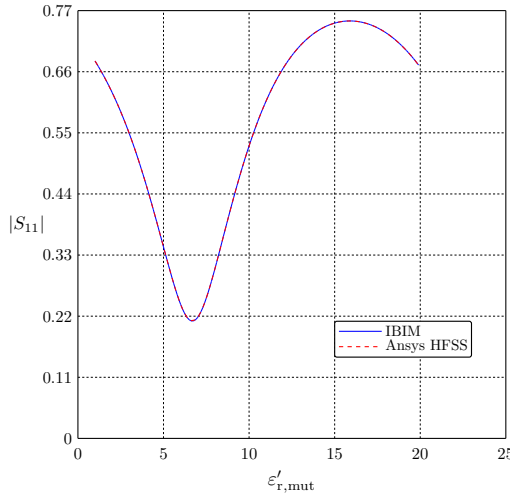


Fig. 6.7. $|S_{11}|$ as a function of $\epsilon'_{r,\text{mut}}$, calculated using the IBIM and HFSS.

Table 6.2

Parameters of the two-rod model		
Model Parameter	Symbol	Value
MUT dielectric constant	$\epsilon'_{r,\text{mut}}$	10.2
MUT loss tangent	$\tan \delta_{\text{mut}}$	0.0023
Dielectric constant of the auxiliary rod	$\epsilon'_{r,\text{aux}}$	4.3
Auxiliary rod loss tangent	$\tan \delta_{\text{aux}}$	0.003
MUT rod radius	r_{mut}	2.5 mm
The radius of the auxiliary rod	d_{aux}	5.7 mm
Interrod distance	r_{int}	8.6 mm
Frequency	f	10 GHz
Waveguide width	a	22.86 mm

6.1.8 Extended Boundary Integral Equation Method

In this section, the extended version of the Improved Boundary Integral Equation Method (IBIM) to handle structures comprising a number of dielectric rods in a rectangular waveguide is employed [128]. The method is also described in one of the papers [129] written by the author during the development of the thesis. This chapter is concerned with a measurement model composed of two dielectric rods located in a rectangular waveguide. One of the rods is made of MUT, whereas the other one is intended to improve the classical single-rod models treated in chapter 1.

The presence of holes or, in the general case, cylindrical dielectric inclusion in an otherwise solid rod give rise to rotational asymmetry, which might be exploited to introduce slight varia-

tions to the S_{11} by rotating the rod around their axes, thereby making slight adjustments of the corresponding measurement curve.

In addition, this kind of structure may be utilized in non-destructive measurements of dispersive dielectric dielectric constant. The measurement procedure, in this case, consists in placing the sample under test (with the dielectric constant to be determined) in (a) hole(s) of the rod. Then, multiple measurements required to find a unique value of the dielectric constant are achieved by making measurements at different rotation angles.

The surface integral equation describing the interaction of electromagnetic waves with the structure is derived in the same manner as the one for the multi-layered structure treated in the previous section.

6.1.9 Formulation

One of the structures for which the method is developed is depicted in Fig. 6.8. Again, it is assumed that only the dominant TE_{10} mode can propagate in the waveguide. The incident wave is the dominant waveguide mode (TE_{10} mode) propagating along the z axis with the electric field component along the y -axis given by

$$E^i(x, z) = \sin(\gamma_1 x) \cdot e^{-jk_z z}. \quad (6.66)$$

Since the cross-sections of rods and the distribution of the fields due to the incident wave are uniform along the y axis, the problem can be solved in two dimensions, thus significantly simplifying the analysis. In order to simplify the derivation process, define local coordinates for all cylindrical regions as shown in Fig. 6.9. The local coordinate systems are defined such that the origin of the coordinate system associated with a cylindrical region coincides with the center of the region. The number of rods is denoted by N , and the number of cylindrical inclusions in the i -th rod is denoted by N_i . For convenience, separate numbering is used for rods, as well as internal homogeneous regions (inclusions) inside different rods.

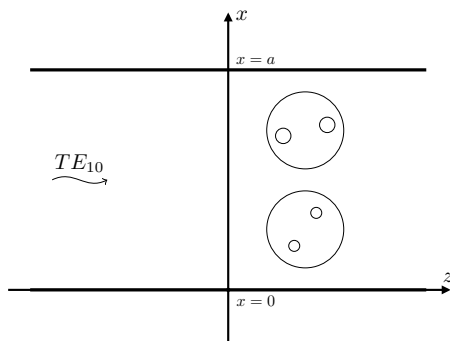


Fig. 6.8. The geometry of the problem. [129]

To make notation compact, different homogeneous regions are labeled using multi-index

that may be either a single or a pair of indices enclosed in braces. For regions between the outer surface and inner surfaces of rods, a single index is used, e.g., the region between the outer and inner surfaces of the n -th rod is labeled $V_{\{n\}}$. For internal homogeneous regions, two indices are used: the first index corresponds to the rod, whereas the second corresponds to its sub-region. For example, label $V_{\{m,n\}}$ is used for the m -th sub-region of the n -th rod. The region outside cylindrical rods is labeled $V_{\{0\}} = V_0$. The outer surface of region V_α is denoted by ∂V_α . The position vector in the local coordinate system associated with region V_α and the corresponding Cartesian and polar coordinates are denoted by \mathbf{r}_α , x_α , z_α , r_α and φ_α , respectively. The position vector of the origin of the local coordinate system for cylindrical region V_α is denoted by $\mathbf{r}_{0,\alpha}$, while $x_{0,\alpha}$ and $z_{0,\alpha}$ represent the global x and z coordinates of the local system origin, respectively, and $r_{0,\alpha}$ refers to the radius of cylindrical region V_α . For the entire surface of region V_α , the symbol Ω_α is used.

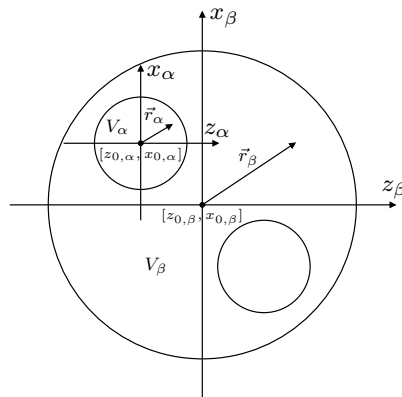


Fig. 6.9. Local coordinate systems of rods and their inclusions. [129]

Also, for the sake of compactness, the following two integral operators are introduced

$$\mathcal{L}_{i,\beta}^\alpha u(\mathbf{r}_s) = \oint_{\partial V_\beta} u(\mathbf{r}_s) \frac{\partial G_i^\alpha(\mathbf{r}_o, \mathbf{r}_s)}{\partial n} dl_s \quad (6.67)$$

$$\mathcal{K}_{i,\beta}^\alpha u(\mathbf{r}_o) = jZ_\alpha k_\alpha \oint_{\partial V_\beta} u(\mathbf{r}_s) G_i^\alpha(\mathbf{r}_o, \mathbf{r}_s) dl_s, \quad (6.68)$$

where the normal derivative in (6.67) is taken in the direction of outward pointing normal vector and \mathbf{r}_o and \mathbf{r}_s are position vectors of observation and source points, respectively.

The first lower index takes only two values $i = 1, 2$. For $i = 1$, the Green's function is given by

$$G_1^\alpha(\mathbf{r}_o, \mathbf{r}_s) = \frac{j}{4} \sum_{n=-\infty}^{+\infty} \left(H_0^{(2)}(k_\alpha r_n^-) - H_0^{(2)}(k_\alpha r_n^+) \right), \quad (6.69)$$

where

$r_n^\pm = \sqrt{(x_0 \pm x_s + 2an)^2 + (z_0 - z_s)^2}$ - the distance between the n -th image of the source point and the observation point, m.

This Green's function is known as the waveguide Green's function as it satisfies PEC boundary conditions on the walls of the waveguide.

For $i = 2$, Green's function is given by

$$G_2^\alpha(\mathbf{r}_o, \mathbf{r}_s) = \frac{j}{4} H_0^{(2)}(k_\alpha r_0^-). \quad (6.70)$$

The integral relation between the electric field at a point outside of the rods, i.e., $\mathbf{r}_o \in V_{\{0\}}$, and the fields on the boundary of the region is as follows

$$E^i(\mathbf{r}_o) = E(\mathbf{r}_o) - \sum_{n=1}^N \left[\mathcal{L}_{1,\{n\}}^{\{0\}} E(\mathbf{r}_s) + \mathcal{K}_{1,\{n\}}^{\{0\}} H(\mathbf{r}_s) \right], \quad (6.71)$$

where $\mathbf{r}_o \in V_{\{0\}}$, $E^i(\mathbf{r}_o)$ is the incident field, $E(\mathbf{r}_o)$ and $H(\mathbf{r}_o)$ are the total electric and magnetic fields, respectively.

Similar relations exist for the other regions, as well. The integral relation for $V_{\{n\}}$ and $\mathbf{r}_o \notin V_{\{n\}}$ is

$$\begin{aligned} & \mathcal{L}_{2,\{n\}}^{\{n\}} E(\mathbf{r}_s) + \mathcal{K}_{2,\{n\}}^{\{n\}} H(\mathbf{r}_s) = \\ & \sum_{n=1}^{N_n} \left[\mathcal{L}_{2,\{n,m\}}^{\{n\}} E(\mathbf{r}_s) + \mathcal{K}_{2,\{n,m\}}^{\{n\}} H(\mathbf{r}_s) \right]. \end{aligned} \quad (6.72)$$

For the m -th inclusion of n -th rod and $\mathbf{r}_o \notin V_{\{n,m\}}$, one has

$$0 = \mathcal{L}_{2,\{n,m\}}^{\{n,m\}} E(\mathbf{r}_s) + \mathcal{K}_{2,\{n,m\}}^{\{n,m\}} H(\mathbf{r}_s). \quad (6.73)$$

To obtain a set of integral equations for the unknown fields on all surfaces of homogeneous regions (6.71) is used, and integral relations (6.72), (6.73) are written for all the regions. Furthermore, the observation point is restricted, \mathbf{r}_o , to the surfaces of the regions (entire surfaces), e.g., for region V_β one must have $\mathbf{r}_o \in \Omega_\beta$.

The next step is to convert each of the integral equations to a set of linear algebraic equations. To that end, the fields on each surface are approximated in terms of finite series of basis functions with unknown expansion coefficients. More precisely, the electric and magnetic fields on ∂V_β are approximated as

$$E_\beta(\varphi_\beta) = \sum_{i=-M}^M E_{i,\beta} e^{i\varphi_\beta}, \quad (6.74)$$

and

$$H_\beta(\varphi_\beta) = \sum_{i=-M}^M H_{i,\beta} e^{i\varphi_\beta}, \quad (6.75)$$

respectively, where $N_B = 2M + 1$ is the number of basis functions.

The Galerkin method is used to discretize the above integral equations to obtain the system of linear algebraic equations to be solved for the field expansion coefficients. In the Galerkin method, the weighting functions are identical to the basis functions used to approximate the fields on ∂V_α . The Galerkin method requires the evaluation of the inner product for all the possible pairs of basis and weighting functions, where the inner product of any two square integrable functions $u(\mathbf{r}_o)$ and $v(\mathbf{r}_o)$ for surface ∂V_α is defined as

$$(u, v)_\alpha = \oint_{\partial V_\alpha} u(\mathbf{r}_o) \cdot v^*(\mathbf{r}_o) dl_o. \quad (6.76)$$

Now, substituting (6.74) and (6.75) for the electric and magnetic fields, respectively, in the equation for region V_γ and applying the Galerkin procedure to surface $\partial V_\alpha \in \Omega_\gamma$ yields

$$e_n^{\alpha,\beta,\gamma} = (E^i(\mathbf{r}_o), e^{jm\varphi_\alpha})_\alpha \quad (6.77)$$

$$l_{n,m}^{\alpha,\beta,\gamma} = (\mathcal{L}_{i,\beta}^\gamma e^{jm\varphi_\beta}, e^{jm\varphi_\alpha})_\alpha \quad (6.78)$$

$$k_{n,m}^{\alpha,\beta,\gamma} = (\mathcal{K}_{i,\beta}^\gamma e^{jm\varphi_\beta}, e^{jm\varphi_\alpha})_\alpha, \quad (6.79)$$

where

$$\partial V_\beta \in \Omega_\beta.$$

In (6.77) through (6.79) $i = 2$ for $\gamma \neq 0$ and $i = 1$ otherwise. Combining equations for all the surfaces yields the resulting equation system, which is solved using a plain solver using the LU factorization. Once the expansion coefficients are found, one can easily determine the elements of the scattering matrix (scattering data) in the same manner as in the case of multiple multi-layered rods.

Graf's addition theorem is utilized to evaluate the matrix entries, which can be accomplished analytically. Thus, Green's function can be written in terms of a series of functions of local coordinates associated with surfaces ∂V_α and ∂V_β only.

$$H_0^{(2)}(k_\gamma|\mathbf{r}_d|) = \sum_{m,n=-\infty}^{+\infty} Z_{m-n}^{\gamma,+}(\mathbf{r}_{\alpha,\beta}) Z_n^{\gamma,+}(\mathbf{r}_\alpha) Z_m^{\gamma,-}(\mathbf{r}_\beta), \quad (6.80)$$

where

$$\mathbf{r}_d = \mathbf{r}_o - \mathbf{r}_s = \mathbf{r}_\alpha - \mathbf{r}_\beta + \mathbf{r}_{\alpha,\beta};$$

$$\mathbf{r}_{\alpha,\beta} = \mathbf{r}_{0,\alpha} - \mathbf{r}_{0,\beta};$$

$$Z_i^{\beta,\pm}(\mathbf{r}_\alpha) = Q_i(k_\beta r_\alpha) \cdot e^{\pm j i \varphi_\alpha};$$

$Q_i(x)$ - is either the i -th order Bessel function $J_i(x)$, or the i -th order Hankel function of the second kind $H_i^{(2)}(x)$ (the latter is used for the largest of r_α , r_β and $r_{\alpha,\beta}$).

Now, substituting (6.80) into (6.78) and (6.79) and integrating, one has

$$\begin{aligned} l_{n,m}^{\alpha,\beta,\gamma} &= -j k_\gamma I_\alpha I_\beta \cdot S_{m-n}^{\alpha,\beta,\gamma} \cdot Q_n(\bar{R}_\alpha^\gamma) \cdot Q_m^{(1)}(\bar{R}_\beta^\gamma) \\ k_{n,m}^{\alpha,\beta,\gamma} &= Z_\gamma k_\gamma I_\alpha I_\beta \cdot S_{m-n}^{\alpha,\beta,\gamma} \cdot Q_n(\bar{R}_\alpha^\gamma) \cdot Q_m(\bar{R}_\beta^\gamma), \end{aligned} \quad (6.81)$$

where

$$\begin{aligned} I_\alpha &= \pi R_\alpha, \bar{R}_\beta^\alpha = k_\alpha R_\beta; \\ S_i^{\alpha,\beta,\gamma} &= Q_i(k_\gamma R_{\alpha,\beta}) \cdot e^{j i \varphi_{\alpha,\beta}} \text{ for } \beta \neq 0; \\ R_{\alpha,\beta} \text{ and } \varphi_{\alpha,\beta} &- \text{ the polar coordinates of vector } \mathbf{r}_{\alpha,\beta}. \end{aligned}$$

Since in case of $\gamma = 0$ the waveguide Green's function is used in place of the free space one

$$S_p^{\alpha,\beta,\gamma} = S_{p,-}^{\alpha,\beta,\gamma} - S_{p,+}^{\alpha,\beta,\gamma}, \quad (6.82)$$

where

$$\begin{aligned} S_{p,\pm}^{\alpha,\beta,\gamma} &= \sum_{l=-\infty}^{+\infty} H_p^{(0)}(k_\gamma r_{l,\alpha,\beta}^\pm) e^{j i \varphi_{l,\alpha,\beta}^\pm}; \\ r_{l,\alpha,\beta}^\pm \text{ and } \varphi_{l,\alpha,\beta}^\pm &- \text{ the polar coordinates of vectors } \mathbf{r}_{l,\alpha,\beta}^+ = \mathbf{r}_{0,\alpha} - \mathbf{r}_{0,\beta} + 2l\mathbf{a} \cdot \mathbf{e}_x \text{ and} \\ \mathbf{r}_{l,\alpha,\beta}^- &= \mathbf{r}_{0,\alpha} - \mathbf{r}_{0,\beta}^* + 2l\mathbf{a} \cdot \mathbf{e}_x; \\ \mathbf{r}_{0,\beta}^* &- \text{ the mirror image of } \mathbf{r}_{0,\beta} \text{ with respect to the } z \text{ axis.} \end{aligned}$$

Unfortunately, the direct evaluation of series (6.82) leads to requires an exceedingly large CPU time unless some series acceleration techniques are employed. Similar to the case of multilayered rod configurations, this issue can be appreciably mitigated via the use of Ewald's summation technique.

Using Ewald's summation technique to speed-up the evaluation of series (6.82) results in the following over-determined equation system

$$\mathbf{Z}^H \mathbf{h} + (\mathbf{I} - \mathbf{Z}^E) \mathbf{e} = \mathbf{i}, \quad (6.83)$$

To calculate the excitation vector entries, one needs to evaluate the surface integral of the product of each weighting function and the function representing the electric field of the incident mode over the surface of the n -th rod. To that end, first rewrite expression (6.66) in terms of local coordinates associated with the n -th rod, whose origin coincides with the axis of the rod

$$E^i(x, z) = e^{-j \bar{k}_{z1}(z_{0,\{n\}} + r_{0,\{n\}} \cos \varphi_{\{n\}})} \frac{1}{2j} \left(e^{j \gamma_1(x_{0,\{n\}} + r_{0,\{n\}} \sin \varphi_{\{n\}})} - e^{-j \gamma_1(x_{0,\{n\}} + r_{0,\{n\}} \sin \varphi_{\{n\}})} \right), \quad (6.84)$$

where

$$\varphi_k = \arctan \left(\sqrt{(k_0 a / \pi)^2 - 1} \right).$$

The $(i+M+1)$ -th entry of the n -th subvector of excitation vector \mathbf{i} , $\mathbf{i}_{\{n\}}$, can be readily found by multiplying the right-hand side of (6.84) by $e^{-ji\varphi_{\{n\}}}$ and performing integration with respect to $\varphi_{\{n\}}$ using the Jacobi-Anger expansion for the exponential function. The resulting expression is identical to (6.65), which was derived for the multilayered rod configuration, except that in this case different notation for the local coordinates associated with rods is used.

Then, to find the relations between the tangential components of the magnetic and electric fields on the surface the m -th subregion of the n -th rod, the fields inside the subregion are expressed in terms of cylindrical functions. As the electric field in the m -th subregion of the n -th rod satisfies the homogeneous Helmholtz equation, the electric field inside it may be expressed as

$$E_{\{m,n\}}(r_{\{m,n\}}, \varphi_{\{m,n\}}) = \sum_{l=-\infty}^{+\infty} A_{l,\{m,n\}} J_n(k_{\{m,n\}} r_{\{m,n\}}) e^{jn\varphi_{\{m,n\}}}. \quad (6.85)$$

The corresponding expansion for the magnetic field inside the m -th cylindrical subregion of the n -th rod can be found by using the second Maxwell's equation and (6.85) as follows

$$H_{\{m,n\}}(r_{\{m,n\}}, \varphi_{\{m,n\}}) = -\frac{1}{jZ_{\{m,n\}}} \sum_{l=-\infty}^{+\infty} A_{l,\{m,n\}} J_n(k_{\{m,n\}} r_{\{m,n\}}) e^{jn\varphi_{\{m,n\}}}, \quad (6.86)$$

where

$Z_{\{m,n\}}$ - the intrinsic impedance of m -th cylindrical subregion of the n -th dielectric rod.

Now, using (6.85) and (6.86), as well as exploiting the orthogonality of both series with respect to $\varphi_{\{m,n\}}$ to eliminate unknown expansion coefficients $A_{l,\{m,n\}}$, one obtains the following relation between the l -th field approximation coefficients $E_{l,\{m,n\}}$ and $H_{l,\{m,n\}}$ for the surface of the n -th cylindrical subregion of the m -th rod

$$H_{l,\{m,n\}} = D_{l,\{m,n\}} E_{l,\{m,n\}} \quad (6.87)$$

where

$D_{l,\{m,n\}}$ - the l -th diagonal entry of a diagonal matrix $\mathbf{D}_{\{m,n\}}$.

Using relation (6.87), as well as (6.83), one can obtain the following relation between subvectors of \mathbf{e} and \mathbf{h} for each internal cylindrical subregion to reduce the number of unknowns and therefore the size of the resulting equation system to be solved for the unknown field expansion coefficients. For example, for the m -th subregion of the n -th rod the submatrices in (6.83)

become related as follows

$$\mathbf{h}_{\{m,n\}} = -\frac{1}{jZ_{\{m,n\}}k_{\{m,n\}}} \mathbf{D}_{\{m,n\}}^{-1} (\mathbf{Z}_{\{m,n\}}^{\text{H}})^{-1} (\mathbf{I} - \mathbf{Z}_{\{m,n\}}^{\text{E}}) \mathbf{e}_{\{m,n\}} \quad (6.88)$$

Substituting (6.88) into (6.83) and solving the resulting equation system for the unknown expansion coefficients, then substituting them into (6.66) and integrating using the Jacobi-Anger expansion yields the following expressions for S_{11}

$$S_{11} = \sum_{n=1}^N \sum_{l=-M}^M (-1)^l \tilde{C}_{l,\{n\}} \sin(\gamma_1 x_{0,\{n\}} + l\varphi_k) e^{j\tilde{k}_{z1} z_{0,\{n\}}}, \quad (6.89)$$

and S_{21}

$$S_{22} = \sum_{n=1}^N \sum_{l=-M}^M \tilde{C}_{l,\{n\}} \sin(\gamma_1 x_{0,\{n\}} - l\varphi_k) e^{-j\tilde{k}_{z1} z_{0,\{n\}}}, \quad (6.90)$$

where

$$\tilde{C}_{l,\{n\}} = \frac{(-j)^{(l-1)} 2\pi k_0 r_{0,\{n\}}}{a \tilde{k}_{z1}} [Z_{\{j\}} H_{l,\{j\}} J_l(k_0 r_{0,\{n\}}) - E_{l,\{n\}} J_l(k_0 r_{0,\{n\}})].$$

6.1.10 Numerical Verification

To verify the proposed method, the scattering parameters of two structures containing single and two dielectric rods with inclusions were calculated using the proposed method and Ansys HFSS. To make the notation more compact, dimensionless parameters are introduced to describe the model under consideration. Namely, in place of the radius of the i -th rod the following dimensionless quantity is used $\tilde{r}_{\{i\}} = r_{\{i\}}/a$. To distinguish relative quantities, they are indicated using a tilde over the respective symbols.

The first of two examined structures is a single rod with two identical circular holes located symmetrically relative to its axis (see Fig. 6.10).

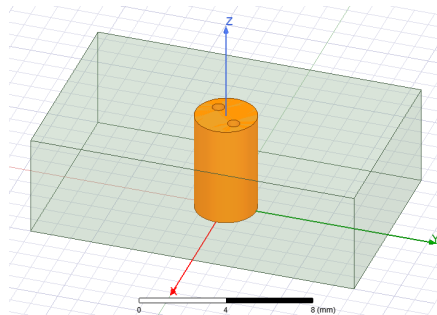


Fig. 6.10. Single dielectric rod with two identical holes (HFSS model). [129]

The dielectric constant of the rod with the relative radius $\tilde{r}_{\{1\}} = 1.5$ are $\varepsilon_{r,\{1\}} = 12.6$. The

relative distance between the centers of two cylindrical holes was $\tilde{d}_{\{1\}} = 0.16$, the radii of holes were $\tilde{r}_{\{1,1\}} = 0.03$ and $\tilde{r}_{\{1,2\}} = 0.03$, respectively. The rod was located midway between the walls of the waveguide, i.e., $\tilde{x}_{o,\{1\}} = 0.5$ and is rotated by an angle $\varphi_{r,\{1\}} = 45^\circ$. The scattering data was computed at 1000 different values of a/λ_0 . As can be seen in Fig. 6.11 the $|S_{11}|$ calculated with the proposed method is in good agreement with that computed by means of Ansys HFSS. The CPU time required by the proposed method and Ansys HFSS are 3 s and 825 s, respectively.

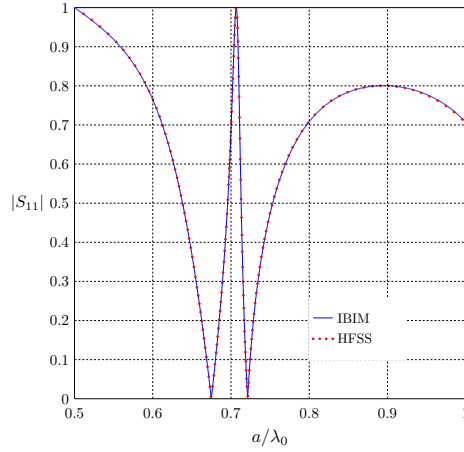


Fig. 6.11. $|S_{11}|$ calculated for the single rod model as a function of a/λ_0 . [129]

The second of the examined structures comprises two rods, each having two cylindrical holes with equal radii, as illustrated Fig. 6.12.

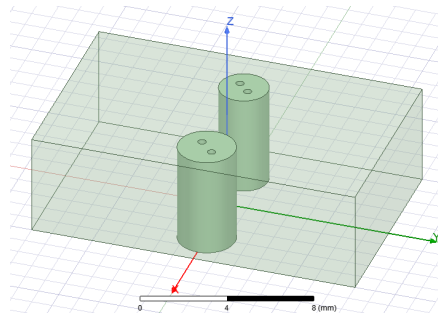


Fig. 6.12. Two dielectric rods with two identical holes (HFSS model). [129]

The dielectric constants of the rods are $\varepsilon_{r,\{1\}} = 12.6$ and $\varepsilon_{r,\{2\}} = 23.7$, respectively. The first rod with radius $\tilde{r}_{\{1\}} = 0.14$ was located at $\tilde{x}_{o,\{1\}} = 0.8$, while the second rod had the radius $\tilde{r}_{\{2\}} = 0.12$ and was located at $\tilde{x}_{o,\{2\}} = 0.25$. The relative distance between the centers of two cylindrical holes was $\tilde{d}_{\{1\}} = \tilde{d}_{\{2\}} = 0.05$ and the radii of holes of the first and second rods

are $\tilde{r}_{\{1,1\}} = \tilde{r}_{\{1,2\}} = 0.05$ and $\tilde{r}_{\{2,1\}} = \tilde{r}_{\{2,2\}} = 0.04$, respectively. Both rods are rotated by $\varphi_{\text{rot},\{1\}} = \varphi_{\text{rot},\{2\}} = 45^\circ$.

The scattering data were computed for 1000 different values of a/λ_0 . The calculated $|S_{11}|$ is plotted in Fig. 6.13 as a function of a/λ_0 .

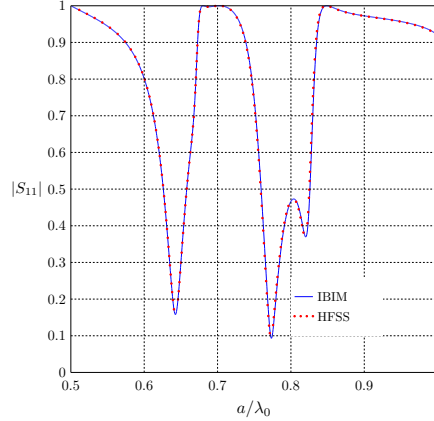


Fig. 6.13. $|S_{11}|$ calculated for the single rod model as a function of a/λ_0 . [129]

The calculated $|S_{21}|$ at different values of a/λ_0 is displayed in Fig. 6.14. The scattering data computed employing the proposed method are in excellent agreement with those obtained using Ansys HFSS. In contrast, the computation time of the proposed method is much shorter (5 s) than that of HFSS (1215 s). The phase was measured from the reference planes at the origin of the global coordinate system.

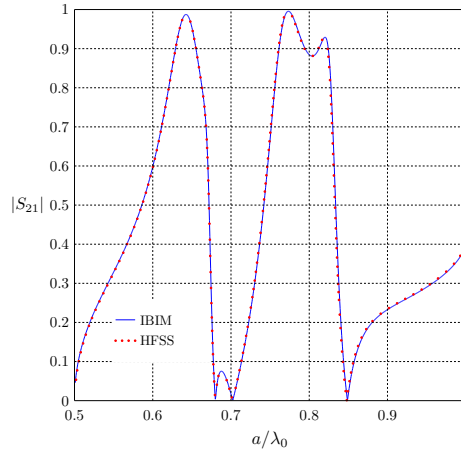


Fig. 6.14. $|S_{21}|$ calculated for the single rod model as a function of a/λ_0 . [129]

However, as can be seen in Fig. 6.15 where the phase of S_{21} is shown, there is, however, a

small discrepancy between the results, which arises due to an increase in the ratio of the average element size to the wavelength that, in turn, reduces the field approximation accuracy.

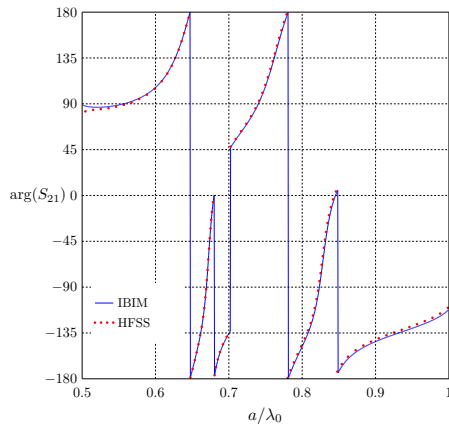


Fig. 6.15. The phase of S_{21} calculated for the double rod model as a function of a/λ_0 . [129]

At the low end, the discrepancy is due to the fact that the adaptive solution frequency in HFSS was chosen to be very close to the highest frequency of the range ($a/\lambda_0 = 0.93$) and an interpolative sweep was employed. In both cases, the number of basis and weighting functions used for each cylindrical surface was $N_B = 11$.

6.2 Summary

A fast integral equation-based method for the scattering parameter calculation of complex structures involving dielectric rods with a single or multiple cylindrical dielectric inclusion(s) or holes (can be viewed as a special case of inclusions) was developed. In contrast to most of its counterparts, it does not require surface partitioning of the object(s) under consideration and performing numerical integration over the subdomains. Instead, the subdomain integrals were evaluated analytically, giving infinite series of cylindrical functions referred to as Schlömilch series or lattice sums. The series exhibit very slow convergence, but it is shown that a considerable speed-up can be achieved with the use of Ewald's summation technique. The accuracy and the CPU time were compared against those obtained by means of commercially available software Ansys HFSS. The outcome of this comparative analysis shows that the method is capable of providing sufficiently high accuracy while being considerably faster than general purpose methods, not exploiting some structural peculiarities of the problem geometry, such as symmetry, etc.

CONCLUSIONS

This thesis is devoted to the evaluation and sensitivity improvement of dielectric permittivity measurement models for high-frequency low-loss dielectric materials. Several of the most widely used dielectric constant measurement models have been investigated: 1) a model where the material under test (MUT) is a dielectric slab in a rectangular waveguide or free space; 2) a model where the MUT is a cylindrical dielectric rod in a waveguide. Both measurement models employ the reflection technique to retrieve dielectric permittivity. The main result of the research is a simple, fast, and convenient measurement model evaluation methodology, which can be applied even when model parameters (MUT dimensions, frequency, as well as the expected value of the dielectric constant) cannot be altered. In the case when the model sensitivity is unacceptably low, and the model parameters are not allowed to be changed, e.g., when it is required by standards or measurements have to be non-destructive or made at a fixed frequency, the author has developed several measurement models employing additional dielectric objects alongside the MUT. To facilitate the construction and calculation of the improved measurement models, the author has developed a number of analytical and numerical approaches. The author has also developed a new numerical method for the analysis of models with a single or multiple circular cylindrical rods in a waveguide, whose use results in an appreciable reduction in the computation time compared to the existing general-purpose numerical methods, which is essential when the measurement uncertainty is estimated with the use of the Monte Carlo method.

1. In the thesis, it is shown and numerically verified that the measurement model sensitivity, which is a quantity showing how sensitive is the value of measurand to small variations in model input parameters, depends significantly on model parameter values and that in the case when the measurements are to be performed at a fixed frequency and for the MUT whose shape cannot be changed, the model sensitivity is significantly affected by the dielectric constant. Also, it is shown that there are dielectric constant value ranges where the model sensitivity is very low, resulting in unacceptably large measurement uncertainties. Furthermore, these low-sensitivity regions become very wide for the MUT dielectric constant values greater than approximately 10.
2. A new methodology is proposed that allows for evaluating the sensitivity of dielectric constant measurement models based on the data obtained by solving the forward scattering problem only, which makes it possible to quickly and straightforwardly evaluate whether the model is suitable for measurements or not.
3. In the Thesis, it is demonstrated and numerically verified that in the case when the measurements must be performed for a fixed set of model parameters and it is found that the conventional model is not suitable due to an unacceptably large measurement uncertainty, it is possible to construct another non-destructive measurement model to reduce the measurement uncertainty. This model can be constructed by adding one or more additional elements to the conventional model containing the MUT only. Additionally, it is demonstrated that the model sensitivity can also be improved by changing the dimensions of the

sample, but this would require sample destruction, which is not always permissible and possible.

4. The following new models were developed for the extended measurement models:
 - in case a measurement method that involves measuring the dielectric constant of a slab made of the MUT and located in free space or a waveguide is employed, the new models are the two-slab model and the three-slab model;
 - in case a measurement method that involves measuring the dielectric constant of a cylindrical rod made of the MUT (it can be hollow in the middle) and located in a rectangular waveguide is employed, the new measurement model is constructed by adding an auxiliary cylindrical rod.
5. It has been shown that even when conventional measurement models do not exhibit sufficiently high model sensitivity, an extended measurement model developed by the author can be used to considerably improve it (at least 3-5 times) to reduce the dielectric constant measurement uncertainty.
6. The author has developed, successfully verified, and employed for the analysis of some of the measurement models examined in the thesis a new fast and accurate integral equation based numerical method for the scattering data calculation for structures composed of one or more multilayered circular cylindrical dielectric rods, as well as metallic rods. The method has been shown to compute the scattering data at least 50 times faster than existing commercially available finite-element-based software.

The results presented in the thesis have been approved and show that all research objectives of the doctoral thesis have been achieved, and all planned analytical and numerical studies have been successfully accomplished. The results may be of particular importance for the evaluation of dielectric permittivity measurement models for low-loss dielectric materials and for constructing new models with a higher measurement sensitivity than that provided by conventional measurement models containing the MUT only.

BIBLIOGRAPHY

- [1] D. K. Kalluri. *Principles of electromagnetic waves and materials*, CRC Press, 2013.
- [2] L. Chen, L.F., Ong, C. K., Neo, C. P., Varadan, V. V., and V. K. Varadan, *Microwave electronics: measurement and materials characterization*, John Wiley & Sons, 2004.
- [3] A. A. Ward, *State of the Art–Dielectric Materials for Advanced Applications*, National Research Centre, Egypt, 2015.
- [4] Rogers Corporation, Rogers RF & Microwave, see online: <https://www.ccieurolam.com/en/products/rogers-rf-microwave-materials/>
- [5] Trans-Tech, Inc., Products for RF/Microwave Applications, see online: <https://datasheet.octopart.com/SR9000SPQ0472AY-Trans-Tech-datasheet-8861441.pdf>
- [6] J. Krupka, “Frequency domain complex permittivity measurements at microwave frequencies,” *Measurement Science and Technology*, Vol. 17, No. 6, pp. R55–R70, 2006, doi:10.1088/0957-0233/17/6/r01.
- [7] Keysight Technologies, Inc., Basics of Measuring the Dielectric Properties of Materials - Application Notes, see online: <https://www.keysight.com/us/en/assets/7018-01284/application-notes/5989-2589.pdf>
- [8] Rohde and Schwartz, Measurement of Dielectric Material Properties RAC-0607-0019 - Application Notes, see online: https://www.rohde-schwarz.com/hk/applications/measurement-of-dielectric-material-properties-application-note_56280-15697.html
- [9] BIPM, IEC, IFCC, ISO, IUPAC, IUPAP, OIML, Guide to the Expression of Uncertainty in Measurement (GUM), Int. Org. Std., Geneva, Switzerland, Tech. Rep. JCGM 100, 2008.
- [10] Association Connecting Electronics Industries, IPC-TM-650 Test Methods Manual, see online: <https://www.ipc.org/test-methods>
- [11] Rogers Corporation, Thermoset Microwave Materials, see online: https://bayareacircuits.com/wp-content/uploads/2020/05/MDS_Rogers_TMM.pdf
- [12] K. Y. You, F. B. Esa and Z. Abbas, “Macroscopic characterization of materials using microwave measurement methods — A survey,” *2017 Progress in Electromagnetics Research Symposium - Fall (PIERS - FALL)*, pp. 194–204, 2017, doi:10.1109/PIERS-FALL.2017.8293135.
- [13] J. Kui, “Microwave Dielectric Ceramic Materials and Their Industry Development Overview and Future Prospects,” *Journal of Physics: Conference Series*, Vol. 1885, No. 3, p. 032034, 2021, doi:10.1088/1742-6596/1885/3/032034.

- [14] L. Mari, P. Carbone, and D. Petri, "Measurement Fundamentals: A Pragmatic View," *IEEE Transactions on Instrumentation and Measurement*, Vol. 61, No. 8, pp. 2107–2115, 2012, doi: 10.1109/TIM.2012.2193693.
- [15] H. Howard, and D. Gilmer, *High dielectric constant materials: VLSI MOSFET applications*, Springer Science & Business Media, 2006.
- [16] J. Baker-Jarvis, R. G. Geyer, J. H. Grosvenor, M. D. Janezic, C. A. Jones, B. Riddle, C. M. Weil, and J. Krupka, "Dielectric characterization of low-loss materials a comparison of techniques," *IEEE Transactions on Dielectrics and Electrical Insulation*, Vol. 5, No. 4, pp. 571–577, 1998, doi:10.1109/94.708274.
- [17] M. W. Hyde, M. J. Havrilla, A. E. Bogle, E. J. Rothwell, and G. D. Dester, "An Improved Two-Layer Method for Nondestructively Characterizing Magnetic Sheet Materials Using a Single Rectangular Waveguide Probe," *Electromagnetics*, Vol. 32, No. 7, pp. 411–425, 2012, doi:10.1080/02726343.2012.716702.
- [18] G. D. Dester, "Electromagnetic material characterization of a conductor-backed material using the two layer, two thickness, and two iris waveguide probe methods: Error analysis, simulation, and experimental results," 2008.
- [19] E. Paez, M. A. Azpurua, C. Tremola, and R. Callarotti, "Uncertainty minimization in permittivity measurements in shielded dielectric resonators," *Progress In Electromagnetics Research M*, Vol. 26, pp. 127–141, 2012, doi:10.2528/pierm12082811.
- [20] Y. Kato, M. Horibe, M. Ameya, S. Kurokawa, and Y. Shimada, "New Uncertainty Analysis for Permittivity Measurements Using the Transmission/Reflection Method," *IEEE Transactions on Instrumentation and Measurement*, Vol. 64, No. 6, pp. 1748–1753, 2015, doi:10.1109/tim.2015.2401231.
- [21] A. Possolo, and H. K. Iyer, "Invited Article: Concepts and tools for the evaluation of measurement uncertainty," *Review of Scientific Instruments*, Vol. 88, No. 1, p. 011301, 2017, doi:10.1063/1.4974274.
- [22] B. N. Taylor, and C. E. Kuyatt, "Guidelines for evaluating and expressing the uncertainty of NIST measurement results," *National Institute of Standards and Technology Technical Note 1297*, 1994.
- [23] E. Páez, M. A. Azpúrua, C. Tremola, and R. C. Callarotti, "Uncertainty estimation in complex permittivity measurements by shielded dielectric resonator technique using the monte carlo method," *Progress In Electromagnetics Research B*, Vol. 41, pp. 101–119, 2012, doi:10.2528/pierb12041306.
- [24] R. Kacker, "True value and uncertainty in the GUM," *Journal of Physics: Conference Series*, Vol. 1065, No. 21, p. 212003, 2018, doi:10.1088/1742-6596/1065/21/212003.

- [25] “Applying Error Correction to Network Analyzer Measurements,” Agilent application note 1287-3.
- [26] A. A. Cliford, *Multivariate Error Analysis: A Handbook of Error Propagation and Calculation in Many-Parameter Systems*, Applied Science Publishers, 1973.
- [27] BIPM, IEC, et al., “Evaluation of Measurement Data – Supplement 1 to the Guide to the Expression of Uncertainty in Measurement – Propagation of Distributions using a Monte Carlo Method,” BIPM, 2008.
- [28] E. T. Jaynes, “Information Theory and Statistical Mechanics,” *Physical Review*, Vol. 106, No. 4, pp. 620–630, 1957, doi:10.1103/physrev.106.620.
- [29] D. Dowson, and A. Wragg, “Maximum-entropy distributions having prescribed first and second moments (Corresp.),” *IEEE Transactions on Information Theory*, Vol. 19, No. 5, pp. 689–693, 1973, doi:10.1109/TIT.1973.1055060.
- [30] M. G. Cox, and B. R. L. Siebert, “The use of a Monte Carlo method for evaluating uncertainty and expanded uncertainty,” *Metrologia*, Vol. 43, No. 4, pp. S178–S188, 2006, doi:10.1088/0026-1394/43/4/s03.
- [31] B. A. Wichmann, and I. D. Hill, “Algorithm AS 183: An Efficient and Portable Pseudo-Random Number Generator,” *Applied Statistics*, Vol. 31, No. 2, p. 188, 1982, doi:10.2307/2347988.
- [32] B. A. Wichmann, and I. D. Hill, “Correction: Algorithm AS 183: An Efficient and Portable Pseudo-Random Number Generator,” *Applied Statistics*, Vol. 33, No. 1, p. 123, 1984, doi:10.2307/2347676.
- [33] B. A. Wichmann, and I. D. Hill, “Generating good pseudo-random numbers,” *Computational Statistics & Data Analysis*, Vol. 51, No. 3, 2006, doi:10.1016/j.csda.2006.05.019.
- [34] G. E. P. Box, and M. E. Muller, “A Note on the Generation of Random Normal Deviates,” *The Annals of Mathematical Statistics*, Vol. 29, No. 2, pp. 610–611, 1958, doi:10.1214/aoms/1177706645.
- [35] J. F. Epperson, *An introduction to numerical methods and analysis*, John Wiley & Sons, 2021.
- [36] J. Baker-Jarvis, M. D. Janezic, J. H. Grosvenor, Jr., and R. G. Geyer, “Transmission/reflection and short-circuit line methods for measuring permittivity and permeability,” NIST, Gaithersburg, MD, USA, Tech. Note 1355-R, 1992.
- [37] I. Rolfes, and B. Schiek, “Calibration methods for microwave free space measurements,” *Advances in Radio Science*, Vol. 2, pp. 19–25, 2005, doi:10.5194/ars-2-19-2004.

- [38] P. G. Bartley, and S. B. Begley, "A new free-space calibration technique for materials measurement," *2012 IEEE International Instrumentation and Measurement Technology Conference Proceedings*, pp. 47–51, 2012, doi:10.1109/I2MTC.2012.6229351.
- [39] B. Will, and I. Rolfes, "Application of the thru-network-line self-calibration method for free space material characterizations," *Proceedings of 2012 International Conference on Electromagnetic Advanced Applications. ICEAA'12*, pp. 831–834, 2012, doi:10.1109/ICEAA.2012.6328749.
- [40] A. M. Nicolson, and G. F. Ross, "Measurement of the Intrinsic Properties of Materials by Time-Domain Techniques," *IEEE Transactions on Instrumentation and Measurement*, Vol. 19, No. 4, pp. 377–382, 1970, doi:10.1109/TIM.1970.4313932.
- [41] W. B. Weir, "Automatic measurement of complex dielectric constant and permeability at microwave frequencies," *Proceedings of the IEEE*, Vol. 62, No. 1, pp. 33–36, 1974, doi:10.1109/PROC.1974.9382.
- [42] E. J. Rothwell, J. L. Frasch, S. M. Ellison, P. Chahal, and R. O. Ouedraogo, "Analysis of the Nicolson-Ross-Weir method for characterizing the electromagnetic properties of engineered materials," *Progress In Electromagnetics Research*, Vol. 157, pp. 31–47, 2016, doi:10.2528/pier16071706.
- [43] A. Elhawil, R. Vounckx, L. Zhang, G. Koers, and J. Stiens, "Comparison between two optimisation algorithms to compute the complex permittivity of dielectric multilayer structures using a free-space quasi-optical method in W-band," *IET Science, Measurement & Technology*, Vol. 3, No. 1, pp. 13–21, 2009, doi:10.1049/iet-smt:20070085.
- [44] N. Gagnon, J. Shaker, L. Roy, A. Petosa, and P. Berini, "Low-cost free-space measurement of dielectric constant at Ka band," *IEE Proceedings - Microwaves, Antennas and Propagation*, Vol. 151, No. 3, p. 271, 2004, doi:10.1049/ip-map:20040264.
- [45] A. Jurado, D. Escot, D. Poyatos, and I. Montiel, "Application of artificial neural networks to complex dielectric constant estimation from free-space measurements," *Methods Model. Artif. Nat. Comput.* pp. 517–526, 2009, doi:10.1007/978-3-642-02264-7_53
- [46] I. Zivkovic, and A. Murk, "Extraction of dielectric and magnetic properties of carbonyl iron powder composites at high frequencies," *Journal of Applied Physics*, Vol. 111, No. 11, p. 114104, Jun. 2012, doi:10.1063/1.4725473.
- [47] A. Elhawil, J. Stiens, R. Vounckx, G. Koers, and L. Zhang, "Reliable method for material characterisation using quasi-optical free-space measurement in W-band," *IET Science, Measurement & Technology*, Vol. 3, No. 1, pp. 39–50, 2009, doi:10.1049/iet-smt:20070086.

- [48] J. Baker-Jarvis et al., “Dielectric characterization of low-loss materials a comparison of techniques,” *IEEE Transactions on Dielectrics and Electrical Insulation*, Vol. 5, No. 4, pp. 571–577, 1998, doi:10.1109/94.708274.
- [49] J. Baker-Jarvis, R. G. Geyer, and P. D. Domich, “A nonlinear least-squares solution with causality constraints applied to transmission line permittivity and permeability determination,” *IEEE Transactions on Instrumentation and Measurement*, Vol. 41, No. 5, pp. 646–652, 1992, doi:10.1109/19.177336.
- [50] K. Y. You, “Materials Characterization Using Microwave Waveguide System,” *Microwave Systems and Applications*, 2017, doi:10.5772/66230.
- [51] S. Kim, and J. Baker-Jarvis, “An Approximate Approach to Determining the Permittivity and Permeability Near $\lambda/2$ Resonances in Transmission/Reflection Measurements,” *Progress In Electromagnetics Research B*, Vol. 58, pp. 95–109, 2014, doi:10.2528/pierb13121308.
- [52] A. Kazemipour et al., “Analytical Uncertainty Evaluation of Material Parameter Measurements at THz Frequencies,” *Journal of Infrared, Millimeter, and Terahertz Waves*, Vol. 41, No. 10, pp. 1199–1217, 2020, doi:10.1007/s10762-020-00723-0.
- [53] S. L. S. Severo, A. A. A. de Salles, B. Nervis, and B. K. Zanini, “Non-resonant Permittivity Measurement Methods,” *Journal of Microwaves, Optoelectronics and Electromagnetic Applications*, Vol. 16, No. 1, pp. 297–311, 2017, doi:10.1590/2179-10742017v16i1890.
- [54] E. Ni, “An uncertainty analysis for the measurement of intrinsic properties of materials by the combined transmission-reflection method,” *IEEE Transactions on Instrumentation and Measurement*, Vol. 41, No. 4, pp. 495–499, 1992, doi:10.1109/19.155914.
- [55] C. Yang, and H. Huang, “Determination of Complex Permittivity of Low-Loss Materials From Reference-Plane Invariant Transmission/Reflection Measurements,” *IEEE Access*, Vol. 7, pp. 131865–131872, 2019, doi:10.1109/ACCESS.2019.2940723.
- [56] M. Ding, Y. Liu, X. Lu, Y. Li, and W. Tang, “An Improved Algorithm for Deducing Complex Permittivity of Thin Dielectric Samples with the Transmission/Reflection Method,” *Progress In Electromagnetics Research M*, Vol. 84, pp. 1–9, 2019, doi:10.2528/pierm19061802.
- [57] U. C. Hasar, and M. T. Yurtcan, “A Microwave Method Based on Amplitude-only Reflection measurements for Permittivity Determination of Low-loss Materials,” *Measurement*, vol. 43, no. 9, pp. 1255–1265, 2010, doi:10.1016/j.measurement.2010.07.002.
- [58] Z. Awang, F. A. M. Zaki, N. H. Baba, A. S. Zoolfakar, and R. A. Bakar, “A Free-Space Method for Complex Permittivity Measurement of Bulk and Thin Film Dielectrics at Microwave Frequencies,” *Progress In Electromagnetics Research B*, Vol. 51, pp. 307–328, 2013, doi:10.2528/pierb13031509.

- [59] U. C. Hasar, and M. T. Yurtcan, "A microwave method based on amplitude-only reflection measurements for permittivity determination of low-loss materials," *Measurement*, Vol. 43, No. 9, pp. 1255–1265, 2010, doi:10.1016/j.measurement.2010.07.002.
- [60] U. C. Hasar, "A Generalized Formulation for Permittivity Extraction of Low-to-High-Loss Materials From Transmission Measurement," *IEEE Transactions on Microwave Theory and Techniques*, Vol. 58, No. 2, pp. 411–418, 2010, doi:10.1109/TMTT.2009.2038443.
- [61] L. Mari, P. Carbone and D. Petri, "Measurement Fundamentals: A Pragmatic View," *IEEE Transactions on Instrumentation and Measurement*, Vol. 61, No. 8, pp. 2107–2115, 2012, doi:10.1109/TIM.2012.2193693.
- [62] R. A. Fenner, E. J. Rothwell, and L. L. Frasci, "Application of Interval Analysis on Error Analysis of Reflection-Only Material Characterization Methods," *Progress In Electromagnetics Research*, Vol. 142, pp. 231–241, 2013, doi:10.2528/pier13062806.
- [63] J. Baker-Jarvis, "Transmission/reflection and short-circuit line permittivity measurements," *NIST, Gaithersburg, MD, USA, Tech. Note 1341*, 1990.
- [64] T. Ozturk, and M. Tahir Güneşer, "Measurement Methods and Extraction Techniques to Obtain the Dielectric Properties of Materials," *Electrical and Electronic Properties of Materials. IntechOpen*, 2019, doi:10.5772/intechopen.80276.
- [65] D. M. Kerns, and R. Beatty, *Basic Theory of Waveguide Junctions and Introductory Microwave Network Analysis*. NY: Pergamon Press, 1967.
- [66] U. C. Hasar, "Permittivity Measurement of Thin Dielectric Materials from Reflection-only Measurements Using One-Port Vector Network Analyzers," *Progress In Electromagnetics Research*, Vol. 95, pp. 365–380, 2009, doi:10.2528/pier09062501.
- [67] U. C. Hasar, "A Microwave Method for Noniterative Constitutive Parameters Determination of Thin Low-Loss or Lossy Materials," *IEEE Transactions on Microwave Theory and Techniques*, Vol. 57, No. 6, pp. 1595–1601, 2009, doi:10.1109/TMTT.2009.2020779.
- [68] U. C. Hasar, "A Fast and Accurate Amplitude-Only Transmission-Reflection Method for Complex Permittivity Determination of Lossy Materials," *IEEE Transactions on Microwave Theory and Techniques*, Vol. 56, No. 9, pp. 2129–2135, 2008, doi:10.1109/TMTT.2008.2002229.
- [69] U. C. Hasar, and C. R. Westgate, "A Broadband and Stable Method for Unique Complex Permittivity Determination of Low-Loss Materials," *IEEE Transactions on Microwave Theory and Techniques*, Vol. 57, No. 2, pp. 471–477, 2009, doi:10.1109/TMTT.2008.2011242.

- [70] Keysight Technologies, Inc., N1500A Materials Measurement Suite, see online: <https://www.keysight.com/us/en/assets/7018-04630/technical-overviews/5992-0263.pdf>
- [71] J. Baker-Jarvis, E. J. Vanzura, and W. A. Kissick, "Improved technique for determining complex permittivity with the transmission/reflection method," *IEEE Transactions on Microwave Theory and Techniques*, Vol. 38, No. 8, pp. 1096–1103, 1990, doi:10.1109/22.57336.
- [72] A. R. Von Hippel, *Dielectric Materials and Applications*, John Wiley and Sons, New York, 1954
- [73] A. Rashidian, L. Shafai, D. Klymyshyn, and C. Shafai, "A Fast and Efficient Free-Space Dielectric Measurement Technique at mm-Wave Frequencies," *IEEE Antennas and Wireless Propagation Letters*, Vol. 16, pp. 2630–2633, 2017, doi:10.1109/LAWP.2017.2737632.
- [74] R. Grignon, M. N. Afsar, Yong Wang, and S. Butt, "Microwave broadband free-space complex dielectric permittivity measurements on low loss solids," *Proceedings of the 20th IEEE Instrumentation Technology Conference (Cat. No.03CH37412)*, 2003, pp. 865-870, doi:10.1109/IMTC.2003.1208278.
- [75] J. Musil, and F. Zacek, *Microwave measurements of complex permittivity by free space methods and their applications*. Amsterdam and New York, Elsevier, 1986.
- [76] L. E. R. Petersson, and G. S. Smith, "An estimate of the error caused by the plane-wave approximation in free-space dielectric measurement systems," *IEEE Transactions on Antennas and Propagation*, Vol. 50, No. 6, pp. 878–887, 2002, doi:10.1109/TAP.2002.1017671.
- [77] D. K. Ghodgaonkar, V. V. Varadan, and V. K. Varadan, "A free-space method for measurement of dielectric constants and loss tangents at microwave frequencies," *IEEE Transactions on Instrumentation and Measurement*, Vol. 38, No. 3, pp. 789–793, 1989, doi:10.1109/19.32194.
- [78] A. N. Nguyen, and H. Shirai, "Electromagnetic Scattering Analysis from Rectangular Dielectric Cuboids - TE Polarization -," *IEICE Transactions on Electronics*, Vol. E99.C, No. 1, pp. 11–17, 2016, doi:10.1587/transele.e99.c.11.
- [79] A. N. Nguyen, and H. Shirai, "A Free Space Permittivity Measurement at Microwave Frequencies for Solid Materials," *IEICE Transactions on Electronics*, Vol. E100.C, No. 1, pp. 52–59, 2017, doi:10.1587/transele.e100.c.52.
- [80] Y. Qin, B. Wei, S. Liu, M. Li, C. Cai, and T. Hou, "A new method for measuring complex relative permittivity of dielectric material by reflection method," *Journal of Physics: Conference Series*, Vol. 1871, No. 1, p. 012002, 2021, doi:10.1088/1742-6596/1871/1/012002.

- [81] F. Gonçalves, A. Pinto, R. Mesquita, E. Silva, and A. Brancaccio, "Free-Space Materials Characterization by Reflection and Transmission Measurements using Frequency-by-Frequency and Multi-Frequency Algorithms," *Electronics*, Vol. 7, No. 10, p. 260, 2018, doi:10.3390/electronics7100260.
- [82] A. Nishikata, "A Swept-Frequency Measurement of Complex Permittivity and Complex Permeability of a Columnar Specimen Inserted in a Rectangular Waveguide," *IEEE Transactions on Microwave Theory and Techniques*, Vol. 55, No. 7, pp. 1554–1567, 2007, doi:10.1109/TMTT.2007.900340.
- [83] A. Nishikata, "Scattering Analysis for Layered Cylindrical Object Perpendicularly Piercing the Wider Walls of a Rectangular Waveguide and Its Application to ϵ_r and μ_r Measurement," *IEEE Transactions on Microwave Theory and Techniques*, Vol. 57, No. 6, pp. 1602–1611, 2009, doi:10.1109/TMTT.2009.2020838.
- [84] Y. Yamanaka, "Liquid material's complex permittivity measurement using a rectangular waveguide and a dielectric tube at 800 and 900 MHz band," *Proc. Int. Electromagn. Compat. Symp.*, Sendai, Japan, 2004, pp. 645–648.
- [85] K. Sarabandi, "A technique for dielectric measurement of cylindrical objects in a rectangular waveguide," *IEEE Transactions on Instrumentation and Measurement*, Vol. 43, No. 6, pp. 793–798, 1994, doi:10.1109/19.368065.
- [86] J. Abdunnour, C. Akyel, and K. Wu, "A generic approach for permittivity measurement of dielectric materials using a discontinuity in a rectangular waveguide or a microstrip line," *IEEE Transactions on Microwave Theory and Techniques*, Vol. 43, No. 5, pp. 1060–1066, 1995, doi:10.1109/22.382066.
- [87] J. Abdunnour, L. Marchildon, C. Akyel, and K. Wu, "Direct Evaluation of Complex Permittivity from Transmission Line Discontinuity Measurements," *1994 24th European Microwave Conference*, 1994, pp. 974–979, doi:10.1109/EUMA.1994.337338.
- [88] A. Rotava, L. E. P. Borges, M. H. C. Dias, and J. C. A. Santos, "Evaluation of a novel tubular sample holder for dielectric measurements with Abdunnour's method," *2013 SBMO/IEEE MTT-S International Microwave & Optoelectronics Conference (IMOC)*, 2013, pp. 1–5, doi:10.1109/IMOC.2013.6646604.
- [89] A. Rotava, R. A. O. Silva, M. H. C. Dias, and J. C. A. Santos, "An analytical model for permittivity measurement of liquid dielectrics with a tubular sample holder," *Microwave and Optical Technology Letters*, Vol. 63, No. 2, pp. 393–398, 2020, doi:10.1002/mop.32606.
- [90] J. N. Sahalos, and E. Vafiadis, "On the Narrow-Band Microwave Filter Design Using a Dielectric Rod," *IEEE Transactions on Microwave Theory and Techniques*, Vol. 33, No. 11, pp. 1165–1171, 1985, doi:10.1109/TMTT.1985.1133189.

- [91] J. Abdulnour, and L. Marchildon, "Scattering by a dielectric obstacle in a rectangular waveguide," *IEEE Transactions on Microwave Theory and Techniques*, Vol. 41, No. 11, pp. 1988–1994, 1993, doi:10.1109/22.273426.
- [92] C. Bachiller et al. "Hybrid Mode Matching Method for the Efficient Analysis of Metal and Dielectric Rods in H Plane Rectangular Waveguide Devices," in *IEEE Transactions on Microwave Theory and Techniques*, Vol. 58, No. 12, pp. 3634–3644, 2010, doi:10.1109/TMTT.2010.2083951.
- [93] R. Kushnin, and J. Semenjako, "Determination of the optimal value of the radius of a circular cylindrical post in a rectangular waveguide for measurement of the dielectric permittivity," *Proceedings of PIERS*, pp. 52–57, 2013.
- [94] R. Kushnin, J. Semenjako, and T. Solovjova, "Determination of optimal pairs of radii of dielectric samples for complex permittivity measurement of dispersive materials," *Proceedings of PIERS*, pp. 2320–2325, 2015.
- [95] Rogers Corporation, AD1000 Laminates, see online: <https://www.rogerscorp.com/advanced-electronics-solutions/ad-series-laminates/ad1000-laminates>
- [96] Exxelia Temex, Dielectric Resonators, see online: <https://exxelia.com/uploads/PDF/e7000-v1.pdf>
- [97] DURATOOL, Digital Caliper, see online: <https://www.farnell.com/datasheets/1661929.pdf>
- [98] Arlon Microwave Materials, PTFE/Woven Fiberglass/Micro-Dispersed Ceramic Filled Laminate for RF & Microwave Printed Circuit Boards, see online: <http://www.agssales.com/ad430.pdf>
- [99] R. Kushnin, G. Kuzminovs, J. Semenjako and Y. V. Shestopalov, "Novel High-sensitivity Non-destructive Technique for the Measurement of Permittivity of a Low-loss Dielectric Slab in Free Space," *2019 Photonics & Electromagnetics Research Symposium - Spring (PIERS-Spring)*, pp. 1723–1731, 2019, doi:10.1109/PIERS-Spring46901.2019.9017638.
- [100] M. N. O. Sadiku. *Numerical Techniques in Electromagnetics*, Boca Raton, CRC Press, 2001.
- [101] D. D. Davidson, *Computational Electromagnetics for RF and Microwave Engineering*. Cambridge University Press, Cambridge, 2005.
- [102] M. N. O. Sadiku, "Finite Difference Solution of Electrodynamical Problems," *The International Journal of Electrical Engineering & Education*, Vol. 28, No. 3, pp. 230–245, Jul. 1991. doi:10.1177/002072099102800309.

- [103] J. Schwinger, *Notes on lectures. Discontinuities in waveguides*. New York: Gordon and Breach, 1968. 163p.
- [104] N. Marcuvitz, *Waveguide handbook*. London, P. Peregrinus on behalf of the Institution of Electrical Engineers, 1986. 446p.
- [105] J. C. Araneta, M. E. Brodwin and G. A. Kriegsmann, “High-Temperature Microwave Characterization of Dielectric Rods,” *IEEE Transactions on Microwave Theory and Techniques*, Vol. 32, No. 10, pp. 1328–1335, 1984, doi:10.1109/TMTT.1984.1132844.
- [106] Y. Leviatan, P. G. Li, A. T. Adams and J. Perini, “Single-Post Inductive Obstacle in Rectangular Waveguide,” *IEEE Transactions on Microwave Theory and Techniques*, Vol. 31, No. 10, pp. 806–812, 1983, doi:10.1109/TMTT.1983.1131610.
- [107] Y. Leviatan, and G. S. Sheaffer, “Analysis of Inductive Dielectric Posts in Rectangular Waveguide,” *IEEE Transactions on Microwave Theory and Techniques*, Vol. 35, No. 1, pp. 48–59, 1987, doi:10.1109/TMTT.1987.1133594.
- [108] G. S. Sheaffer, and Y. Leviatan, “Composite inductive posts in waveguide—a multifilament analysis,” *IEEE Transactions on Microwave Theory and Techniques*, Vol. 36, No. 4, pp. 779–783, 1988, doi:10.1109/22.3589.
- [109] Chung-I G. Hsu, and H. A. Auda, “Multiple Dielectric Posts in a Rectangular Waveguide,” *IEEE Transactions on Microwave Theory and Techniques*, Vol. 34, No. 8, pp. 883–891, 1986, doi:10.1109/TMTT.1986.1133461.
- [110] P. Silvester, “Symmetric quadrature formulae for simplexes,” *Mathematics of Computation*, Vol. 24, No. 109, pp. 95–100, 1970.
- [111] E. D. Nielsen, “Scattering by a Cylindrical Post of Complex Permittivity in a Waveguide,” *IEEE Transactions on Microwave Theory and Techniques*, Vol. 17, No. 3, pp. 148–153, 1969, doi:10.1109/TMTT.1969.1126913.
- [112] R. Kushnin, and J. Semenjako. “Scattering by a Layered Circular Cylindrical Post in a Rectangular Waveguide,” *Telecommunications and Electronics*, pp. 41–48, 2011.
- [113] R. Gesche, and N. Löchel, “Scattering by a lossy dielectric cylinder in a rectangular waveguide,” *IEEE Transactions on Microwave Theory and Techniques*, Vol. 36, No. 1, pp. 137–144, 1988, doi:10.1109/22.3493.
- [114] R. Gesche, and N. Löchel, “Two cylindrical obstacles in a rectangular waveguide—resonances and filter applications,” *IEEE Transactions on Microwave Theory and Techniques*, Vol. 37, No. 6, pp. 962–968, 1989, doi:10.1109/22.25397.
- [115] T. B. Senior, and J. L. Volakis, *Approximate Boundary Conditions in Electromagnetic*. IEE Press, 1995, 363p.

- [116] M. Abramovich, and I. A. Stegun, *Handbook of Mathematical Functions with Formulas, Graphs and Mathematical Tables*. New York: Dover, 1974. 121p.
- [117] P. P. Ewald, “Die Berechnung optischer und elektrostatischer Gitterpotentiale,” *Annalen der Physik*, Vol. 369, No. 3, pp. 253–287, 1921, doi:10.1002/andp.19213690304.
- [118] C. M. Linton, and I. Thompson, “One- and two-dimensional lattice sums for the three-dimensional Helmholtz equation,” *Journal of Computational Physics*, Vol. 228, No. 6, pp. 1815–1829, 2009, doi:10.1016/j.jcp.2008.11.013.
- [119] S. Boutami, and M. Fall, “Calculation of the Free-Space Periodic Green’s Function Using Equivalent Finite Array,” *IEEE Transactions on Antennas and Propagation*, Vol. 60, No. 10, pp. 4725–4731, 2012, doi:10.1109/TAP.2012.2210179.
- [120] M. J. Park, and S. Nam, “Rapid summation of the Green’s function for the rectangular waveguide,” *IEEE Transactions on Microwave Theory and Techniques*, Vol. 46, No. 12, pp. 2164–2166, 1998, doi:10.1109/22.739301
- [121] G. T. Lei, “An Efficient and Simple Approach to Computing the Green’s Function for the Rectangular Cavity,” *IEEE Microwave and Wireless Components Letters*, Vol. 20, No. 7, pp. 363–365, 2010, doi:10.1109/LMWC.2010.2049423.
- [122] M. G. Silveirinha, and C. A. Fernandes, “A new acceleration technique with exponential convergence rate to evaluate periodic Green functions,” *IEEE Transactions on Antennas and Propagation*, Vol. 53, No. 1, pp. 347–355, 2005, doi:10.1109/TAP.2004.838793.
- [123] M. J. Park, and S. Nam, “Rapid calculation of the Green’s function in the shielded planar structures,” *IEEE Microwave and Guided Wave Letters*, Vol. 7, No. 10, pp. 326–328, 1997, doi:10.1109/75.631190.
- [124] C. M. Linton, “Schlömlich series that arise in diffraction theory and their efficient computation,” *Journal of Physics A: Mathematical and General*, Vol. 39, No. 13, pp. 3325–3339, 2006, doi:10.1088/0305-4470/39/13/012.
- [125] J. C. Nedelec. *Acoustic and Electromagnetic Equations: Integral Representations for Harmonic Problems*, Springer-Verlag, New York, 2010.
- [126] G. N. Watson. *A Treatise on the Theory of Bessel Functions*, Cambridge University Press, Cambridge, 1995.
- [127] E. T. Whittaker, and G. N. Watson, *A Course in Modern Analysis*, 4th ed. Cambridge, England: Cambridge University Press, 1990.
- [128] R. Kushnin, J. Semenjak, and Y. V. Shestopalov, “Accelerated boundary integral method for solving the problem of scattering by multiple multilayered circular cylindrical posts in a

- rectangular waveguide,” *2017 Progress In Electromagnetics Research Symposium - Spring (PIERS)*, pp. 3263–3271, 2017, doi:10.1109/PIERS.2017.8262320.
- [129] R. Kushnin, J. Semenjako, and Y. Shestopalov, “Fast Method for Analysis of Multiple H-Plane Cylindrical Posts with Multiple Cylindrical Inclusions in a Rectangular Waveguide,” *2020 IEEE Microwave Theory and Techniques in Wireless Communications (MTTW)*, pp. 190–194, 2020, doi:10.1109/MTTW51045.2020.9244922.
- [130] G. D. Dester, E. J. Rothwell, M. J. Havrilla, and M. W. Hyde IV, “Error Analysis of a Two-Layer Method for the Electromagnetic Characterization of Conductor-Backed Absorbing Material Using an Open-Ended Waveguide Probe,” *Progress In Electromagnetics Research B*, Vol. 26, pp. 1–21, 2010, doi:10.2528/pierb10080506.
- [131] R. Kushnin, J. Semenjako, Y. V. Shestopalov, and A. Viduzs, “Two-Slab High Sensitivity Technique for Measurement of Permittivity of a Dielectric Slab in a Rectangular Waveguide,” *2018 Progress in Electromagnetics Research Symposium (PIERS-Toyama)*, pp. 176–183, 2018, doi:10.23919/PIERS.2018.8597966.
- [132] R. Kushnin, J. Semenjako, and Y. V. Shestopalov, “Maximum-sensitivity method for minimizing uncertainty in the measurements of permittivity of a cylindrical dielectric sample in a rectangular waveguide,” *2017 Progress in Electromagnetics Research Symposium - Fall (PIERS - FALL)*, pp. 570–578, 2017, doi:10.1109/PIERS-FALL.2017.8293202.
- [133] R. A. Fenner, E. J. Rothwell, and L. L. Frasch, “A comprehensive analysis of free-space and guided-wave techniques for extracting the permeability and permittivity of materials using reflection-only measurements,” *Radio Science*, Vol. 47, No. 1, p. RS1004, 2012, doi:10.1029/2011rs004755.
- [134] P. S. Epstein, and A. D. Berk, “Ferrite Post in a Rectangular Wave Guide,” *Journal of Applied Physics*, Vol. 27, pp. 1328–1335, 1956.
- [135] N. Okamoto, I. Nishioka, and Y. Nakanishi, “Scattering by a Ferrimagnetic Circular Cylinder in a Rectangular Waveguide,” *IEEE Transactions on Microwave Theory and Techniques*, Vol. 19, No. 6, pp. 521–527, 1971, doi:10.1109/TMTT.1971.1127568.
- [136] N. Gotsis, E. E. Vafiadis, and J. N. Sahalos, “The discontinuity problem of a cylindrical dielectric post in a waveguide and its application on the dielectric constant measurements of liquids,” *Archiv für Elektrotechnik*, Vol. 68, No. 4, pp. 249–257, 1985, doi:10.1007/bf01845936.
- [137] E. Vafiadis, I. A. Tsoukalas, and J. N. Sahalos, “Metallic post coated by a dielectric tube in waveguide, a NB filter design,” *Archiv für Elektrotechnik*, Vol. 70, No. 3, pp. 195–203, 1987, doi:10.1007/bf01574069.

- [138] C. M. Linton, and I. Thompson, “One- and two-dimensional lattice sums for the three-dimensional Helmholtz equation,” *Journal of Computational Physics*, Vol. 228, No. 6, pp. 1815–1829, 2009, doi:10.1016/j.jcp.2008.11.013.



Romāns Kušņins was born in 1986 in Riga. He obtained a Bachelor's degree in Electronics in 2009 and a Master's degree in Electronics in 2011 from Riga Technical University. He has been a lecturer and researcher at Riga Technical University since 2017. His research interests include electromagnetics, microwave devices, wireless power transfer, filter and antenna design, and applied mathematics.